Visually Guided Pursuit in Harris's Hawks



James Shelton

Lady Margaret Hall

University of Oxford

A thesis submitted for the degree of

Doctor of Philosophy

Michaelmas 2022

Abstract

Prey pursuit in birds is a complex goal-oriented behaviour mechanised via active control of the visual system. This active gaze control enables the bird to track their targets. In this thesis, I investigate the pursuit behaviour of Harris's hawks (*Parabuteo unicinctus*), which are dependent on visual cues to catch their prey. I build upon existing research on the mathematical rules that describe pursuit in raptors and to describe the gaze strategy of Harris's hawks for the first time. To do this, I develop and validate a highly accurate biologger, which combines post processed GPS data with an inertial measurement unit (IMU) to record the head movements of hawks. The accuracy of the GPS solution validated to be < 0.02m marks a significant improvement over currently used systems in animal behaviour research. Using this logger, I capture flight data of Harris's hawks in aerial pursuit of a smoothly manoeuvring target. I fit several known guidance laws to the experimental flight data and identify the best fitting model. I investigate the head movements of hawks during flight and identify a gaze strategy that describes their behaviour. I then use this in combination with guidance modelling to hypothesise how sensory outputs might be used to mechanise guidance in Harris's hawks and discuss the implications of this for animal behaviour and for improvements to target tracking in aerial robotics.

Acknowledgements

First of all, many thanks to my supervisor Graham Taylor for all of the insightful guidance that has been provided over the years. It has been great experience working in the Oxford Flight group and I look forward to keeping up with upcoming research. Thank you to my internal assessors Tim Guilford and in particular Adrian Thomas for not only providing helpful comments but also being a part of the deciding panel to award me a scholarship that enabled me to pursue this research. Thank you to all members of the Oxford Flight Group for technical assistance and camaraderie along the way. A big thanks to Caroline for having an experiment setup and ready to go by week 1! Thank you to Helen, Lucy and Mark for your falconry expertise and thanks to Phil for allowing me to park my car sometimes!

Thank you to the University of Oxford and Lady Margaret Hall for my scholarship to enable me to do this DPhil and thank you to the ERC for supporting the materials needed to perform this research.

Last but not least, I would like to thank my family for their continual support throughout the past 4 years. Numerous trips to Moelfre Isaf during lockdown to test my GNSS sensor will not be forgotten!

Contributions

I declare that this thesis has been composed solely by myself and that it has not been submitted, in whole or in part, in any previous application for a degree. Except where stated otherwise by reference or acknowledgement, the work presented is entirely my own. My contributions towards the data chapters are as follows:

Chapter 2. Developing a High Accuracy, High Precision GNSS Biologger

This chapter is presented as a manuscript *in prep* for submission to a peer-reviewed journal. I conducted the hardware and software, designed validation experiments, analysed the results and wrote the manuscript with the supervision of Graham Taylor.

Chapter 3. Guidance Modelling of a Harris's Hawk in Pursuit of a Smoothly Manoeuvring Target

This chapter is presented as a manuscript *in prep* for submission to a peer-reviewed journal. This work was conceived by Graham Taylor, Caroline Brighton and myself. Caroline Brighton designed the experiment, I collected and post processed the data and analysed the results. I wrote the final manuscript and edited with suggestions from Caroline Brighton and with the supervision of Graham Taylor.

Chapter 4. Gaze Strategy in Harris's Hawks

This chapter is presented as a manuscript *in prep* for submission to a peer-reviewed journal. This work was conceived by Graham Taylor, Caroline Brighton and myself. Caroline Brighton designed the experiment, I collected and postprocessed the data and analysed the results. At present, I wrote the final manuscript and edited with the supervision of Graham Taylor.

Contents

List of Figures **viii**

List of Tables **x**

1 Modes of Target Guidance and Pursuit in Biological and Engineered Systems **1**

1.1 Introduction . . . 1
1.2 Pursuit Guidance . . . 2
1.3 The Visual System . . . 7
1.3.1 Birds . . . 7
1.3.2 Missiles & Flying Aerial Systems . . . 8
1.4 Gaze Movements and Mechanisation of Guidance . . . 9
1.4.1 Biological Systems . . . 10
1.4.2 Missiles & Flying Aerial Systems . . . 14
1.5 What might a Bio-Inspired System Look Like? . . . 15
1.5.1 Gaze Strategy in Pursuit . . . 15
1.5.2 What might be gained through the use of a bio-inspired saccadic gaze strategy? . . . 16
1.6 Thesis structure . . . 17

2 Developing a High Accuracy, High Precision GNSS Biologger **20**

2.1 Introduction . . . 21
2.1.1 Non-Satellite Technologies . . . 21
2.1.2 Satellite Technologies (Argos, GNSS) . . . 22
2.1.3 Advanced GNSS correction techniques . . . 24
2.2 Materials and Methods . . . 27
2.3 Results . . . 29
2.3.1 Accuracy and Precision . . . 29
2.3.2 Technical Validation . . . 29
2.3.3 Pursuit Experiment with IMU Head Tracking . . . 38
2.4 Discussion . . . 44
2.4.1 PPK Logger Capabilities . . . 44
2.4.2 Trade-offs in GNSS Technology Selection . . . 46

3 Guidance Modelling of a Harris's Hawk in Pursuit of a Smoothly Manoeuvring Target 50
3.1 Introduction . . . 51
3.2 Materials and Methods . . . 53
3.2.1 Experimental Design . . . 53
3.2.2 Instrumentation . . . 55
3.2.3 GPS Data Processing . . . 55
3.2.4 Wind Measurements . . . 57
3.2.5 Guidance Simulations . . . 57
3.2.6 System identification . . . 58
3.3 Results . . . 59
3.3.1 Guidance Modelling . . . 59
3.3.2 Harris's Hawk trajectories are best modelled by the mixed guidance law . . . 61
3.3.3 Generating a lift-based mixed guidance model for gliding flight in wind . . . 66
3.3.4 Incorporating air velocity to definition of deviation angle . . . 69
3.4 Discussion . . . 69
3.4.1 Sensory Inputs . . . 70
3.4.2 Comparison in guidance law behaviour . . . 71
3.4.3 The mixed guidance law is robust to wind . . . 76

4 Gaze Strategy in Harris's Hawks 78
4.1 Introduction . . . 79
4.2 Materials and Methods . . . 83
4.2.1 Data Collection . . . 83
4.2.2 Data Processing . . . 85
4.2.3 Guidance Simulations . . . 86
4.2.4 System identification . . . 87
4.3 Results . . . 88
4.3.1 Gaze Analyses . . . 88
4.3.2 Proxies . . . 93
4.3.3 Guidance Modelling . . . 95
4.3.4 Guidance modelling results . . . 97
4.4 Discussion . . . 99
4.4.1 Gaze Strategy . . . 99
4.4.2 Mechanisation of guidance . . . 102
4.4.3 Limitations . . . 108
4.4.4 Future work . . . 109

5 Conclusions and Future Work **111**
5.1 Conclusions . . . 111
5.2 Limitations and Recommendations . . . 114
5.3 Future Work . . . 117

References **120**

Appendices

A Supplementary for Chapter 2 - Developing a High Accuracy, High Precision GNSS Biologger **130**
A.1 Supplementary Text: A GNSS Primer . . . 130
A.1.1 System Overview . . . 130
A.1.2 GNSS Code Positioning . . . 131
A.1.3 GNSS Error Sources and Techniques to Improve Position Accuracy . . . 132
A.1.4 Reference Coordinate System . . . 134
A.2 Supplementary Methods . . . 134
A.2.1 Sensor Design Specifications . . . 134
A.2.2 Component Choices . . . 134
A.2.3 Base Station Reference Networks . . . 137
A.2.4 GNSS Messages and ZED-F9P Configuration using u-Center 137
A.2.5 Electromagnetic Compatibility . . . 138
A.2.6 Software Architecture . . . 139
A.2.7 Sensor Operation . . . 141
A.2.8 Post Processing Software Overview . . . 141
A.2.9 Circuit Wiring Diagram . . . 142

B Supplementary for Chapter 3 - Guidance Modelling **144**
B.1 Augmented PN and PN+PP . . . 144

C Supplementary for Chapter 4 - Gaze Strategy in Harris's Hawks **147**
C.1 Supplementary Methods . . . 147
C.1.1 GNSS Data Processing . . . 147
C.1.2 IMU Calibration . . . 148
C.2 Supplementary Figures . . . 148

References **153**

List of Figures

1.1 Definition sketch showing inertially derived angles 3
1.2 Geometric rules that describe aerial interception trajectories 3

2.1 GNSS-IMU biologger 28
2.2 Results of static accuracy/precision experiment 31
2.3 Results of dynamic testing using motorised turntable 33
2.4 3D plot of dynamic test with L1 helical antenna and photo of experimental setup on triangulation point 34
2.5 Adjusted PVT data over each 4s revolution shifted to the origin for the L1 helical antenna 35
2.6 Results of dynamic testing when applying the interpolated PPK correction compared to the true PPK and uncorrected SBAS solution 37
2.7 Median fitted circle centroid error for uncorrected PVT data, interpolated PVT data and PPK reference over a range of flight intervals 37
2.8 Two pursuit flights showing bird and target trajectories with lines of sight and head orientation vectors 39
2.9 Accuracy of GNSS satellite fix 40
2.10 Velocity quality control from IMU acceleration data 41
2.11 Impact of GNSS error on deviation angle and LoS rate for first flight 43
2.12 Impact of GNSS error on deviation angle and LoS rate for second flight 43

3.1 Schematic of experimental setup 54
3.2 Definition sketch showing inertially derived angles 61
3.3 Mixed guidance law surface plots 62
3.4 Comparison between measured and simulated intercept trajectories 64
3.5 Comparison of guidance law fit performance 65
3.6 Sensitivity analysis of PN+PP optimal guidance parameters 66
3.7 Wind modelling implementation flow diagram 67
3.8 Comparison of wind modelling guidance law fit performance 68
3.9 Comparison of simulated trajectories using optimal guidance parameters tuned with smooth and erratic targets 74

3.10 Comparison of simulation error using optimal guidance parameters tuned with smooth and erratic targets 75

4.1 Schematic of experimental setup 84
4.2 Inertial angle definitions and visual field of the Harris's hawk 89
4.3 Time histories over a single flight 90
4.4 Time histories cropped between 6 and 7 seconds to display behaviour during saccade that starts at $t = 6.38\,\mathrm{s}$ 92
4.5 Histogram of the head tracking error 93
4.6 Time history and correlation spatial histograms to assess the suitability of head yaw rate as a proxy to line-of-sight rate and gaze direction to velocity angle as a proxy to deviation angle 96
4.7 Histograms of the root mean squared error over all flights for PP, PN and PN+PP guidance models when using input proxy or truth guidance parameters 99
4.8 Histograms of the fitted guidance parameters N and K for PP, PN and PN+PP guidance laws simulated using proxy and truth inputs 100
4.9 Definition sketch showing 2D angles used in guidance control analysis 105
4.10 Block diagram for PN 106
4.11 Block diagram for mixed guidance law PN+PP 107

A.1 RTOS Sequence Diagram 140
A.2 Biologger circuit wiring diagram 143

B.1 Comparison of augmented guidance law fit performance 145
B.2 Simulated trajectories for guidance laws using augmented PN 146

C.1 Power spectral density of head yaw rate and vertical linear acceleration for a single flight 149
C.2 Scatter plot of median correlation coefficient over all flights between inertially derived line-of-sight rate and head yaw rate filtered using a low pass filter with different cutoff frequencies 150
C.3 2D trajectory plots showing how the head gaze bearing (blue arrows) and instantaneous line-of-sight vectors (grey) between the hawk (blue) and the target (red) vary throughout 8 flights 151
C.4 Time histories of head yaw bearing (red), LoS bearing (blue) and track angle (yellow) bearing for 8 flights 152
C.5 Time history of head tracking error for 8 flights. 152

List of Tables

2.1 Median fitted centroid error and radius for PPK, PVT and interpolated PPK correction methods for differing flight interval durations 38
2.2 Table presenting the correlation coefficients between interpolated PPK x and y velocities and IMU and PVT derived x and y velocities. 41
2.3 Standard deviation in metres for PPK method with L1/L2 patch antenna and interpolated PPK method with L1 helical antenna. . . 42

4.1 Results of guidance fitting with proxy and truth input guidance parameters for PP, PN and PN+PP guidance models 97

B.1 Globally fitted guidance parameters for augmented PN and augmented PN + PP 145

1

Modes of Target Guidance and Pursuit in Biological and Engineered Systems

1.1 Introduction

The evolution of the eye from a system able to detect changes in light intensity to one with high spatial resolution and focusing optics enabled the development of visually guided behaviours in animals. Vision is fundamental to basic locomotive tasks such as self-motion estimation, orientation and obstacle avoidance and also goal directed behaviours such as prey detection and pursuit guidance, predator detection and evasion and perching [1]. In this literature review, we compare behaviours in flying animals; specifically birds and insects. Both the low acuity compound eyes of insects and the spatially acute camera eyes of raptors are able to facilitate these behaviours despite their vastly differing morphology. Active gaze control directs and stabilises the visual system through eye movements, head movements or a combination of both to enhance the information acquired to perform each task. Gaze control is essential in aerial pursuit and guidance in animals and in homing missile systems; an engineered system with similar function. Here, we compare the different strategies of aerial target guidance and pursuit in animals and missile systems and explain how a biologically inspired strategy might drive improvements in the field of robotics.

1.2 Pursuit Guidance

Before exploring the visual abilities of biological and engineered systems, it is important to understand the goal-directed behaviour of pursuit guidance which leads the attacker on a collision course to its prey. Previous research articles fitted three geometric rules to the attack trajectories of birds [2], dragonflies [3] and bats [4] based on constancy of one of two angles; the line-of-sight (LoS) bearing (λ) between the attacker and target positions, and the deviation angle (δ) between the attacker's velocity vector and the line-of-sight to target (see Figure 1.1). The first of these geometric rules is pure pursuit, which is defined by the rule $\delta(t) = 0$ where the attacker always flies towards the target. This has been described in blowflies [5], honeybees [6], tiger beetles [7] and houseflies [8]. The second geometric rule of deviated pursuit is observed when the attacker always flies towards the target at a non-zero deviation angle and is defined by $\delta(t) = \alpha$. Under the third geometric rule, the attacker maintains the target at a constant inertially referenced line-of-sight bearing, as defined by the rule $\lambda(t) = \lambda(0)$. This is known as parallel navigation and has been described in hawks [2] and bats [4]. It is worth noting that there exists a multitude of terms describing these geometric rules including constant absolute target direction (CATD) used for parallel navigation and the constant bearing rule or constant bearing decreasing range (CBDR), which is sometimes used to describe deviated pursuit. The geometry of these three rules can be seen in Figure 1.2. However, more recent research has focused on the fitting of behavioural algorithms [9], in this case a guidance law that models the turning behaviour of the animal based on sensory feedback. Contrary to a geometric rule which considers only the observed trajectory resulting from the guidance law, this type of analysis models how sensory outputs are used to generate a guidance command to guide the animal to target intercept. This allows an exploration of the mathematical rules and sensory systems that might describe and mechanise pursuit guidance in animals. Three guidance laws that are typically used in pursuit are proportional pursuit (PP), proportional navigation (PN) and the mixed guidance law (PN+PP) combines elements of PP and PN and are explained below.

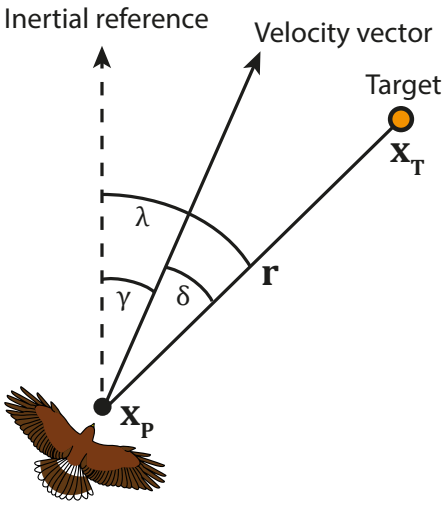


Figure 1.1: Definition sketch showing inertially derived angles of line-of-sight (LoS) bearing λ defined by the LoS vector $\boldsymbol{r}$ between the attacker and target positions $(\boldsymbol{x}_P, \boldsymbol{x}_T)$ and track angle γ which is the inertially referenced velocity vector bearing. Also shown is the egocentrically derived deviation angle δ defined as the angle between the LoS and velocity vectors.

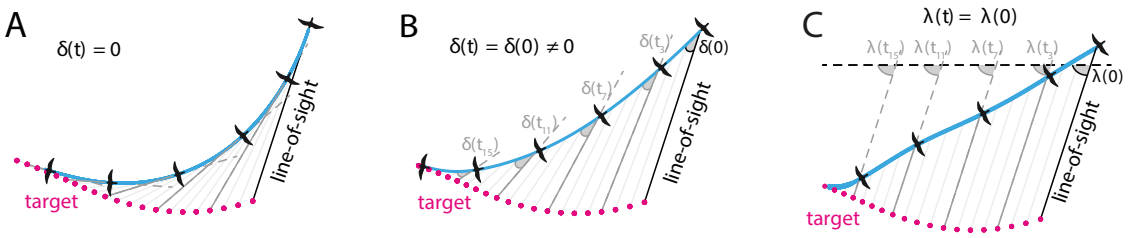


Figure 1.2: Geometric rules that describe aerial interception trajectories. (A) pure pursuit, (B) deviated pursuit, (C) parallel navigation. Reproduced from Brighton et al [10].

Guidance modelling has successfully fitted proportional navigation to describe the attack behaviour of peregrine falcons [10] (*Falco peregrinus*) and fitted a mixed guidance law which combines proportional navigation and proportional pursuit to describe the observed attack behaviour in Harris's hawks (*Parabuteo unicinctus*) [11] and gyrfalcons (*Falco rusticolus*) [12]. This research used Global Positioning System (GPS) loggers attached to the predator and prey to extract position and velocity information of the pursuer relative to the target enabling the use of guidance laws to simulate the measured attack trajectories. The proportional pursuit guidance law generates a steering command that is proportional to the deviation angle between the pursuer's velocity vector and its line-of-sight to target. The line-of-sight to the

target is the inertial vector between the pursuer and target positions. Figure 4.2 presents the angles that define the geometry of pursuit in the inertial frame. This guidance law drives the deviation angle to zero, effectively directing the pursuer's velocity vector towards the target giving the law its tail chase characteristic. PP can be written in the form:

$$\dot{\gamma} = -K\delta \tag{1.1}$$

where $\dot{\gamma}$ is the commanded turn rate, K is the guidance constant and δ is the deviation angle. Proportional navigation commands turning proportionally to the rate of change of the line-of-sight vector between pursuer and target according to equation 1.2

$$\dot{\gamma} = N\dot{\lambda} \tag{1.2}$$

where N is the navigation constant and $\dot{\lambda}$ is the line-of-sight rate. Tuning of the navigation constant in PN leads to differing trajectory shapes. When $N = 1$, the commanded turn rate is equal to the LoS rate so that $\delta(t) = \delta(0)$. This produces a pure or deviated pursuit trajectory. When $N = \infty$, $\dot{\lambda}$ tends to zero such that $\lambda(t) \approx \lambda(0)$ and a parallel pursuit trajectory results, which maintains a constant λ. It is important to note that for the case where $N = \infty \to 0$, the high gain would amplify the effects of any error and delay in the output signal and so this assumes that the signal is noiseless. Finally, the mixed guidance law, PN+PP combines PN and PP to form a two parameter model and can be expressed in the form shown in equation 1.3.

$$\dot{\gamma} = N\dot{\lambda} - K\delta \tag{1.3}$$

The tuning of guidance constants when simulating the trajectories measured from bird flights can provide insights into the attack strategies of differing species. Brighton et al [10] identified that the attack trajectories of peregrine falcons in level aerial pursuit can be described by the proportional navigation (PN) guidance law.

This guidance law is commonly used in guided missiles and is characterised by turn rate that is proportional to the angular line-of-sight rate between the attacker and the target. A navigation constant (N value) of $N = 2.8$ was fitted for the flights undertaken by the peregrines in this study. In gyrfalcons, PN was also found to be the best fitting guidance model with a lower guidance constant of $N = 1.2$.

Brighton and Taylor's study [11] into the ground pursuit of erratically moving targets found that a globally fitted mixed guidance law fitted the flight data better than a proportional navigation guidance controller with a single fitted N value. Global fitting is achieved with the unique combination of guidance parameters N, K, τ that minimise the median root mean squared error between the measured and simulated trajectories for all flights. Compared with individual fitting, which obtains values of N, K and τ for each flight, global fitting reduces the risk of overfitting. This is because global fitting fits the guidance constants, of which there are three in the case of the mixed guidance law for the entire dataset, in comparison to three multiplied by the number of flights in the dataset when individual fitting is conducted. When tuning the N value for each flight using the PN guidance law, it was possible to directly compare the guidance law output to the previous study on peregrines [10]. For the two species there were clear differences in the tuning of the N value that could be attributed to their natural hunting behaviour. Peregrines were found to operate at higher values of $N \approx 3$, whereas in Harris's hawks $N \approx 1$. This lower N in Harris's hawks was found to be better tuned to predation of the species' natural ground prey because it reduces the effect that sharp evasive turns have on the bird's flight trajectory. Generally, higher tuned values of the navigation constant are better for open areas and also enable a faster interception time, whereas the tail-chase flight path resultant at lower N values allows the predator to chase the path of the prey through obstacles in a cluttered environment. Tuning of the navigation constant used in guided missiles ($3 < N < 5$) was much closer to the range found in peregrine falcons than in hawks, which also supports the previous statement since guided missiles operate over long range engagements in open areas.

In insects, Fabian et al [13] found that PN with a navigation constant of $N \approx 3$ described the attack trajectories of the robber fly (*Holcocephala fusca*) and tuning of $N \approx 1.5$ in the killer fly (*Coenosia attenuata*). Whilst both species hunt aerial prey, *Holcocephala* operates against open sky whereas *Coenosia* hunts in cluttered environments. These findings are broadly consistent with the fitted guidance constant of PN in raptors. In dragonflies, Olberg [14] hypothesised that *Erythemis simplicicollis* were executing a parallel navigation guidance strategy due to the observation that the prey was being held at a constant LoS angle to intercept; however, Mischiati et al [15] found that for *Erythemis simplicicollis* in pursuit of constant speed prey, parallel navigation only occurred reliably near prey capture and that the intercept geometry approached parallel navigation and then deviated from it. This deviation signifies that dragonfly steering is inconsistent with parallel navigation. Mischiati et al [15] also disagree with the notion that dragonfly steering is implemented with a neural autopilot based on reactive control to prey angular velocity [16] (stabilising the target on the retina) as they show the prey-image drift to drive this autopilot to be negligible and poorly correlated with prey angular velocity; ruling out reactive control models driven solely by prey movement. They gather results consistent with the use of an efference copy of wing motor commands to drive a forward model that predicts prey image drift from self-motion. They also hypothesise that an internal model of prey motion is required to predict this quantity. Overall, this study proposes that dragonfly interception is driven by 'forward and inverse models of dragonfly body dynamics and by models of prey motion'.

Despite these studies, the biological processes that mechanise target tracking and guidance in each species are still unknown. Homing missile systems have been using proportional navigation since the 1950s and it is still used today due to its ease of implementation and effectiveness [17]. A deeper understanding of the role of the visual system, eye and head movements in gaze stabilisation and tracking in target pursuit of animals might have the potential to feed into areas of bio-inspired technology; for example improvements in target tracking for autonomous aerial interception in unmanned aerial vehicles (UAVs). It might be possible to

draw from the mechanisation of proportional navigation in homing missiles to suggest how guidance is mechanised in birds and insects. In the next sections, we look to discuss these areas.

1.3 The Visual System

1.3.1 Birds

Ocular anatomy impacts the possible attack behaviours a species can perform since visual field orientation has an effect on the eye and head movements required in an animal to survey the environment and has implications for pursuit behaviour. The visual field is defined as the space around the head from which a bird can receive visual information at any one instant [18]. In engineering terminology, the field of view (FOV) of an image sensor is equivalent to the visual field of an animal's visual system. The field of regard (FOR) defines the total field of view as a result of being able to move or gimbal the visual system. This is a relevant term to animals; mechanised through the use of head or eye movements.

Raptors live in a diverse range of habitats and vary in their foraging behaviour which result in interspecies differences of their visual systems, including the visual field, eye and head movements and acuity [19, 20]. The foveae are the areas of greatest visual acuity in the retina and can occupy different angular regions of the total field of view. The number of foveae differ between raptor species, with a single central fovea found in carrion eaters, but bifoveate (central and temporal fovea) anatomy is predominantly found in diurnal birds of prey. Diurnal raptors have been shown to have the highest visual acuity among animals [1].

In the Harris's hawk, the temporal fovea is directed towards the frontal region and can provide a small region of binocular vision. Wallman and Pettigrew [21] identified the temporal foveal location in the little eagle (*Hieraaetus morphnoides*), which is in the same family as Harris's hawks (Accipitridae), to be approximately located around 5-10 degrees from the mid-sagittal plane of the head. Potier et al [22] show that Harris's Hawks are bifoveate with a total field of vision of 162 degrees and a binocular field maximum width of 47 degrees, which is much wider than

typically found in birds [18, 23]. The central fovea is directed towards lateral vision and can be assumed to be located at an angle of 69 degrees from the mid-sagittal plane. Central foveae have higher photoreceptor density than the temporal fovea [24, 25], thus indicating higher acuity.

Insects like the blowfly (*Calliphora vicina*) have a compound eye and a visual field that almost spans the whole sphere around the fly's head. *Calliphora* has a visual field with a 20° blind area at the rear of the head and a binocular region that spans 10° either side of the mid-sagittal plane of the head. Despite having spatial resolution orders of magnitude lower than raptors, insects are able to perform complex locomotor tasks such as perching and prey pursuit and capture.

1.3.2 Missiles & Flying Aerial Systems

Homing missiles sense the environment using a sensor called a seeker, which is analogous to the visual system of an animal. Active missile seekers use radar and emit pulsed RF signals to detect and track targets based on the received RF energy; whereas, passive seeker technology takes advantage of the IR radiation emitted from targets, with modern systems building an IR map of the target. There are two different types of missile seeker systems that can be categorised according to the way the seeker is attached to the missile body. A strapdown seeker is fixed to the missile body and cannot change orientation independent of missile attitude. This limits the field of view and is used in applications where a wide field of view is not required. The space-stabilised or gimballed seeker allows for increased field of regard, which effectively increases the usable field of view of the sensor with a gimbal system that allows it to rotate in two orthogonal axes; yaw and pitch [17, 26].

In robotics, cameras are the main sensor system used for the development of vehicle-to-target tracking and non-GPS navigation. Development of image tracking and object classification algorithms are made for use with camera images. Cameras provide high frame rate images with a range of pixel resolutions dependent on sensor. For target tracking and classification, better resolutions enhance classification ability at further distances; however, this increases processing requirements. Generally,

the field of view of cameras is narrow (around 90-120 degrees) and is a frustum. Wider FOV is possible, but introduces distortion to the image. At the highest resolutions, the camera still has a lower resolution than the bird's visual system and a far narrower field of view. Information regarding target tracking in these systems is limited as many details are not available in the public domain.

1.4 Gaze Movements and Mechanisation of Guidance

Shifts of gaze can be achieved through either head or eye movements, which can both be subject to active and reflexive control enabling gaze stabilisation and goal-oriented gaze shifts. In a system using a guidance law such as proportional navigation, the line-of-sight rate of the target is required to mechanise guidance. Likewise, an estimate of the deviation angle during flight is required to mechanise PP. In a missile system using PN, the gaze strategy of the seeker is key to target tracking; it maintains the target within the FOV whilst also estimating the target LoS rate as an input to execute guidance. We assume that animals use these guidance algorithms for which they would also need to estimate LoS rate and so perhaps they would use gaze strategy in a similar manner. Birds are able to detect external stimuli through the visual, vestibular and proprioceptive systems, but no work has taken place to understand the role these might have in parameter estimation or whether they use similar models to guidance laws at all. Whilst Walker [27] took measurements of the head movements of peregrines in pursuit of a lure towed behind a radio-controlled aeroplane using a GPS-IMU (GPS-inertial measurement unit) biologger, no conclusions were made regarding their gaze strategy or the mechanisation of guidance, which is currently unexplored in the literature. Here we summarise findings of gaze movements in birds, insects and the mechanisation of PN in missiles.

1.4.1 Biological Systems

Animals utilise head, eye and body movements to augment the orientation of their visual system. Walls [28] suggested that vertebrates evolved a gaze strategy to stabilise the visual scene on the retina during locomotion to remove motion blur. A saccade and fixate gaze strategy is widely used amongst vertebrates. This combines periods of fixation, which allows extraction of visual scene information, with rapid shifts in gaze, driven by head and/or eye movements which allow recentreing of gaze on a given target such that the head or eyes do reach the extremes of their movement range. Gaze stabilisation is facilitated in vertebrates by two reflexes known as the vestibulo-ocular reflex (VOR) and the opto-kinetic reflex (OKR). The VOR encodes angular position of the head from the vestibular system, which is used to produce counter rotation of the eyes to stabilise vision during head motions. The OKR is a feedback loop that is induced by relative image motion across the retina. It uses retinal motion detectors to action a response from the eye in the same direction as the stimulus to reduce image motion and causes a pattern of slow tracking and rapid resetting eye movements known as nystagmus. This reflex causes the eye to slowly track the target and must be suppressed when smooth target tracking, also known as smooth pursuit is conducted. Smooth tracking allows continual tracking of a target separated from the visual background using smooth and continuous movements rather than saccadic eye movements. It has the ability to predict future motion of the target [1]. In humans, smooth pursuit eye movements are well studied [29–31]. When performing target tracking and interception, humans have been observed to smoothly pursue the target prior to interception, which appears to reduce interception errors [32–35]. It is noted that smooth pursuit of targets moving in the horizontal plane is more accurate than those moving in the vertical plane, hypothesised to be due to poorer object motion prediction in the latter case [36]. Primates have been shown to perform smooth pursuit [37] with neural control hypothesised to be located in the frontal eye field cortex [38]. Monkeys have also been shown to learn to track a moving target using smooth pursuit [39]. The ability to perform smooth pursuit may not be

restricted to primates: studies have demonstrated smooth pursuit-like movements that closely track a visual target, maintaining it in within the fovea in blowflies [5, 40], hoverflies [41] and dragonflies [42].

In birds, gaze changes are facilitated by head movements and it is largely assumed that eye motion in birds is limited or negligible because birds use saccadic head movements in preference to eye movements due to their light and highly flexible necks [1], which allow head saccades of similar speeds to that of the human eye. Eye movements in birds are small; a study [19] on different diurnal raptors found interspecific differences in visual field configuration (degree of eye movements and binocular overlap) to be related to the behavioural differences in hunting strategy. This study found a range of eye movement in the Cooper's hawk (*Accipiter cooperii*) and American kestrel (*Falco sparverius*) between 1° and 8°. The low degree of eye movement in the American kestrel may help in image stabilisation when it is hovering above prey. It is suggested that eye movements can prevent retinal blur during pursuit. It is worthy of note that most eye movement studies have been performed with the bird restrained so movements of the eye may be exaggerated.

Eckmeier et al [43] investigated the gaze strategy used in zebra finches when negotiating an obstacle avoidance task. They hypothesised that optic flow is an ideal strategy for fast-moving animals to perform distance estimation since fast motion results in poor edge detection and image blur and this technique requires low resolution linear motion information rather than using complex features in the visual scene. It also reduces the likelihood of these birds using stereopsis also because this works for a limited spatial range and is only well developed in predators [18].

In order to extract distance to an object, translational optic flow components need to be separated from the rotational components because rotations do not provide differing image velocities/flow when there are objects at different distances. It was hypothesised that the birds would be able to process distance information from optic flow if an active gaze strategy was being employed to reduce the rotational components [43]. They found that the finches were using head saccades in a gaze strategy defined by intersaccadic periods of fixed gaze direction to separate the two

components of optic flow. Results in pigeons from Ros and Biewener [44] indicate that 'visual and proprioceptive cues are used as steering inputs for turning flight in birds'. They found that pigeons direct head saccades into the turn rather than the flight trajectory and may use head offset to reorient their body after turning.

Schilstra and van Hateren [45, 46] found that blowflies utilise head and thorax saccades in gaze stabilisation to split their flight regime into a region of straight flight where translational optic flow dominates and a turning region where the rotational flow component dominates. This reduces the blur in vision and concentrates rotational flow associated with turning in small regions of flight, such that the translational flow distance measurement can be active for the majority of the flight time. This is an example of the use of gaze strategy to enhance the basic visual system ability to effectively perform distance measurements using optic flow; enabling the blowfly to navigate its environment.

To relate studies in guidance to those on gaze strategy, I first introduce Tucker's theory. Tucker [47] proposed that since raptors possess two foveas and that studies indicate that the central fovea, which is located an angle of around 45° to the mid-sagittal plane of the head has the highest visual acuity (see more in Section 1.3), the peregrine falcon would use this to track their prey. It was also suggested that peregrines would keep their head aligned with their body to reduce aerodynamic drag, such that a spiral attack trajectory would result through use of the central fovea, leading to a deviated pursuit course with a lead angle of 45°. This suggests that the attack path is dictated by kinematic constraints from a strategy that minimises aerodynamic drag and from their visual anatomy rather than being based on a rule that uses sensory feedback. This study used static images of the head orientation of falconry birds looking at food and from published photographs of birds looking towards a photographer. This method does not provide position information of the pursuer and target and does not allow an analysis of the flight trajectory. There is also uncertainty in the method to obtain head orientation since it is difficult to ascertain whether the bird was always fixated on the food

or photographer in the images and the snapshot nature of this does not provide any information as to how the head fixation changes during flight.

Animal-borne head-mounted video cameras were used to assess the pursuit strategy in falcons [2, 48] by analysis of the prey location in the bird's visual field. Their finding that the target was often positioned in the temporal fovea rather than the central fovea provides evidence against Tucker's theory. Analysis of visual target location throughout a chase indicated that falcons would fix the target at a constant visual angle, which is indicative of the use of parallel navigation. From this visual analysis, it was also possible for Kane and Zamani [48] to observe saccadic head motion in gyrfalcon (*Falco rusticolus*)/Saker falcon (*Falco cherrug*) hybrids. These studies begin to consider sensory feedback based on target motion to explain the proposed guidance strategy. The use of head-mounted cameras enabled the acquisition of data to explain gaze strategy, but the lack of position information of attacker and target prevented a guidance modelling and understanding of mechanisation of guidance via this sensory feedback.

Guidance analyses from Brighton et al [10–12] were the first in birds to model guidance laws from GPS and high-speed camera position measurements of attacker and target; however, no sensors were placed on the head of the bird which prevented an analysis of gaze strategy. A high number of flights recorded in the studies involving GPS [10, 12] were rejected as a result of the low accuracy of the GPS loggers used. GPS loggers used throughout animal tracking studies lack the accuracy and precision required for guidance analysis. Without confidence in the position measurement, it is not possible to know whether the guidance law fit is due to the model not fitting or poor data. This presents further complication when combining position and gaze measurements, since relative position errors affect the target position in the bird's visual field, which has large implications for analysis of gaze strategy and target foveation. Walker [27] developed a GPS-IMU logger, which was deployed on peregrines in a pursuit experiment; however, poor GPS accuracy led to issues in relative accuracy between bird and target and an inability to make concrete conclusions on the birds' gaze strategy. This presents an opportunity

to combine high accuracy and precision GPS position and IMU head orientation measurements to study guidance and gaze strategy in birds.

1.4.2 Missiles & Flying Aerial Systems

In homing missile systems the gimballed seeker is able to rotate in two orthogonal axes: yaw and pitch. Roll control is determined by rotation of the missile body. The gimbal system acts to both track the target and isolate the sensor from significant body rate motion in its two axes of control much like the head-neck motor system in animals. In a strapdown seeker, the sensor array is fixed in position, resulting in a fixed look angle (FOR = FOV) of the sensor. This system indirectly calculates LoS rate from the look angle (via drift rate of the target across the sensor) but does not require a mechanism to operate. Since target tracking is facilitated through physical movements of the missile body, it effectively utilises no gaze strategy. In contrast, the gimballed seeker implements a continuous tracking gaze strategy, where the seeker is moved to keep the target at the centre of the field of view. This is based on estimation of the tracking error between the seeker centreline and the target location in the field of view. The rate of this tracking error is used to generate a yaw rate command for the seeker and so the yaw rate of the sensor is approximately equal to the LoS rate of the target. Using a gyroscope mounted to the gimbal, the yaw rate can be directly measured and used as an estimate of LoS rate to be fed into the PN guidance controller [49].

UAV systems with gimballed cameras mostly focus on aerial photography and have limited tracking function. In this function, the background is stabilised such that the video is unaffected by turbulence/gusts that disturb the dynamics of the airframe. Typically, UAV visual target tracking keeps the subject in the centre of the camera field of view; continuously tracking the target with no inertial or background stabilisation. Again, information regarding these systems are limited as many details are not available in the public domain.

1.5 What might a Bio-Inspired System Look Like?

1.5.1 Gaze Strategy in Pursuit

In the context of gaze strategy, it is hypothesised that raptors may be doing one of four options as listed below. Suggestions have been made for how LoS rate information might be estimated for the mechanisation of PN.

1. **Fixed Tracking**

   Here, the head is held fixed relative to the body and LoS rate guidance commands are generated from the drift of the target across the retina. The turning command output directs the head towards the target direction; keeping it in the FOV. This strategy keeps the head in line with the body (analogous to the strapdown missile seeker); therefore minimising drag according to Tucker's theory [47] as the body is most streamlined when the head is straight. Similar behaviour is seen in hoverflies (*Syritta pipiens*), which retract their head to the thorax during flights such that rotational movement of the visual field is due to body rotation rather than head rotation. [41].

2. **Continuous Tracking**

   The first strategy utilising gaze shifts is continuous tracking, where the target is kept at the centre of the field of vision of either fovea (Harris's hawks have two foveated regions of their retina) facilitated by continuous horizontal head movements. Target guidance information (e.g. LOS rate) is extracted directly from the head movement via the vestibular or proprioceptive systems. This method is analogous to the function of a space-stabilised gimballed missile seeker [49].

3. **Saccadic Fovea-Switching Continuous Tracking**

   Alternatively, the birds may adopt a continuous tracking technique that incorporates saccades to relocate the target from the central to temporal fovea on the same eye or for switching between central foveae on each eye. This technique may be useful for tracking the target when it is rapidly moving

across the field of vision. Here, the target is continuously tracked in the time between saccades and guidance information is determined using the same method as for continuous tracking.

4. **Saccadic-Fixed Tracking**

   Tracking of the target is saccadic with periods of target fixation where the background is held constant or the head is held fixed inertially and the guidance information (e.g. LOS rate) is determined from measurement of the drift of the target across the retina. Head movements facilitate the movement to recentre the target when it reaches a threshold point in the visual field.

1.5.2 What might be gained through the use of a bio-inspired saccadic gaze strategy?

Through the use of a saccadic fixed gaze strategy, it may be simpler to determine target guidance parameters through measurement of the drift across the sensor. This is because using a gimballed method with continuous tracking requires gaze movements to maintain the target in the centre of the camera sensor that would create a continuously changing visual background, making target classification difficult due to motion blur. Therefore, the saccadic tracking gaze strategy allows the background to be fixed, thus reducing computational complexity to detect and maintain fixation on the target.

Using this strategy, it may also be easier to identify the presence of a single moving target in a visual scene that may contain multiple targets and perform tracking. Using a fixed background allows the use of a visual landmark to stabilise the gaze until the target moves near the limits of the FOV. A gimbal movement would then allow redirection of the gaze to allow tracking to resume. However, using the saccadic technique may require reacquisition of the target if it is moving at high relative velocity across the sensor; therefore, the added complexity of feed forward control may be required to predict the next location of the target and apply gimbal movement commands. It may also be appropriate to optimise a gaze strategy between these two hypotheses that fits the constraints of an engineered system.

The most considerable constraints are the processing capabilities of embedded system hardware and the camera sensor specifications, which are much different from the visual system of birds.

Therefore, an investigation into the gaze strategy used in biological systems may be useful to both understand the physiological pathways that control guidance and to enhance the performance of visual tracking algorithms to move closer to autonomy in aerial robotic systems. This chapter highlights four key research questions that this thesis aims to answer, which are as follows: Is it possible to develop a high accuracy GPS and inertial measurement biologger for studying prey pursuit? What guidance model fits best to the trajectories of Harris's hawks in pursuit of smoothly manoeuvring targets? How do Harris's hawks direct their gaze when pursuing smoothly manoeuvring targets? What sensory information is used to mechanise guidance in the Harris's hawk during pursuit flight?

1.6 Thesis structure

In this thesis, I look to understand gaze strategy in target tracking and the mechanisation of pursuit guidance in Harris's hawks.

In **Chapter 2**, I present a method to develop a high accuracy and precision biologger which combines positional measurements from a global navigation satellite system (GNSS) receiver and gaze measurements from the bird's head using an inertial measurement unit (IMU). A post processing method to achieve such high accuracy is described, which uses a post processing method known as post processed kinematic (PPK). I validate its performance in a series of static and dynamic tests to show significant improvements over traditional GNSS loggers used in animal tracking research. This system was developed to overcome the constraints of traditional loggers which provide uncertainty in the position solution via low accuracy data. This was fundamental for guidance modelling since accurate knowledge of the position of the predator relative to its prey is required for confidence in the estimated sensory outputs used in guidance commands.

This is relevant for the development of identical GNSS loggers for use in other animal tracking studies where high accuracy and high precision positioning between a number of individuals is essential. All components and post processing software are widely available and open source.

In **Chapter 3**, I present guidance modelling for a pursuit experiment using data recorded and post processed using the biologger and methods presented in Chapter 2. A pursuit experiment was conducted in which Harris's hawks equipped with a GNSS-IMU biologger pursued a smoothly maneouvring radio-controlled car equipped with a GNSS logger. The measured trajectories from **64** flights were modelled using the three guidance laws introduced in section 1.2 and the model that best fitted the data was obtained. I find that when fitting across all flights the mixed guidance law performed the best. I compared the results to those found in our previous Harris's hawk pursuit study on erratically maneouvring targets [11] and discuss the implications of the differing fitted guidance constants.

In **Chapter 4**, I present gaze analyses for the experiment described in Chapter 3 using data recorded and post processed using the biologger and methods presented in Chapter 2. This is the first study to measure head movements of raptors during flight and assess the importance of head movements and gaze strategy in raptors and the influence this has on the mechanisation of prey pursuit. I present an analysis of the gaze strategy observed in Harris's hawks and find that the hawks use a saccadic tracking gaze strategy that maintains target fixation in a broad range of coordinates within the binocular overlap region of their visual field. I then perform guidance simulations with proxy sensory outputs for LoS rate and deviation angle derived from head gaze data available to the hawk and compare these with trajectories modelled with truth data. I find that proxies model the data well and hypothesise the physiological pathways that control guidance in Harris's hawks based on knowledge from guided missile systems.

In **Chapter 5**, I summarise and discuss the conclusions of the previous chapters and the implications of this research in the wider field. I also assess the limitations and future direction this work could take. I include details of some incomplete

work involving the implementation of proportional navigation on a small UAV as part of the future work.

2

Developing a High Accuracy, High Precision GNSS Biologger

Abstract

GPS biologging has become a mainstay of animal behaviour studies, yet few have embraced the superior accuracy available from advanced GNSS processing methods and reliability of multi-constellation GNSS. We developed a miniature, lightweight high accuracy GNSS biologger that uses post processed kinematic (PPK) for deployment in animal behaviour studies. The horizontal position error of this device was validated to be lower than 2cm for both stationary and dynamic tests; representing at least a tenfold improvement over the loggers that have been used in studies to date. The usefulness of the logger was demonstrated through deployment on a Harris's hawk and radio-controlled car in a rapid pursuit experiment. An interpolated PPK method was developed for situations dominated by lower quality GNSS data, which allows the user to obtain centimetre accuracy for short timescale events. The high accuracy results demonstrate applications to revolutionise biological experimentation involving the interaction between multiple individuals, the individual and the environment and absolute static positioning. The component cost is approximately £450 and post processing software is open source.

2.1 Introduction

The study of animal behaviour is the study of animal movement. Whether studying prey pursuit, locomotion, biomechanics, foraging, migration or social networks, it is necessary to measure movement in order to analyse the time history of the behaviour. The scale of these movements varies depending on the specific behaviour and species, so different types of measurement systems will be suited to different scales. For most outdoor studies, instruments worn by the animal are used for data capture, but video-based tracking with both static cameras and drones are options that offer minimal disturbance to the animal. There are a multitude of technologies that have been developed for the purpose of biologging, each appropriate to the study of behaviour at different spatial and temporal scales. For example, GNSS receivers, Argos satellite Doppler geolocators and light level geolocators are commonly used to provide global localisation, whereas other methods are confined to a local area of interest, such as wireless sensor networks (WSN) or radio tracking. These technologies differ in function and in the accuracy, precision, data rate and minimum sensor mass that they offer. The following presents a brief survey of the various biologging techniques that have been used to measure animal movement. We begin with a brief review of non-satellite-based techniques before a detailed review of satellite-based technologies.

2.1.1 Non-Satellite Technologies

Radio technology has been commonplace from the 1950s and 1960s under the fields of radio tracking and radio telemetry. Lord et al used radio telemetry to record frequency changes caused by respiration and wing beat of a flying duck [50], whilst LeMunyan et al developed the first radio tracking transmitter with the aim of locating released animals for wildlife management [51].

Wireless sensor networks (WSN) have been developed over the past decade, also known as reverse-GPS systems, to allow tracking and proximity sensing of small animals in complex environments unsuitable for GPS and other technologies [52]. Ripperger et al [53] developed a WSN to study wild bat flight trajectories and social

networks. They required a network of receiver nodes to be set up in the desired study area and lightweight (1g) transmitters mounted to the study species. These systems offer very good spatial and temporal resolution for the sensor mass, but are limited to a small, finite area where nodes have been installed.

Radio (or VHF) tracking and WSN use animal mounted transmitters and allow localised tracking because infrastructure is required to determine the location of the tag in the region of interest. In radio tracking, position estimates are typically obtained manually using signal triangulation; however, Kays et al [54] developed an automated system using a network of receiver towers with position accuracy of 50m to study animal movements in the Panama rainforest.

Light level geolocators (global location sensors or GLS loggers) have been used to study migratory pathways from Manx shearwater [55] to sea turtles [56]. These systems use ambient light level to determine global location; where day length is used to determine longitude and the local noon for latitude [57]. Position estimates are accurate in the range of tens to hundreds of kilometres [58] and the technology inherently offers low data rate at a maximum of two fixes per day when local noon and local midnight are used for latitude calculation. For this reason, geolocators are only feasible for very long-distance studies such as in migration, where system accuracy is insignificant compared to the distance travelled over the measurement period and data rate is unimportant. Devices such as the tag used in [59] weigh in the region of 1g, which is ideal for tracking small birds in these situations, where it is not possible to use other (heavier) technologies such as GNSS.

2.1.2 Satellite Technologies (Argos, GNSS)

The first remote global tracking system was established in the in the late 1960s and 1970s with the Nimbus satellite system [60], which was replaced in the 1980s with the Argos data collection and localisation system. Whilst radio tracking relies on a human to find and record animal locations, the Argos system provides data autonomously from radio transmitters equipped on animals that are localised from satellites passing overhead. It allows studies to be conducted over long timescales

with remote data retrieval. This system can also be used with GPS-Argos loggers to remotely transmit the GPS coordinates of tracked animals. Without GPS, these tags are very lightweight, but with few position fixes per day based on latitude (14 at the poles and fewer at the equator) and measurements with a vast range of accuracy from 150m-150km [61], this satellite system was developed for collecting data that concern long distance movements such as in migration in peregrine falcons and Swainson's hawks [62] and in the foraging ecology of northern elephant seals [63], which do not rely on significant positional accuracy. ICARUS is a development on the ARGOS telemetry and remote data retrieval system designed with the intention of creating a global small-animal tracking system [64, 65]. The deployment of the Navstar Global Positioning System (GPS) in 1993 enabled animal tracking to be conducted remotely with higher spatial and temporal accuracy than previously possible. Prior to May 2000, GPS civilian signals were subject to selective availability, which limited the potential accuracy obtainable from users [66]. The GPS satellite constellation was rapidly followed by a Russian equivalent; GLONASS and now there are four constellations that each provide global coverage. These constitute a Global Navigation Satellite System (GNSS) [67], which is the primary method for accurate global animal tracking used in biologging equipment to date.

In animal tracking, GPS was first used to evaluate moose habitat use to advise updates in forestry guidelines in Canada [68] and it has since been used across thousands of studies. Movebank has trajectory data from 5915 studies [69] and has been used to study a range of topics from collective behaviour in baboons [70] to foraging movements in Manx shearwater [71].

GNSS position is determined by estimating the pseudorange from several satellites to Earth at the user receiver, which is calculated using measurement of the emitted satellite signal propagation time. These measurements are subject to errors that degrade their accuracy; the primary error source being a result of non-synchronised clocks between the transmitting satellites and receivers. There are several methods that have been developed to reduce some of these errors, of which satellite-based augmentation system (SBAS) is one. Deployments of SBAS systems

vary from the regions they serve for example, WAAS in the USA was operational in 2003 [72] and EGNOS – the equivalent to serve Europe – was operational in 2009 [73]. The majority of GNSS biologging studies to date use receivers that use only the GPS constellation and may use SBAS depending on equipment capability, region and the date of data collection. The best horizontal accuracy available to the user is 1.4m radius CEP (50%) when using SBAS and 3.3m radius (CEP 50%) without SBAS [74, 75]. These figures are dependent on the equipment and the location it is used in. The effect of measurement error can be reduced by logging at a higher sample rate, which can also increase trajectory precision particularly when studying fast moving animals. Studies into behaviour are enhanced by additional on-animal sensors such as inertial measurement units (IMU). The information provided by the additional sensor can be complementary to improve the GNSS position solution (via sensor fusion for example) and in understanding the behaviour of interest.

GNSS tracking has been used across terrestrial and airborne species to answer varied behavioural questions. In flight research, the mathematical guidance laws that describe prey interception behaviour have been studied in peregrine falcons and gyrfalcons using trajectories recorded by GPS (SBAS) loggers at 5Hz [10, 12]. In these experiments, GPS logging was required for both the predator and pursuit target and so high relative accuracy between the two units was highly desirable. Each receiver utilised SBAS to provide 2.5m CEP spatial accuracy, so the authors used a method to align end points at interception to eliminate the effects of this error over short time scales. In testing, precision error was found to be less than 0.2m [10], resulting in good trajectory shape reconstruction; however, uncertainty in true position and drift unique to each receiver are errors that remain when using SBAS correction. Without the precision and high data rate that GNSS tracking offers, this study would not be possible.

2.1.3 Advanced GNSS correction techniques

Advanced correction techniques such as PPK and sensor fusion can be used to augment the GNSS data to improve the position accuracy, precision or both when

compared to SBAS positioning. To achieve the highest accuracy, GNSS-only processing methods use the carrier phase of satellite signals, which enables higher precision measurement when compared to pseudorange. Real time kinematic (RTK) and post processed kinematic (PPK) are carrier phase differential GNSS methods, which have been extensively explored for use in the field of robotic navigation and terrestrial surveying and mapping [76, 77]. RTK and PPK operate using simultaneous measurements between two receivers: with one on the subject (rover) and another as a static base station. Double differencing observations from two receivers almost eliminates satellite and receiver clock errors, improving the precision of positioning. When the coordinates of the static receiver are known, one can resolve the absolute accuracy of the rover receiver to the order of centimetres [78]. In RTK, corrections occur in real time, whereas for PPK, corrections are performed after data acquisition, which removes the need for a data link between the two receivers: reducing complexity and mass.

Traugott [79] developed a small sized and lightweight GPS logger for measurement of small-scale flight behaviour that uses a time-differenced post processing method to improve the precision of the position solution to decimetre level, whilst retaining accuracy equivalent to standard GPS (no SBAS). This precision enhancement enabled the sensor system to be used to understand the mechanics of upwind dynamic soaring in albatrosses [80–82]. This method is affected by GPS drift and so is applicable to correct precision over short timescale motion on trajectories from 30 second to 5-minute duration only.

PPK-GPS was used in studies by the same research lab using a custom GPS logger with inertial sensing (accelerometer and gyroscope). Haddadi et al [83] and King et al [84] used PPK to research social networks in sheep, whilst Usherwood et al [85] studied flocking behaviour in pigeons and Portugal et al [86] studied formation flight in ibises. The logger designed for the pigeons was lightweight (35g) and logged position at 10Hz. Accuracy was up to the 0.5m range after post processing [85] , whilst King et al [84], stated accuracy to 0.1-0.2m, and Portugal et al [86] stated 0.3m.

The locomotion dynamics of hunting in cheetahs was studied using custom GPS-IMU collars [87]. As in avian interception behaviour, these short scale movements require high accuracy and precision. In this case, sensor fusion between GPS and IMU data allowed an improvement in precision to 0.67m (median Kalman filter error), whilst retaining the metre level accuracy of SBAS GPS. These collars have been used in various other tracking studies [88–91], with [92] using this equipment with PPK for positioning.

More recently, RTK-GNSS was used to study social networks in sheep; a scenario that requires high spatial accuracy [93]. RTK technology enabled the interactions between close individuals to be studies as position errors in the order of 0.2m were achieved. The use of RTK is a limitation since it requires a base station with direct line-of-sight to the devices on the animals. When there is a drop in the incoming data to the rover receiver, the solution quality is degraded, which does not occur when using PPK.

As this review shows, when global positioning with high accuracy is required, GNSS is the optimal choice if the weight budget allows. GNSS technology has progressed such that it is now possible to achieve reliable single digit centimetre (0.01m) position accuracy and precision using PPK and yet this method has been relatively unused in the field of biologging. Most tracking studies do not select a GNSS device for scenarios where accuracy is an important metric. Very high spatial accuracy is fundamental in studies focused on accurate positioning between multiple individuals, accurate positioning between an individual and the environment and in absolute static positioning. Many current studies such as those mentioned above still frequently use SBAS correction and would benefit from higher accuracy absolute positioning. Although Haddadi et al [83] , King et al [84] and Usherwood et al [85] used PPK in their studies, the highest reported accuracy was 0.1-0.2m [84]. Keshavarzi et al [93] also used RTK to achieve 0.2m accuracy, but in a large sized and high mass device, not optimised for small animals. Modern PPK reduces the scale of motion over which animal movement is applicable to a minimum of around one metre.

We begin by describing a new open-source, lightweight PPK GNSS logger, for which we provide validated results demonstrating centimetre level accuracy and precision in static and dynamic tests. This is done using PPK alone and again when using a novel correction method useful when a consistent PPK solution is unavailable. We conclude by demonstrating the use and usefulness of this logger in behavioural experiments, for the test case of a Harris's hawk chasing a fast-moving target.

2.2 Materials and Methods

A high-accuracy, lightweight, wearable GNSS sensor system was developed; capable of utilising PPK differential carrier phase post processing correction via the latest in low-cost GNSS module technology. This logger was designed with the intention of studying target pursuit in Harris's hawks, where a hawk would chase a radio-controlled car to interception, whilst both were equipped with a GNSS data logger. For this application, highly accurate relative positioning (centimetre level) between the attacker and target was the primary design specification. A combination of high data rate and confidence in the accuracy of the positioning between two receivers was necessary to accommodate data collection for short time scale, energetic dynamic pursuit flight. Determination of the relative position and direction between two receivers at close range was very unreliable using standard SBAS GPS receivers with accuracy at metre level (CEP) and so PPK was the chosen processing method to ensure this accuracy requirement was met. Additionally, inertial measurement (via IMUs) was incorporated for this use case to measure head orientation of the bird for other research aims.

The bird logger (see Figure 2.1) was designed around the ZED-F9P RTK GNSS receiver (u-Blox, Switzerland) and a BT-103 L1 helical antenna (Beitian, China). Data logging and sensor communication was handled by custom software written in C using the Arduino IDE (Arduino AG, Italy) using a Teensy 4.0 microcontroller (PJRC, USA) that stored data to a microSD card. One BNO055 9DOF IMUs (Bosch Sensortec, Germany) was used with the intention of being detachable and mounted to the head of the bird (Figure 2.1). The unit used the smallest equipment

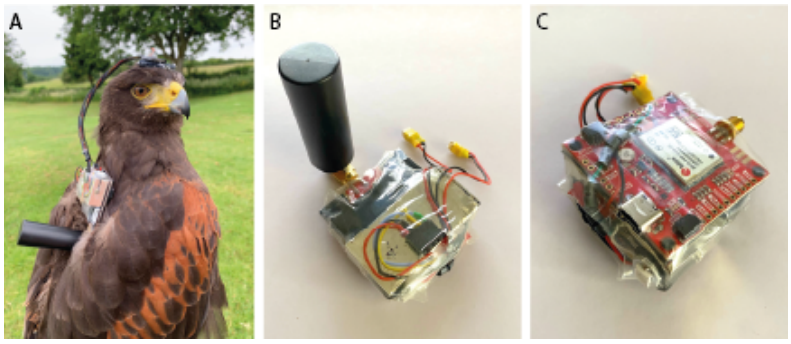


Figure 2.1: A: PPK logger fitted to a Harris's hawk with external head IMU attached and B,C: logger unit alone.

available and had a total mass of 50g formed of a back-mounted mass of 48g and head-mounted (IMU) mass of 2g, representing 4% of the total mass. The footprint of the logger was 70 x 45 x 20mm with the antenna protruding by 60mm. A backpack worn by the bird facilitated sensor attachment using Velcro.

The GNSS receiver was programmed to access all satellite L1 constellations at a sample rate of 10 Hz. The raw data required for the PPK correction was recorded in addition to the receiver's internal PVT SBAS solution (over all constellations). The IMU used was capable of outputting an internally fused absolute orientation quaternion at a maximum sample rate of 100 Hz; however, due to limitations in data save rates to the onboard storage, this was set to a sample rate of 50 Hz and run simultaneously alongside the GNSS receiver.

PPK post processing was performed with open source software RTKLIB [94], due to its capability and accessibility. We used a version of RTKLIB suited for low cost GNSS receivers and with specific support for the ZED-F9P, available via rtklibexplorer on GitHub [95]. The version used in this work was the demo5 b34d binaries, which is based on RTKLIB version 2.4.3 b34 released on 29/12/2020.

The design process, equipment choice and software architecture can be seen in greater detail in the supplementary methods in Appendix A.

2.3 Results

2.3.1 Accuracy and Precision

Accuracy defines the closeness of the position solution to the true coordinates in a reference coordinate system (e.g. WGS84, ETRS89). CEP at the 50% confidence level is commonly used to describe 2D horizontal accuracy for GNSS devices. Precision defines the repeatability of a position solution; in a static case this is represented by the closeness of each point to each other and in a dynamic case, this represents the ability of the solution to correctly track the velocity vector of the trajectory. Accuracy is most significantly affected by non-synchronised satellite and receiver clocks, but also by atmospheric errors, satellite geometry, signal multipath and receiver and antenna design, features and quality, which affect the signal propagation estimate. These errors are dynamic and cause a slow drift in the position estimate of an uncorrected solution. Antenna radiation pattern, orientation and obstructions also affect the received signal strength and therefore affect the position solution.

2.3.2 Technical Validation

Static and dynamic GNSS performance were validated by a series of experiments conducted at a triangulation pillar. The pillar has known geodetic coordinates that are measured from a top mounted 'spider' plate and height datum located at a flush bracket on the pillar's side at a vertical offset of 0.865m from the top. Knowledge of this location allowed the true sensor accuracy and precision to be determined.

The SBAS PVT (position, velocity, time) solution from the receiver was compared with the PPK solution derived from the recorded raw data that was processed using RTKLIB according to the procedure detailed in the methods. These tests were also used to select the optimal antenna for the bird logger; for which a single frequency (L1) helical antenna was chosen on the basis PVT and PPK performance in stationary and dynamic tests, low mass (11g) and good RF noise performance. Due to its performance and low-profile form factor, a dual frequency (L1/L2) patch

antenna was chosen for the radio-controlled car target. It was not possible to use a dual frequency antenna for the bird logger to due mass constraints. For more information on antenna choice, see the supplementary methods in Appendix A.

This section presents the results from the stationary and dynamic testing with several antennas. A novel correction technique termed 'interpolated PPK' correction method is introduced. This technique applies a correction to SBAS PVT data to give a position estimate with comparable accuracy to a PPK solution when a PPK solution is unavailable throughout the region of interest. It provides improved accuracy over an uncorrected PVT estimate up to around 30-minute timescales. Finally, demonstration of two GNSS loggers operating simultaneously in a Harris's hawk target pursuit experiment is presented with use of an IMU to measure head orientation.

Accuracy in Stationary Measurements

Stationary measurements were made with each sensor located in the centre of the plate atop the triangulation pillar. Each sensor remained stationary for a data collection period of 55 minutes for L1/L2 patch, 45 minutes for L1 helical and 40 minutes for L1 patch antennas. Figure 2.2 presents the recorded data for the three test antennas. The CEP was calculated for each of these antennas. For the PPK solution, this was very consistent at 0.017m, 0.011m, 0.003m for L1/L2 patch, L1 helical and L1 patch respectively. The PVT solution CEP results are better than the stated 1m from the receiver datasheet with 0.321m, 0.238m and 0.464m respectively.

These results show that a fixed PPK static solution is extremely accurate when compared to the PVT solution for all antennas. The uncorrected PVT solution showed best results for the L1/L2 patch and L1 helical antennas. It is likely that the observed PVT accuracy is an improvement over the 1m CEP stated in the receiver datasheet (47) because this was measured over the period of < 1h rather than the 24 hours of the stated figure. Nevertheless, this low CEP of 0.24 - 0.46m (antenna dependent) could be beneficial when analysing stationary measurements over reduced timescales.

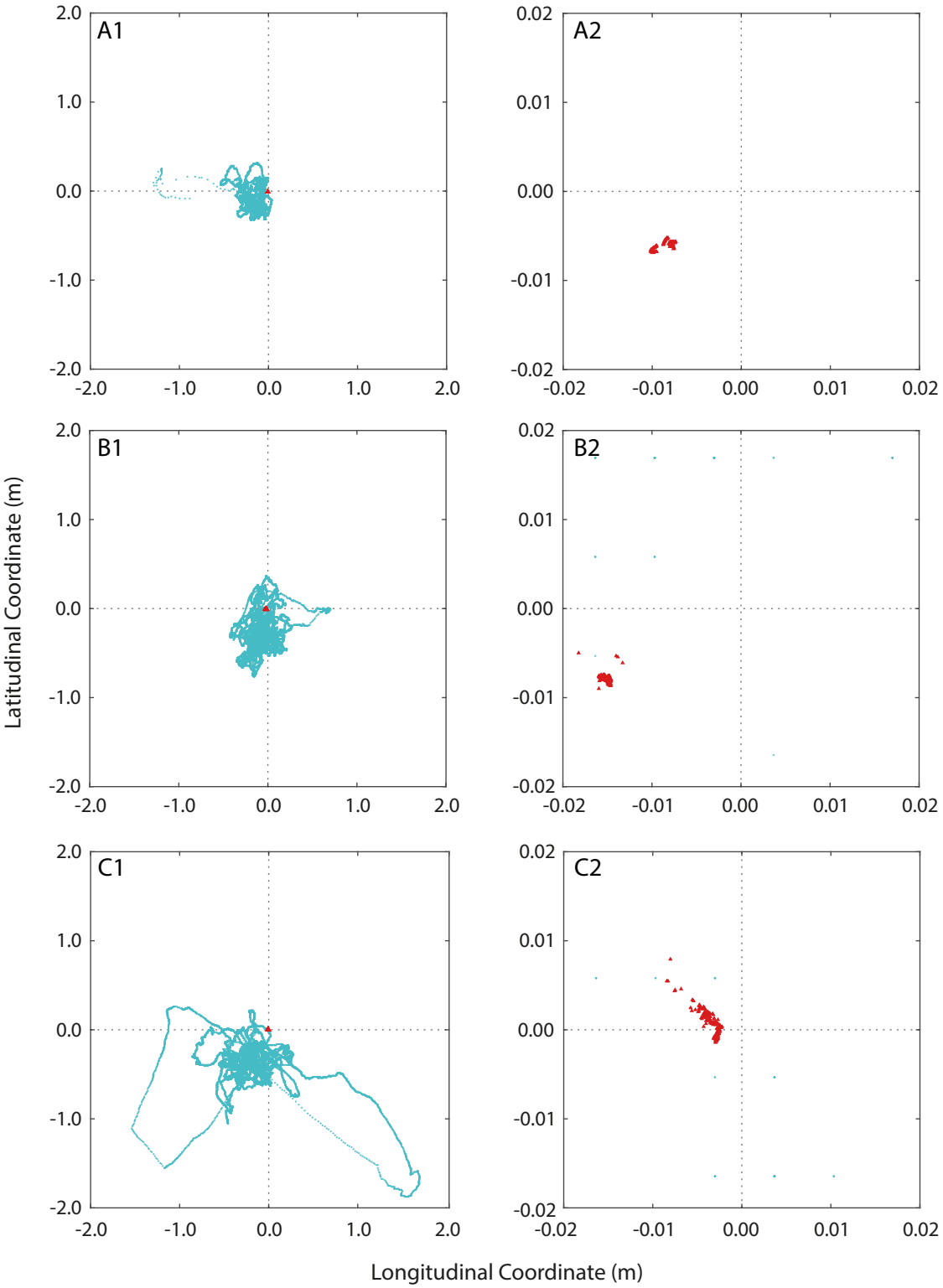


Figure 2.2: Results of static accuracy/precision experiment. A) L1/L2 Patch antenna, B) L1 Helical antenna, C) L1 Patch antenna. Turquoise (only shown in the first column) shows the uncorrected PVT solution and red (shown in both columns) shows the corrected PPK solution. Right column view (A2, B2, C2) zoomed in to view the PPK solution. Axes show the longitudinal and latitudinal position in metres as distance from the true triangulation pillar coordinate.

Dynamic Accuracy and Precision using Motorised Turntable

Measurements with the three antenna options were also made on a motorised turntable, which was centrally placed atop the triangulation pillar. The sensors were attached to the edge of the turntable at a radius of 0.19 m from the centre of rotation. Sensors were left stationary for approximately 10 minutes before and after rotation, which lasted approximately 20 minutes. The turntable speed was constant at approximately 12.5 rpm and generated a circular trajectory.

The data was post processed and the PPK solution compared to the internal uncorrected PVT solution. The following figures (Figs 2.3 and 2.4) present the results of these tests. The PPK results are a considerable improvement in accuracy and reliability throughout whole recorded trajectory over the uncorrected data, as they trace the circumference of the turntable with very low error.

However, the PVT results recorded here generally remain accurate to under 1m depending on the antenna used. Note that the circle centre of the PPK data is slightly offset from the origin, which dictates the true centre of the pillar, although, this may be a result of the antenna not being completely centred to the OS defined point despite best efforts to do so. The source of non-coincidence with the OS defined point is due to the ambiguity of the measurement point atop the triangulation pillar, since the measurement equipment used to define the OS coordinates is attached via the side of the pillar and not the top. This likely resulted in a systematic error in placement of the loggers and antennas when testing. There may also be a slight offset due to the antenna phase centre; the location in space where the satellite signals are received not being aligned with the mechanical antenna centre.

Using Pratt's circle fit method [96, 97], which outputs a fitted circle centre and radius; the centroidal error of each PPK and PVT distribution to the true triangulation point coordinate centre (at the origin) were calculated for all three antennas. For the PPK solution this was: 0.014m, 0.015m, 0.016m, and for the PVT solution, results of: 0.166m, 0.282m, 0.701m were obtained for the L1/L2 patch, L1 helical and L1 patch antennas respectively. For the test in figure 2.4, the average PPK vertical error was -0.124m and the PVT vertical error

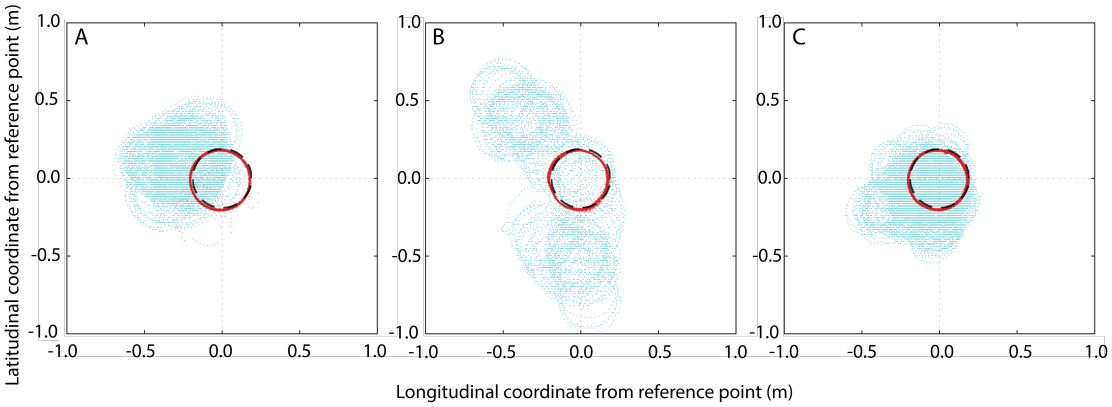


Figure 2.3: Results of dynamic testing using motorised turntable. Each subfigure shows different antenna: A) L1 helical B) L1 Patch C) L1/L2 Patch. Turquoise shows the uncorrected PVT position solution and red shows the PPK corrected solution. The black circle shows the expected PPK trajectory and centre of rotation based on true coordinates of OS pillar (x=0, y=0, R=0.19m). Dotted centre lines show the axis origin. Axes show the longitudinal and latitudinal position in metres as distance from the true triangulation pillar coordinate (reference point).

was +1.117m showing PPK offers an order of magnitude improvement in vertical accuracy, but also vastly improves the consistency over time by removing drift effects ($\sigma_{PPK} = 0.006\,m$, $\sigma_{PVT} = 0.256\,m$).

Interpolated PPK Correction Method

When deploying a GNSS sensor on an animal, it might not be possible to always achieve a fixed PPK solution. This may be due to excessive movement of the animal and antenna or sky blockage (e.g. moving under trees), which can prevent the receiver from consistently tracking the received raw satellite data that is required for the highest accuracy solution. Even when this is the case, the internal PVT solution generated by the receiver is often reliable. To compensate for the lack of a PPK fix and the inaccuracy in the PVT solution, a method termed 'interpolated PPK correction' has been proposed.

This method assumes precision in the uncorrected PVT solution from the receiver. Rotating turntable data was used to quantify this precision. The data was split into 4 second blocks, the approximate duration of a single rotation. The data for each block was shifted to the origin as a reference point and consecutive blocks were overlaid, which can be seen in Figure 2.5. The median radial error of 0.0003

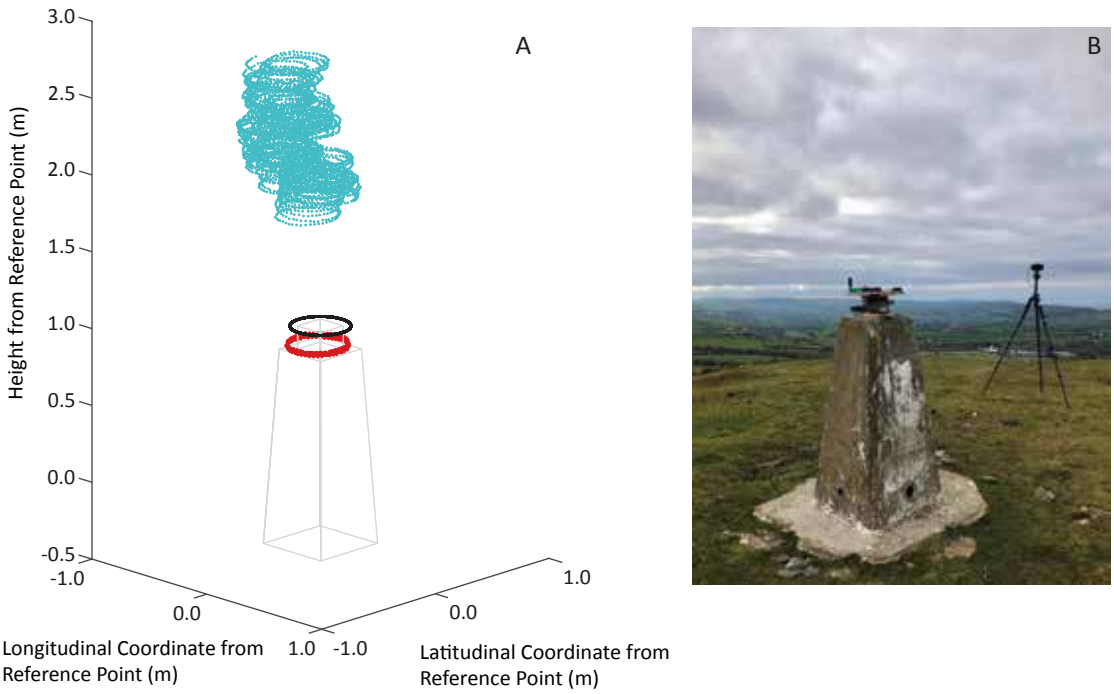


Figure 2.4: 3D plot of dynamic test with L1 helical antenna and photo of experimental setup on triangulation point. Turquoise shows the uncorrected PVT position solution and red shows the PPK corrected solution. The black circle shows the expected PPK trajectory and centre of rotation based on true coordinates of OS pillar and z-offset from height of turntable assembly (x=0, y=0, z=1.015m, R=0.19m).

m demonstrates that precision is maintained in a PVT solution even if there is considerable drift. This is the magnitude of the radial error from the origin.

In the design pursuit experiment, the bird is held stationary at the start point for a short duration before the chase begins. Once it has intercepted the target, it also remains roughly stationary until it is collected and taken to the next start location. During these stationary periods, GNSS data quality is good and a fixed PPK solution can be calculated; however, during the flight period; termed here a flight interval, it is not always possible to achieve this level of accuracy, which has been attributed to excessive antenna motion during wing flapping.

The interpolated PPK correction method uses the availability of fixed PPK data just before and after the flight interval. The closer these fixed points are to the start and end of this region, the more accurate the correction. The nearest fixed PPK data point to the start and end of the selected flight interval were used

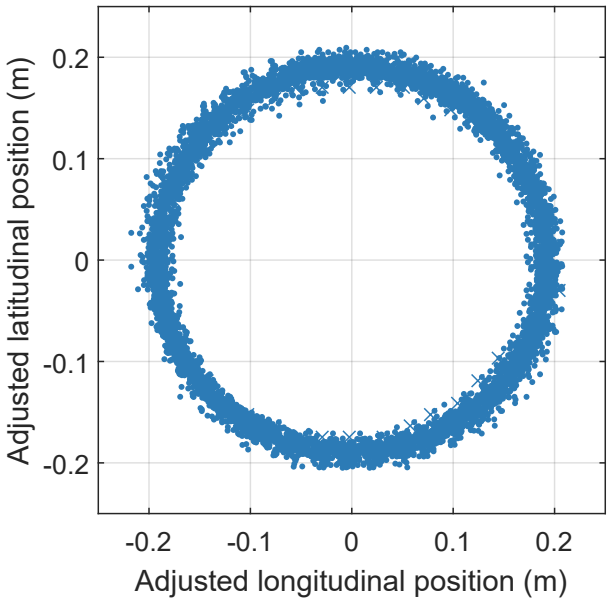


Figure 2.5: Adjusted PVT data over each 4s revolution shifted to the origin for the L1 helical antenna

to calculate the correction between the PPK and corresponding PVT solution for those two points. Each data point in the PPK solution is associated with a unique correction value. Since there is a different value of PPK correction between the start and end of the flight interval, the correction shift to be applied to the PVT data is linearly interpolated between these two values in x and y separately. This shift is then applied to the uncorrected PVT data of the flight interval of interest to align this with the PPK data.

In this dataset, PPK data was available for all flight intervals chosen, so the method could be verified. 6s was chosen as a representative timescale over which a pursuit flight occurs for this experiment and a 100 s timescale was shown for comparison. The interpolated PPK correction was applied over the recording for 198 x 6 s and 12 x 100 s windows (according to the length of the recording) and as before, a circle was fitted to the data to identify the median fitted centroid error and radius over all windows was calculated. Table 2.1 and figure 2.6 show median centroid error and fitted radius for interpolated PPK, PVT and PPK data for flight intervals of 6s and 100s.

For short timescales, the interpolated correction not only brings the interpolated distribution closer to the true PPK mean, but the interpolated shift alters the variance in the PVT data and corrects the data shape to be more representative of the true PPK solution. This method reduces the effect of satellite clock errors and the associated position drift this causes (which are assumed to be linear). The results presented in Figure 2.7 show that whilst this assumption is valid over short timescales, it does not hold over longer timescales as seen by the drift in the interpolated PPK data.

When looking at the fitted radius in Table 2.1, over the 6s flight interval a figure of 0.195m was achieved for interpolated PPK; closely matching the PPK radius of 0.193m. Whilst for the 100 s flight interval, interpolated PPK radius was 0.213m and is in accordance with the 0.215m radius for the PVT data rather than the expected radius achieved by the PPK solution. This reflects the slow drift in clock error (and/or slow changes in propagation time). For very short timescales, in the 10s range, this correction method achieves almost the same centroid and radius error as having a full PPK solution throughout. However, it highlights the need for a full PPK solution over longer timescales for absolute positioning. It nevertheless improves position accuracy over uncorrected PVT for timescales as high as 20 minutes (see Fig. 2.7) and it is estimated to be around 30 minutes where this technique fails to improve the solution centroid error.

This also shows that in this dynamic example, the PVT SBAS solution from the ZED-F9P GNSS receiver with the chosen L1 helical antenna is also very good with a median error of 0.277m. The data and results presented here are unique to the data recorded on the day including factors such as: the number of satellites in view, their position dilution of precision (PDOP), and the geographic location and proximity to the OS Net reference base station. Despite this, it gives an idea of the performance of the interpolated PPK correction, which is generally applicable in any use case to improve position accuracy over PVT positioning on the condition that a PPK fix is present either side of the recorded feature of interest and where this feature is of duration under 30 minutes.

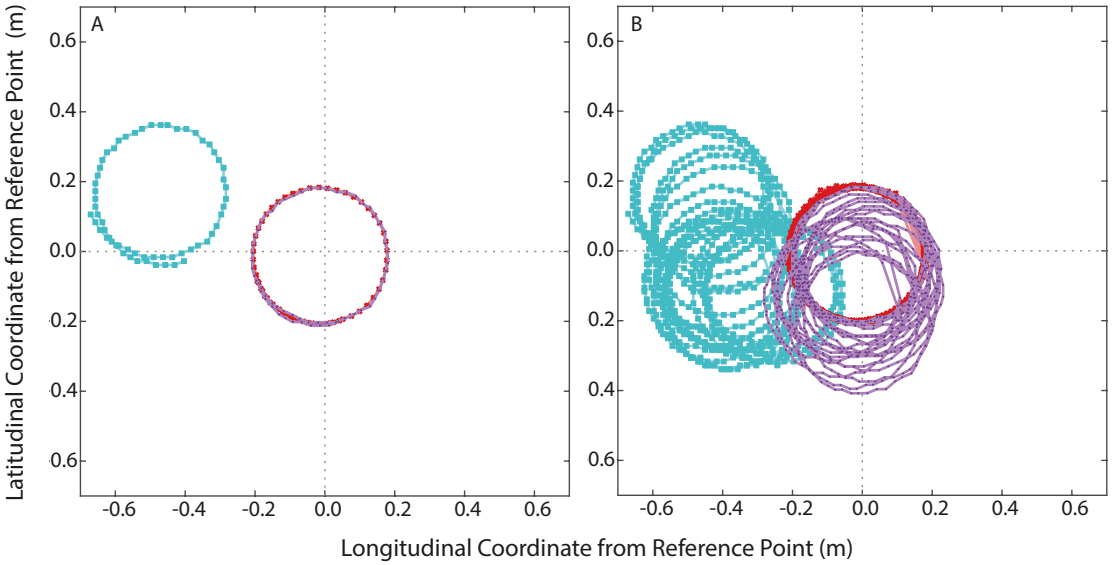


Figure 2.6: Results of dynamic testing when applying the interpolated PPK correction (purple) compared to true PPK (red) and uncorrected SBAS solutions (turquoise). A shows one window of a 6s flight interval and B shows one window of a 100s flight interval. All data shown is for the L1 helical antenna.

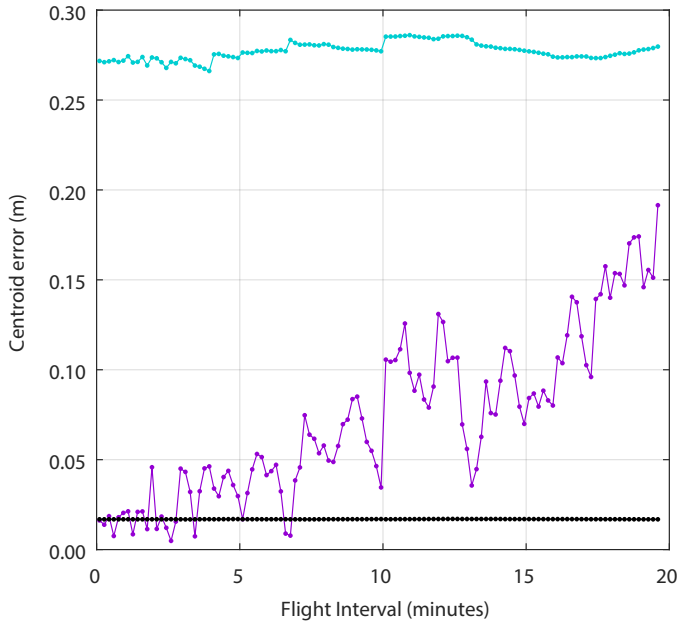


Figure 2.7: Median fitted circle centroid error for uncorrected PVT data (turquoise), interpolated PVT data (purple) and PPK reference (black) over a range of flight intervals in minutes. Average calculated over a range of repeats dependent on flight interval length.

Table 2.1: Median fitted centroid error and radius for 198x6s and 12x100s duration flight intervals when using PPK, PVT and interpolated PPK correction methods

	Median Fitted Centroid Error (m)			Median Fitted Radius (m)		
Flight Interval (s)	PPK	Interpolated PPK	PVT	PPK	Interpolated PPK	PVT
6	0.017	0.017	0.257	0.193	0.195	0.195
100	0.016	0.009	0.258	0.193	0.213	0.215

2.3.3 Pursuit Experiment with IMU Head Tracking

A logger was deployed on a Harris's hawk in pursuit of a logger-equipped radio-controlled car; here denoted as the target. The target was a lure placed at the rear of the car body at an approximate distance of 0.3 m behind the antenna. Figure 2.8 shows results of this experiment for two separate flight trials. During flight, significant antenna motion during flapping prevented a consistent lock to raw satellite data during flight, which led to the use of the interpolated PPK method for the bird trajectory and the standard PPK solution for the car trajectory. The bird's head orientation was recorded using the integrated IMU using the internal sensor fusion algorithm that outputs a orientation quaternion by combining measurements from the accelerometer, gyroscope and magnetometer. The heading accuracy of the magnetometer is ±2.5 degrees, which is not improved via sensor fusion. The accelerometer is 14 bit and has a sensitivity of 1 LSB/mg (least significant bit per milli g) whilst the gyroscope is 16 bit and has a sensitivity of 16 LSB/deg/s. In fusion mode, the IMU runs the accelerometer range at $\pm 4g$ and the rate range at 2000 deg/s. These values result in a measurement precision of 0.005 ms^{-2} and 0.488 deg/s [98]. This output is displayed using arrows at a reduced sample rate for visibility. The head IMU was attached to the birds head using velcro and in each flight trial, there will be a slight yaw offset due to the difficulty in attaching the IMU whilst the bird's head was moving. A calibration procedure was introduced to eliminate this systematic error before the first flight for each bird. Therefore, uncertainty in the head mounting should only be a unknown dynamic component from the flexure of the velcro whilst in flight. This behaviour could impact the head yaw rate measurement through mechanical damping. The low

sample rate of 50Hz was a significant source of error in yaw rate measurement in this experiment. The interception point was determined as the point where the gap between bird and target was within 0.6m. This accounts for the gap between car-mounted antenna and lure target, the bird's leg extended pose when reaching for the target and the offset between bird leg and antenna. The maximum speed for the bird in each flight was $11.0\,m\,s^{-1}$.

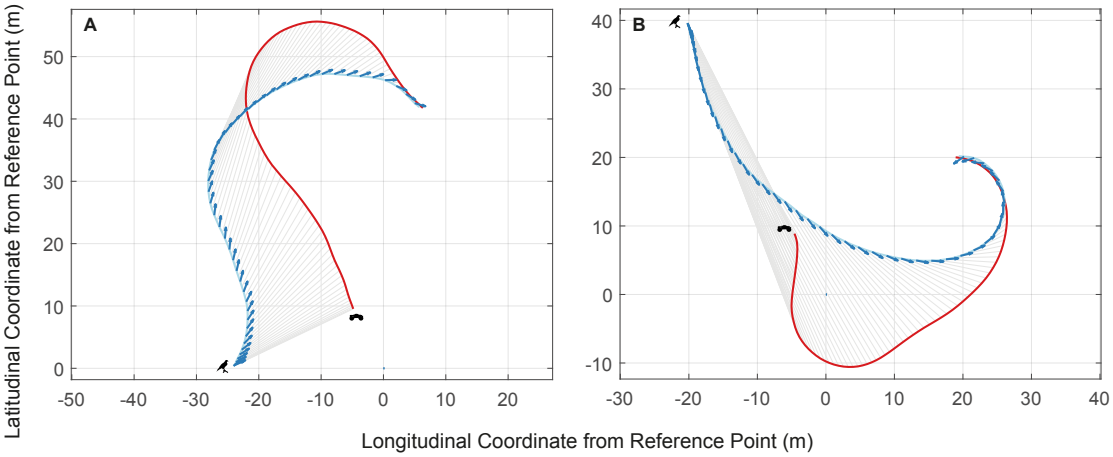


Figure 2.8: Pursuit flight data with bird trajectory from interpolated PPK data in light blue, target trajectory from PPK data in red, line-of-sight vectors in grey and bird head orientation vectors shown in dark blue for every GNSS sample. Flight start is indicated by bird and car silhouettes and interception is where the bird and car trajectories meet.

Validation of accuracy over a linear trajectory where start and end points are varied and not ground truth is difficult; particularly in an environment where large changes in acceleration are present. Figure 2.9 shows that changes in the number of satellites used in the SBAS solution (used to form the interpolated PPK result) do not affect the horizontal and vertical position errors. Although error increases slightly as the flight begins, it then stabilises for the remaining duration. The non-periodic nature of the satellite dropouts additionally suggests that the bird's wingbeat is not affecting signal reception and additionally not affecting accuracy. We then compared the velocity obtained via integration of the acceleration measured from the onboard IMU with the velocity determined from differentiation of the interpolated PPK position data and the direct velocity output from the GPS receiver PVT solution (see Fig 2.10). Acceleration was converted from local IMU axes to the

world frame using the IMU's fused orientation output and cubic spline interpolation with end conditions was used to upsample GNSS data to the same rate as the IMU data and to allow analytical integration. The same spline fit was also used to allow differentiation of GNSS data. In both flights, there is close tracking between IMU and interpolated PPK x and y velocities and IMU and PVT derived x and y velocities with correlation coefficients of 0.996, 0.994, 0.993, 0.993 and 0.994, 0.993, 0.992, 0.992 for the two flights respectively as seen in table 2.2. Speed comparison with the IMU derived speed receiver measured Doppler speed was made with correlation coefficients of 0.983 and 0.861 respectively. The observed fluctuation in the IMU derived velocities compared those derived from GPS data are a combined result of the hawk's wingbeats and head saccades which were not filtered from the acceleration before integration. In the early stages of the flight, wingbeats dominate the visible disturbances, whereas, in the latter stages of the flight, head saccades have a greater contribution as distance between attacker and target decreases and regular head motion is used in tracking.

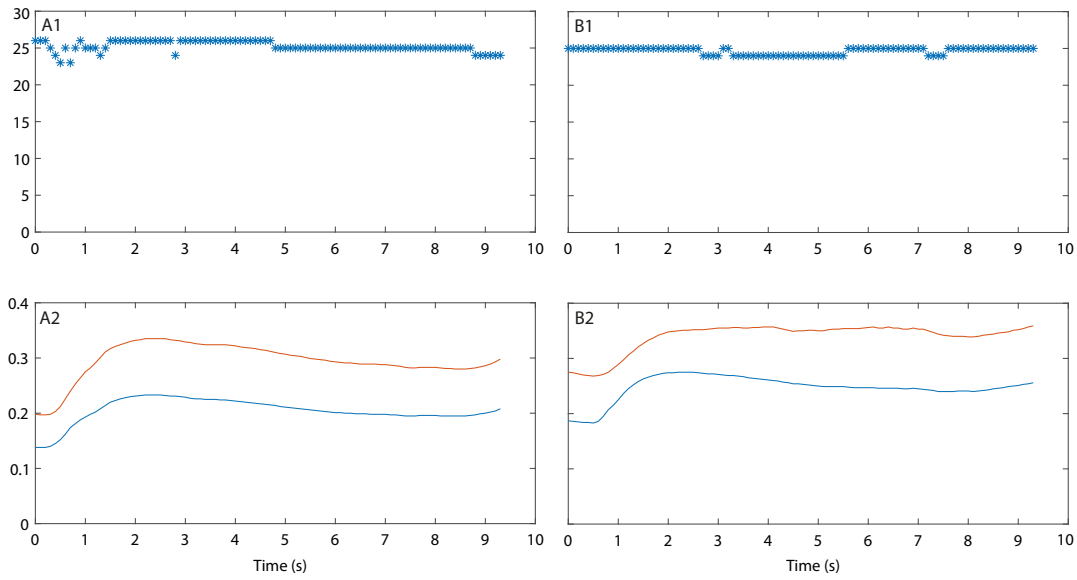


Figure 2.9: Accuracy of GNSS satellite fix. Satellite data for internal GPS receiver PVT solution for each of the two flights in Figure 8. A1, B1: the number of received satellites. A2, B2: the receiver estimated horizontal position accuracy (blue) and vertical position accuracy (red).

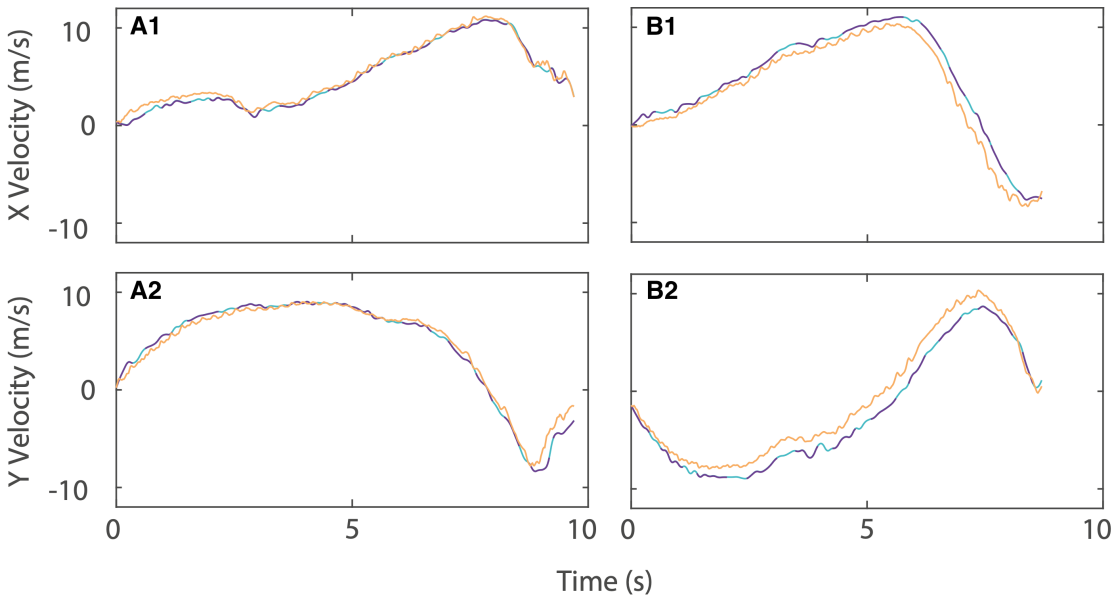


Figure 2.10: Velocity quality control from IMU acceleration data. Integration of head accelerometer data over flights A and B with A1/B1 and A2/B2 presenting x and y velocities respectively for SBAS PVT (turquoise), interpolated PPK (dashed purple) and integrated acceleration (yellow). GNSS data plotted at 10Hz, IMU data at 50Hz.

Table 2.2: Table presenting the correlation coefficients between interpolated PPK x and y velocities and IMU and PVT derived x and y velocities.

	Correlation coefficient			
	Interpolated PPK - IMU		PVT - IMU	
	v_x	v_y	v_x	v_y
Flight 1	0.996	0.994	0.994	0.993
Flight 2	0.993	0.994	0.992	0.992

This data was used in the proceeding section in guidance modelling of proportional navigation (PN), proportional pursuit (PP) and a mixed guidance law to the data captured with these loggers. To model these quantities, an estimate of the inertial line-of-sight (LoS) rate ($\dot{\lambda}$) between the pursuer and target positions and the deviation angle (δ) between the attacker's velocity vector and the line-of-sight vector is required. To understand potential error in these estimates as a result of the measured GNSS error, the standard deviation from the static accuracy tests for the PPK method and dual band patch antenna used on the target-equipped logger (Fig 2.2A2) and the interpolated PPK method and helical antenna used on the bird-equipped logger (Fig 2.2B1) was obtained. A figure for the interpolated PPK

static accuracy was determined by applying the method to the PVT results from the static test and then averaging the standard deviation in x and y separately over 52 x 6s samples equispaced throughout the dataset (since 6s intervals is a typical flight length and is used in Table 2.1 and Fig 2.6). The results are presented in Table 2.3.

Table 2.3: Standard deviation in metres for PPK method with L1/L2 patch antenna and interpolated PPK method with L1 helical antenna.

	σ_x (m)	σ_y (m)
PPK L1/L2 Patch	0.0004	0.0003
Interpolated PPK L1 Helical	0.0067	0.0074

For the flights in Fig 2.8, the estimated error in LoS rate and deviation angle was calculated using the error distribution of the two methods. Given that flights were short, the effects of satellite drift were minimal and so a constant error was randomly drawn from each distribution in x and y. This was then added to the bird and lure positions before calculating the error. The following figures (Fig 2.11, 2.12) present the estimated error in LoS rate ($\varepsilon_{\dot{\lambda}}$) and deviation angle ($\varepsilon_{\delta}$). As expected from the low standard deviation, the impact of this GNSS error is minimal and it can be seen that it has the most significant effect when the bird is closest to the target in the final stages of pursuit. During the final 1s in Fig 2.11A, the range to the target is within 3 metres and the magnitude of the deviation angle and LoS rate error is around 0.4 degrees and 1.5 degrees per second, which is within the region where guidance no longer takes place and so this GNSS error is of negligible significance to this dataset.

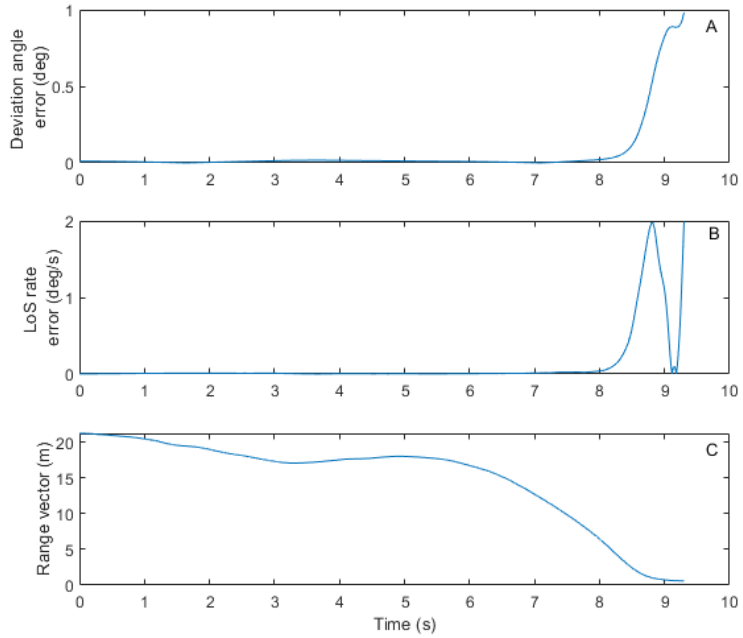


Figure 2.11: Showing the impact of GNSS error on deviation angle in degrees (A) and LoS rate in degrees per second (B) for first flight. Also presenting the range vector as the distance of the bird from the target in metres (C).

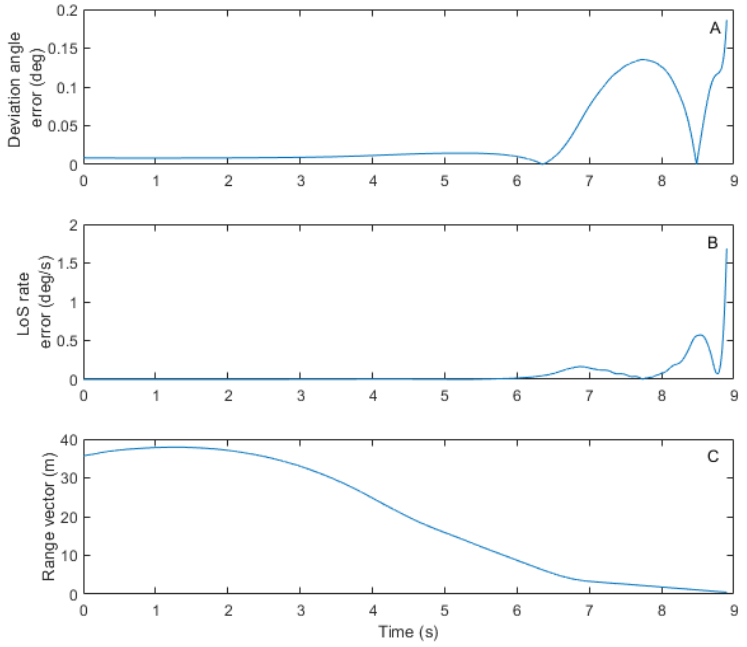


Figure 2.12: Showing the impact of GNSS error on deviation angle in degrees (A) and LoS rate in degrees per second (B) for second flight. Also presenting the range vector as the distance of the bird from the target in metres (C).

These results demonstrate the accuracy that one can achieve with a pair of these receivers using both the PPK solution if available (as on the car) and the interpolated PPK method for use when only PVT is available during the flight interval.

2.4 Discussion

2.4.1 PPK Logger Capabilities

This paper presents the design and development of a PPK GNSS biologger that can provide the user with high accuracy trajectory data for behavioural studies involving static and kinematic motion in a small, lightweight package. It is manufactured using COTS components, which result in a low cost (£450) device and the compatibility with open-source PPK post-processing software makes this a simple, viable solution for large scale deployment in biologging applications where high accuracy and precision are essential.

To the best of our knowledge, this research offers the first validation experiments of PPK accuracy and precision for biologging. It also demonstrates the first time the F9P GNSS receiver (u-Blox, Switzerland) has been incorporated into a wearable system aimed at PPK biologging. The accuracy available using multi-constellation PPK is much greater than that which can be achieved with the typical SBAS GPS receivers that have been commonly used in biology research to date. Results showed that in the configuration developed here, the ZED-F9P GNSS receiver provided high solution accuracy and precision to the user with a tenfold improvement in accuracy over previously used GNSS devices.

This technology is useful for three primary application areas in biological experimentation. These are accurate positioning between multiple individuals, accurate positioning between an individual and the environment and absolute static positioning of features in the environment.

Positioning Between Multiple Individuals

The pursuit experimentation presented in section 2.3.2 and figure 2.8 demonstrate highly accurate trajectory reconstruction between two fast moving targets in a

bird-to-prey pursuit flight onboard a Harris's hawk flying at maximum effort and provided a novel method to achieve high accuracy in the uncorrected PVT solution using the interpolated PPK correction. In this case, the interpolated PPK method was used to achieve relative positioning between the bird and target to within the expected centimetre range (due to offsets between the antennas). The inclusion of the onboard internal measurement using the head mounted IMU shows that the head orientation of the bird follows the direction of the car along the lines of sight between the two objects. Without confidence in the solution accuracy between a pair of receivers, incorrect measurements in relative positioning can adversely affect studies focused on guidance and gaze direction. In addition to pursuit, examples of animal behaviour studies that would benefit from this are flocking, courtship behaviour, social networks, and formation flight.

The interpolated PPK method was developed to enable centimetre level accuracy in regions where a fixed PPK solution was not possible to obtain. From testing, this scenario would arise when there was excessive movement of the antenna when mounted to a rapidly accelerating hawk and it will also be the case where there is any sensor sky blockage which could occur when the animal is moving under cover. We have validated the interpolated PPK method in a dynamic scenario with constant angular velocity (Figs. 2.6 and 2.7) and in a linear case with rapidly fluctuating acceleration (Figs. 2.9 and 2.10). For the second case, where motion is not about a known GPS reference point, validation was conducted through comparison of the velocity obtained from differentiation of the GPS position and integration of the IMU acceleration (Fig. 2.10). Here, we show near identical velocity tracking between the two sources.

The interpolated PPK method provides positioning accuracy comparable to a PPK solution in very short timescale events and is an excellent method for improving the accuracy of uncorrected PVT data across short timescales up to approximately 30 minutes (Figure 2.7). It also eliminates the need and uncertainty in performing and endpoint correction in a dataset where the receivers are known to be at the same location at a specific time.

Positioning Between an Individual and the Environment

Understanding the interaction between an individual and its environment is essential when studying behaviour such as: soaring flight, fine scale route following, route recapitulation, roam and search, obstacle avoidance and habitat use. Capturing data that represent these behaviours require a tracking system that is highly accurate in both stationary states and dynamic motion. Testing at the triangulation point in sections 2.3.2 and 2.3.2 validates the capability of the system to perform under these conditions. When under stationary and constant angular velocity motion, we found that the PPK solution had exceptional accuracy (0.0105m stationary and 0.0153m dynamic) and the PVT accuracy was often much improved over the 1m CEP stated value in the datasheet [99] and with very high precision. The interpolated PPK correction method also applies to these applications as shown in figure 2.6 where accuracy was identical to PPK over a 6s timescale event (0.02m).

Absolute Static Positioning of Features in the Environment

Absolute static positioning is another scenario where PPK can provide valuable measurements for experimentation. Already used extensively in terrestrial surveying and mapping, use of a PPK GNSS receiver could be used to map key features such as landmarks, obstacles, locations of specific equipment (anemometer etc) and start/end locations. It could be used to map the location of plants or other environmental features to centimetre level once or in a temporal study. Stationary position error was measured reliably to a triangulation point with known position to an average of 0.01m over the three antennas tested (see section 2.3.2 and figure 2.2).

2.4.2 Trade-offs in GNSS Technology Selection

When deciding upon the most appropriate GNSS positioning technology to use, there are two primary options to choose between; PPK and SBAS. Within the envelope of each are receivers that offer single or multi-constellation, single or multi-frequency signal reception – which are factors that significantly affect performance – in addition to variable data rates for each operational mode.

In the described pursuit experiment, it may also have been possible to measure the body trajectories using 3D photogrammetry which was used in measuring hawks in Brighton and Taylor [11]. This method uses a set of calibrated camera pairs spaced at a set distance apart to reconstruct 3D trajectories of multiple targets in a captured area. The error on the GNSS loggers described in this work is comparable with the estimated error from photogrammetry (however this was recorded in a smaller volume), where they found a static error of 0.02m compared with the 0.01m found in this study using PPK. GNSS has the benefit of having homogeneous accuracy, whereas the accuracy of photogrammetry reconstruction is dependent on the range of the target from the cameras and no ground truth measurement is output. Photogrammetry also requires a significantly large point target to track, otherwise, it is unclear whether the same point on the animal is being tracked frame to frame. This method therefore requires significant set up time, synchronised cameras and an increasing number of cameras to cover an increasing experimental area and required accuracy. For example, Brighton and Taylor [11] required 4 cameras to cover an experimental volume of 50x20m. Using an accurate GNSS system, which can be deployed anywhere with limited set up overhead poses a significant benefit for the experiment presented here. However, if the measurement volume is small, photogrammetry could be a good method to measure body trajectories to high accuracy and could allow for smaller species to be measured.

At the present, multi-constellation PPK GNSS is the optimal technology for biologging applications that depend on obtaining absolute accuracy and confident positioning between individuals. For studies where this level of position accuracy is not required, using the internal multi-constellation SBAS PVT position solution would be most suitable. Successful use of the high precision PVT solution is demonstrated in the interpolated PPK method presented in section 2.3.2.

The primary disadvantages to PPK technology are the system mass, high data throughput and necessary proximity of the receiver to a reference base station. The PPK GNSS logger developed in this study was around twice the mass of an SBAS GPS logger that it replaced (whilst offering significant accuracy improvements).

This limits the size of the animal on which it can be deployed. In this study, electromagnetic interference (EMI) was a constraint that affected the antenna choice and therefore minimum mass and size of the logger. With high data throughput, power consumption affected battery choice; adding mass to meet record duration requirements. With further development, it is likely that a smaller and lighter system could be produced, but it would not likely be possible to service animals with a mass below 0.5 kg with the current technology. For absolute solution accuracy, proximity (within 20 km) to a regional reference base station is essential. With these stations typically sparsely distributed throughout the country, there are locations with no coverage and this level of solution accuracy is not possible. This is a particular limitation for studies involving pelagic birds for example. However, for locations and countries where a base station is unavailable, it is still possible to enable cm level relative accuracy using PPK with the implementation of a local base station in a known location. With this, all measurements are made relative on the baseline to the local base receiver. This is a reliable method for performing relative measurements between multiple individuals equipped with separate GNSS loggers.

The primary disadvantage of SBAS positioning is the inability to obtain absolute positioning and the position drift that occurs over the duration of a recorded trajectory. Whilst SBAS system performance can be successful using smaller and lighter receiver and antenna components, it should be noted that the performance of the SBAS solution obtained in this study is in part due to the optimised receiver and antenna and elimination of EMI. However, from testing, this had a greater impact on the locking of raw satellite data used in the PPK solution rather than the internally generated SBAS solution. With system optimisation, validation results here show that dynamic precision and static accuracy are good and is a suitable option for studying long range movements.

This paper develops the first lightweight PPK GNSS logger system designed for accurate animal tracking that utilises open-source software and COTS hardware. PPK GNSS technology offers the ability to answer biological questions that could not be previously answered. The scope of questions that consider interaction of multiple

individuals, the individual and the environment and questions that consider absolute static positioning are widened with the realisation of <0.02 m accuracy in both static and dynamic motion. The static and dynamic GNSS validation enables confidence in the position solution when deployed on animals and highlights the need to validate receiver accuracy and precision independent of the GNSS technology used.

The method to reproduce the developed logger system has been outlined and the software architecture supports IMU sensing in addition to PPK GNSS. This could be easily modified to incorporate data inputs other than inertial sensing as required for the specific experiment.

Stability of the antenna during experimentation is very important in acquiring the best raw data for PPK analysis; however, if fixed PPK solution data is intermittent, the interpolated PPK method presented here can recover the accuracy offered by the PPK solution without needing to rely on a solution fix throughout the whole dataset.

3

Guidance Modelling of a Harris's Hawk in Pursuit of a Smoothly Manoeuvring Target

Abstract

Aerial predators rely on accurate visual guidance when tracking and intercepting prey. For birds with a variety of prey species, does tuning of this guidance control 0system vary and how robust is it to perturbations such as wind? Here we used precision GPS loggers to record the attack trajectories and identify the guidance law of n=5 Harris's hawks (*Parabuteo unicinctus*) chasing smoothly manoeuvring artificial targets, which were then compared to existing flight data of Harris's hawks intercepting erratically manoeuvring targets. We found that the mixed guidance law (PN+PP), which commands turning proportionally to a linear combination of the angular rate of the line-of-sight to target at guidance gain N and the deviation angle between the velocity vector and the line-of-sight to target at guidance gain K best modelled the data with a higher value of N, a higher N to K ratio and a significantly lower sensorimotor delay. We attribute these tuning differences to the predictability of the smooth target and visual filtering in the bird to predict the location of the target. We also tested several alternative versions of the mixed guidance law in an attempt to better model flight in wind; however, we found the standard mixed guidance law formulation is robust to wind.

3.1 Introduction

The success of an aerial predator is reliant on its ability to guide a path to intercept their prey. It is possible to represent the interaction between predator and prey as a two-particle problem and use the guidance laws implemented in missile literature [17] as behavioural algorithms in birds to model target tracking and interception.

Guidance laws have been fitted to characterise prey pursuit of aerial targets in peregrines (*Falco peregrinus*) [10], gyrfalcons (*Falco rusticolus*) [12] and in Harris's hawks (*Parabuteo unicinctus*) in pursuit of erratically manoeuvring ground targets [11]. The measured flight trajectories of these three raptors were modelled by three guidance laws; proportional pursuit (PP), proportional navigation (PN) and a mixed guidance law (PN+PP), which combines the properties of both PN and PP. These use sensory outputs available to the birds through the visual, vestibular and proprioceptive systems and command a motor output in the form of the bird's turn rate. A PN guidance law commands turning proportionally to the time derivative of the line-of-sight vector ($lam\dot{b}da$) that is constructed between the positions of the attacker and target as ($\dot{\gamma} = N\dot{\lambda}$), where N is the navigation constant and is assumed to be constant throughout the flight. A PP guidance law commands turning proportionally to the deviation angle (δ) between the attacker's velocity vector and its line-of-sight to target as ($\dot{\gamma} = -K\delta$). The PP gain, K is also assumed to be constant throughout the flight. The mixed guidance law is a linear combination of PN and PP as ($\dot{\gamma} = N\dot{\lambda} - K\delta$).

To identify the guidance law that best fits the measured behaviour, the combination of guidance parameters (N, K, τ) that minimise the error between measured and simulated trajectories are found. The implication of this is that different behaviour can be modelled using different parameter tuning of the same guidance law and therefore be compared across species. Whist the attack behaviour of peregrines and gyrfalcons were best modelled by the same proportional navigation law with differing parameter tuning, attack behaviour of Harris's hawks was best modelled by a mixed guidance law. This law combines proportional navigation, which leads to an intercept trajectory and proportional pursuit, which promotes

tail chasing to the target. These findings are expected given the differing hunting behaviour of the three species. Whereas peregrines and gyrfalcons hunt avian prey in open environments, Harris's hawks are specialized ground hunters often operating in cluttered environments. Brighton and Taylor [11] found the best-fitting parameters of the mixed guidance law of Harris's hawks when in pursuit of erratic ground targets to be $N = 0.7$ and $K = 1.2$. The erratic target behaviour is characterised by abrupt inflection points in the measured trajectories caused by target motion with high jerk and the guidance parameter tuning suggests that these model parameters are optimised for unpredictable target behaviour for two key reasons. The first is that the low N values reduce the steering command amplification caused by unpredictable turning of the target and make it less likely for the hawk to be thrown off course [11] and secondly, the higher ratio of K to N promote the characteristics of the PP part of the model, leading to tail chase trajectories.

Harris's hawks are widely distributed between the Southern US, Mexico and South America in semi-open desert scrub, savanna, grassland, and wetland habitats and feed on medium sized mammals (*Leporidae*), small birds and lizards [100]. This diversity in prey species and habitat suggests that the hawks must adapt their hunting strategy, specifically their guidance system to successfully pursue targets with differing evasive behaviour. Given this and the findings from Brighton and Taylor [11], we hypothesise that Harris's hawks are able to adapt their guidance based on target behaviour. In this study we assess the fit of a guidance law that best models Harris's hawk pursuit flight to a smoothly manoeuvring target and compare the results to our previous study in these birds [11].

We measured N=61 pursuit flights from n=5 birds chasing a food lure target fitted to a radio-controlled car using custom precision Global Positioning System and Inertial Measurement Unit (GPS-IMU) loggers. Previous work has used inaccurate measurement technologies; however, in this work, positional accuracy is guaranteed by high system (logger) accuracy and IMU cross validation. We used the IMU to perform velocity quality control on the GPS measurements (see Methods), which resulted in a sample size of 54 flights. This equipment and process

reduces the uncertainty in the position measurement and therefore in guidance modelling, ensuring that poorly fitting models are not a result of questionable data. The measured trajectories were used to simulate the bird's path modelled using the three different guidance models PN, PP, PN+PP and the best fitting model and associated parameters were found. We found that Harris's hawks pursuing smoothly manoeuvring targets are best modelled by the mixed guidance law with different parameter tuning to that found when in pursuit of erratic targets. With wind measurements recorded on the day using a 3D sonic anemometer, we then investigated whether the identified optimal mixed model is suitable for simulating pursuit trajectories when wind is present and whether a new model based on first principles can better model this behaviour in wind.

3.2 Materials and Methods

3.2.1 Experimental Design

We flew n=5 captive-bred Harris's hawks (*Parabuteo unicinctus*) at a smoothly manoeuvring target simulating a fast-moving ground prey item. The birds consisted of 4 males and 1 female, having mass that ranged between 0.62 kg - 0.84 kg during experimentation. A meat lure attached to a Savage XS (HPI Racing, Denmark) radio-controlled car was used as the pursuit target. Tests were conducted at the cricket pitch in Wytham, UK. For each flight, the target start direction was randomised from one of four perpendicular directions and the bird start location was randomised from one of three directions relative to the target's start position (avoiding the scenario where the car exits towards the bird). The target start location was fixed over all flights and was concealed in a box such that the bird did not anticipate the exit direction prior to start. The experimental setup is depicted in figure 4.1 below. For each flight, with the car concealed in the box and the bird at the start position, the car would start first before the bird took off from the falconer's glove. The flight would continue until the hawk intercepted the lure and then the bird was retrieved and moved to the next start location whilst the car was returned to the box.



Figure 3.1: Schematic of experimental setup and inset photograph from flight trials. This shows the car start position in the centre of the Wytham cricket field that was hidden inside a box with 4 potential exit directions labelled 1-4. The 4 random bird start positions are labelled as orange dots and also labelled 1-4 at a constant 30m from the box. The inset figure shows the falconer holding the bird before takeoff with the car box in view.

Each bird flew a maximum of 3 consecutive flights per day leading to a possible total of 15 flights per day across all individuals. The total dataset consisted of 61 flights before IMU and wind based quality control. The car was driven manually in an evasive trajectory with smooth turning. Turn rates were limited by the performance envelope of the car. The car's speed was modulated based on the performance of the bird; as such it was reduced if the bird's speed dropped to motivate it to continue pursuit. For the fittest individuals, the maximum speed was not sufficient to outpace them. The bird start position was set at an offset of 30m from the target.

3.2.2 Instrumentation

The hawks were fitted with a custom designed post processed kinematic (PPK) GNSS-IMU biologger, comprising a GNSS receiver and external IMU attached to the head of the bird. An identical logger was placed on the car. This was attached to the bird with a falconry harness, which uses a plastic mounting plate held between the shoulders by a pair of Teflon ribbons drawn once around the bird's body in a figure-of-eight. A local GNSS base station also using an identical GNSS receiver was placed at a fixed location on the cricket strip for GNSS post processing and to provide a fixed reference for calibration of the head IMU. These loggers recorded GNSS position data at 10Hz and IMU data at 50Hz.

A PPK GNSS solution is a post processing method that enables high precision and centimetre-level accuracy to the ground truth and relatively between two receivers. This operates using a moving receiver (bird/car) and a static base station receiver concurrently to reduce satellite and receiver clock errors. For data recorded from bird-mounted loggers, an interpolated PPK technique was developed to recover centimetre accuracy from the internal receiver SBAS position solution over short timescales. This uses a linear correction that interpolates between the endpoint offset between PPK and SBAS positions in the stationary region either side of a flight to correct the position of the SBAS data.

3.2.3 GPS Data Processing

A pre-processing pipeline was developed to analyse the raw data obtained from all sensors and output synchronised bird and lure GNSS trajectory data for each flight.

GNSS data was first PPK post processed using RTKLIB; an open-source program for GNSS positioning [94, 101]. Bird and target GNSS data were processed using the Kidlington (OXFR) Ordnance Survey OSNet antenna [102] as the reference base station, which was located within 6km of the study site. The GNSS receiver outputs coordinates in the WGS84 reference coordinate system, whilst the OSNet reference antenna RINEX files output coordinates in ETRS89 reference frame. To process the

PPK solution in the same coordinate system, the position of the reference antenna was converted to WGS84 for processing in RTKLIB.

For this data, which was collected in 2021, an ETRS89 to WGS84 coordinate transformation is equivalent to an ETRF97 e2009.756 to ITRF2008 e2021.5 conversion. This was done using the EUREF Permanent Network (EPN) coordinate transformation tool [103]. To convert between epochs (e2009.756 to e2021.5) as well as reference frames (ETRF to ITRF), it is necessary to estimate the tectonic plate velocities, which was done using the UNAVCO calculator [104]. For this, the NUVEL 1A tectonic plate motion model with no net rotation (NNR) was used.

The SBAS and PPK position data were converted from the geodetic reference frame (longitude, latitude, height) with units in decimal degrees and height in metres to the local tangential ENU coordinate reference frame with units in metres using the base station positioned on the cricket pitch as the origin. A flight velocity quality control procedure was used to ensure that the average velocity extracted from differenced position was within a threshold of the measured Doppler ground speed.

The interpolated PPK correction was run on the bird SBAS position data and the PPK position was used for the target trajectory. All data was output from bird flight start until the point of target interception. Flight intercept timing was based on a 0.6m threshold distance between the measured bird and lure positions. A value of 0.3m accounted for the distance from target antenna to the position of the lure on the radio-controlled car and an additional 0.3m was used to account for leg extension, and position offset of the GNSS antenna on the back of the bird. When the bird was in the catch phase within this threshold, it was concluded that guidance had ended and so it was taken as the end point for simulation. This process was also used as a quality control check to discard any flights where the bird and lure were not present within the threshold. An independent velocity quality control check between integration of IMU acceleration and differentiation of GNSS position was used to remove flights that did not meet a correlation threshold of > 0.8. After all quality control, a total sample of n=54 flights was obtained for guidance simulation.

3.2.4 Wind Measurements

Wind speed was measured using a 10Hz 3D sonic anemometer (Windmaster, Gill Instruments, Hampshire, UK) at a single fixed location in the experimental area. For each flight, the average wind speed was calculated over the flight duration for use in analyses. This was done to account for static measurement since the wind experienced by the anemometer was not the wind experienced by the bird at that moment in time. Wind data was missing for 4 flights and so the sample size for wind guidance fitting was n=50 flights.

3.2.5 Guidance Simulations

The guidance simulations processed in this work are based upon 2D planar motion in which the geometric and kinematic equations are written in the inertial reference frame. The simulation method used is the same as that developed by Brighton & Taylor, 2019 [11], from which the remainder of this section is drawn. The line-of-sight vector or range (r) between the pursuer (P) and the target (T) defines the distance between the two objects and the line-of-sight direction directed from P to T. Using the simulated position vector of the pursuer ($\boldsymbol{x}_P$) and the measured position vector of the target ($\hat{\boldsymbol{x}}_T$), the line-of-sight vector can be defined as:

$$\boldsymbol{r} = \hat{\boldsymbol{x}}_T - \boldsymbol{x}_P \tag{3.1}$$

and the closing velocity $\boldsymbol{v}_C$ as:

$$\boldsymbol{v}_C = \boldsymbol{v}_P - \hat{\boldsymbol{v}}_T = -\dot{\boldsymbol{r}} \tag{3.2}$$

For a constant velocity, the centripetal acceleration of the pursuer ($\boldsymbol{a}_P$) can be written in relation to the turn rate extracted from the guidance law in vector form as:

$$\boldsymbol{a}_P = \dot{\boldsymbol{\gamma}} \times \boldsymbol{v}_P \tag{3.3}$$

The line-of-sight rate (ω) can be written in vector form as:

$$\boldsymbol{\omega} = \frac{\boldsymbol{r} \times (\hat{\boldsymbol{v}}_T - \boldsymbol{v}_P)}{|\boldsymbol{r}|^2} = \frac{\boldsymbol{r} \times (-\boldsymbol{v}_C)}{|\boldsymbol{r}|^2} \tag{3.4}$$

The deviation angle δ is given in vector form as:

$$\boldsymbol{\delta} = \left(cos^{-1} \frac{\boldsymbol{r}.\boldsymbol{v}_P}{|\boldsymbol{r}||\boldsymbol{v}_P|} \right) \left(\frac{\boldsymbol{r} \times \boldsymbol{v}_P}{|\boldsymbol{r} \times \boldsymbol{v}_P|} \right) \tag{3.5}$$

The forward Euler method is used to solve the guidance equations in discrete time using the following two difference equations:

$$\boldsymbol{v}_{P_{n+1}} = \hat{v}_{P_{n+1}} \frac{\boldsymbol{v}_{P_n} + \Delta t\, \boldsymbol{a}_{P_n}}{|\boldsymbol{v}_{P_n} + \Delta t\, \boldsymbol{a}_{P_n}|} \tag{3.6}$$

$$\boldsymbol{x}_{P_{n+1}} = \boldsymbol{x}_{P_n} + \Delta t \boldsymbol{v}_{P_n} \tag{3.7}$$

Where $\hat{v}_P = |\hat{\boldsymbol{v}}_P|$ denotes the actual measured ground speed of the attacker and where the subscript notation indicates the values of the variables at successive time steps, such that $t_{n+1} = t_n + \Delta t$.

In equation 4.5, the centripetal acceleration $\boldsymbol{a}_{P_n}$ commanded by the guidance law is first used to determine the direction of the simulated velocity at the next time step. The magnitude of the rotated simulated velocity vector $\boldsymbol{v}_{P_{n+1}}$ is then normalised to match the actual measured speed of the bird $\hat{v}_{P_{n+1}}$. In equation 4.6, the simulated velocity is then used to calculate the simulated position of the attacker at the next time step $\boldsymbol{x}_{P_{n+1}}$ as commanded by the guidance law.

The step size Δt in the simulations was made small enough to guarantee the accuracy of the fitted guidance parameters and the prediction error to the level of precision at which they are reported. A process shown below was used to obtain the value of the time step $\Delta t = 3.33 \times 10^{-4} s$.

3.2.6 System identification

Guidance simulations were run on a sample size of 54 flights (50 for wind analysis) with a range of values of N, K and τ for each guidance law; PP, PN and PNP. Initially, a coarse fit was run with values of guidance constants N and K in the

range $[0.2 : 0.2 : 6]$ and tau in the range $[0 : 0.02 : 0.2]s$ with a step size of $\Delta t = 3.33 \times 10^{-4} s$. These values were chosen as reasonable values for bird guidance based on previous studies on Harris's hawks and peregrine falcons [10, 11]. Each delay (τ) represented a time shift between the bird and lure trajectories, which were simulated from $t = \tau_{max}$ (here $\tau_{max} = 0.2\,s$) to the end of the flight to ensure that the same section of the flight was simulated independent of the delay for a particular run. For each set of N, K and tau, the prediction error ε was calculated, defined as the mean absolute distance of between the measured ($\hat{\boldsymbol{x}}_P$) and simulated positions ($\boldsymbol{x}_P$) of the bird at each time point (n):

$$\varepsilon = \frac{1}{k} \sum_{n=1}^{k} |\boldsymbol{x}_{P_n} - \hat{\boldsymbol{x}}_{P_n}| \tag{3.8}$$

To determine the global optimum, the unique combination of N, K and time delay τ that minimised the median prediction error ε over all flights was identified using the results of the exhaustive search of N, K and τ as above. Once it was observed that the optimum values lay within the parameter space identified from the coarser fit, the optimisation was run with a smaller interval between values. N, K and τ were refined within the ranges between $N, K = [0.2 : 0.05 : 3]$ and between $\tau = [0 : 0.005 : 0.1]s$. If the optimum parameters were situated at a boundary in the parameter space, a larger range would be first tested before refinement.

3.3 Results

3.3.1 Guidance Modelling

The hawks' measured flight trajectories were simulated using a forward Euler method with three guidance laws: PP, PN, PN+PP, which generate a centripetal acceleration command. In this dataset, birds flew approximate planar interception trajectories with vertical deviations of less than 3m. The guidance simulations processed in this work are therefore based upon 2D planar motion in which the geometric and kinematic equations between pursuer, P and target, T are written in the inertial reference frame. Equations are written in general 3D vector form. For

a constant velocity, the centripetal acceleration of the pursuer can be written as: $\boldsymbol{a}_P = \dot{\boldsymbol{\gamma}} \times \boldsymbol{v}_P$, where $\dot{\boldsymbol{\gamma}}$ is the turn rate vector commanded by the guidance law and $\boldsymbol{v}_P$ is the pursuer's velocity vector. In the guidance equations below, line-of-sight rate, $\dot{\lambda}$ and deviation angle, δ are lagged by a delay $\tau \geq 0\,s$ to simulate sensorimotor delay. Proportional navigation commands turning proportionally to the line-of-sight rate between the pursuer and target. The acceleration commanded by proportional navigation at time t can therefore be written as:

$$\boldsymbol{a}_P(t) = N\omega(t-\tau) \times \boldsymbol{v}_P(t) \tag{3.9}$$

where N is the navigation constant, ω is the vector form of line-of-sight rate at time $t-\tau$ and τ is the sensorimotor delay. This is the definition of pure proportional navigation (PPN). Proportional pursuit commands turning proportionally to the deviation angle, $\delta = \lambda - \gamma$ between the attacker's velocity vector and line-of-sight to target. The acceleration commanded by proportional pursuit at time t can be written as:

$$\boldsymbol{a}_P(t) = -K\delta(t-\tau) \times \boldsymbol{v}_P(t) \tag{3.10}$$

where K is the guidance constant and δ is the deviation angle vector at time $t-\tau$. Under the mixed PN+PP guidance law, elements from PP and PN are combined to command the pursuer's centripetal acceleration as:

$$\boldsymbol{a}_P(t) = N\omega(t-\tau) \times \boldsymbol{v}_P(t) - K\delta(t-\tau) \times \boldsymbol{v}_P(t) \tag{3.11}$$

See Fig. 4.2 for a definition of the angles that define the geometry of pursuit in the inertial frame. Simulations were run given knowledge of the attacker's initial position and velocity and the time history of the attacker's ground speed and the target's position. The hawk's simulated ground speed was always matched to the measured GPS ground speed.

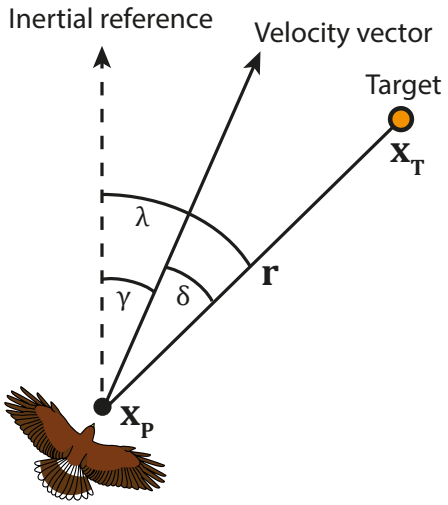


Figure 3.2: Definition sketch showing inertially derived angles of line-of-sight (LoS) bearing λ defined by the LoS vector $\boldsymbol{r}$ between the attacker and target positions $(\boldsymbol{x}_P, \boldsymbol{x}_T)$ and track angle γ which is the inertially referenced velocity vector bearing. Also shown is the egocentrically derived deviation angle δ defined as the angle between the LoS and velocity vectors.

3.3.2 Harris's Hawk trajectories are best modelled by the mixed guidance law

Guidance parameters (N, K, τ) were fitted to all 54 flights using an exhaustive search between a coarse range of gains $N = [0.2 : 0.2 : 6]$ and $K = [0.2 : 0.2 : 6]\, s^{-1}$ and $\tau = [0 : 0.02 : 0.2]\, s$, which were then refined using smaller intervals. The unique combination of N, K and τ that minimised the median root mean squared distance error (ε) between simulated and GPS measured trajectories over all flights was identified. Fig. 3.4 presents the fitted surface plots and global minimum error across all flights for each guidance law. This method gives a better representation of the observed flight behaviour compared to fitting individually and eliminates the risk of overfitting to the data.

Starting with PN and PP, where two parameters are fitted per flight, the best-fitting parameters of $N = 1.25$ and $\tau = 0.01\, s$ resulted in a median prediction error of $\bar{\varepsilon} = 2.86\, m$ for PN (Bootstrapped 95% CI: $\bar{\varepsilon} = 2.23, 3.69\, m$, $N = 0.85, 1.85$, $\tau = 0.0003, 0.03\, s$). For PP, $\bar{\varepsilon} = 2.28\, m$ resulted from optimal parameters of $K = 6\, s^{-1}$ and $\tau = 0\, s$ (Bootstrapped 95% CI: $\bar{\varepsilon} = 1.83, 2.68\, m$, $K = 6, 6\, s^{-1}$,

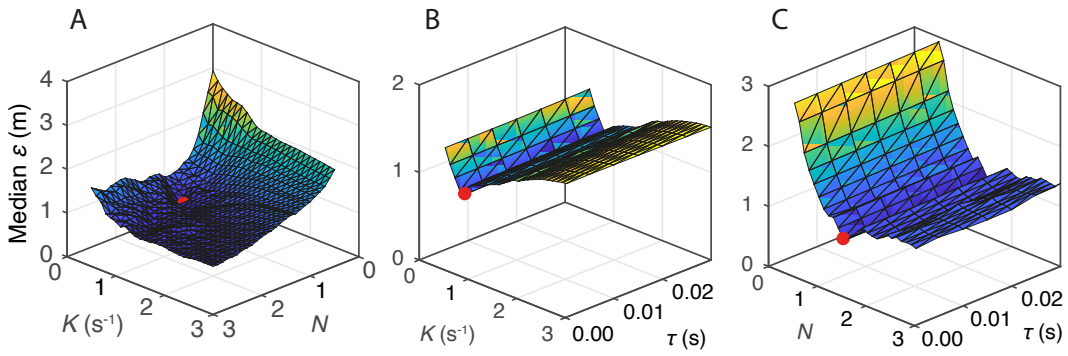


Figure 3.3: Mixed guidance law surface plots. Shows how median root mean square distance error (ε) varies as a function of each pair of guidance parameters N, K, τ, whilst holding the third constant over all 54 flights for the mixed PN+PP guidance law. Surface colour represents height and the red dot shows the optimal value.

$\tau = 0.0003, 0.08\,s$); the limits of the range of values (K and τ) tested. The optimal parameters fitted under the mixed guidance law were then identified to be $N = 1.5$,$K = 0.9\,s^{-1}$ and $\tau = 0\,s$ resulting in a median prediction error of $\bar{\varepsilon} = 0.94\,m$ (Bootstrapped 95% CI: $\bar{\varepsilon} = 0.73, 1.37\,m$, $N = 1.0, 1.6$, $K = 0.5, 1.0\,s^{-1}$, $\tau = 0.0003, 0.02\,s$). The lowest median error across all flights was found using the mixed PN+PP model with a 95% confidence interval that does not overlap with the results from the PP or PN guidance laws. These results show that the mixed guidance law fits best to the data, whilst neither PN or PP alone do not model the data well. The reduction in error when trajectories are simulated using PN+PP is statistically significant at the 5% level when compared against PN (Sign test: $p = 3.89E-10$) and PP (Sign test: $p = 3.89E-10$). The same result can also be seen in the distribution of relative error in Fig. 3.5, where the mixed guidance law gives the lowest IQR and median relative error, and in the simulated trajectories seen in Fig. 3.3. This figure presents three flights that represent the first, second and third quartile (Q1, Q2, Q3) of relative error for each guidance law. Relative error is calculated as the root mean squared error between the measured and simulated trajectories divided by the flight length for each flight. This is used since longer flights have a tendency to fit worse than shorter flights because the

model has error that accumulates over time. Shorter flights have less time for divergence to occur and so tend to more closely fit to the data.

The simulated trajectories visibly fit better to the dataset when compared those simulated using the other guidance models (Fig. 3.3); however, it can be seen that there are a significant number of flights where the optimal PN+PP simulation deviates from the measured trajectory or intercepts sooner than was measured. Most noticeably there is sometimes a point of divergence of the simulation from the measured trajectory. When this occurs, it typically does not recover, preventing a later convergence. We hypothesise that this may be a result of an internal or external perturbation on the bird affecting the fit, which we are not currently modelling. The relationship between average wind velocity and relative error was found to be uncorrelated (Wilcoxon test: $p = 0.237$, $z = -1.1825$). We conducted a sensitivity analysis of the optimal guidance parameters by incremental removal of the worst fitting flights from the sample set in order (see Fig. 3.6). This is standard outlier removal, enabling outlying flights, which may be the consequence of multiple factors, such as poor bird motivation, to be excluded prior to global fitting. In this way, the sampled data will more closely reflect pursuit flights and thus any model derived from the data may be expected to more accurately describe the true guidance parameters (N, K). Once each flight was removed, the trajectories were simulated using the new optimal parameters to obtain a new error distribution to use for the next flight removal. The parameters N, K and τ are relatively stable between 1 and 7 flights removed with N consistently higher than K. After 7 flights removed, the values of N and K change to a higher level whilst generally retaining the same hierarchy. As the number of flights removed increases, the reduction in median error towards zero indicates overfitting.

The worst fitting flights are subject to the most disturbance from following the trajectory simulated from the guidance law alone. It is clear that there are other effects influencing the flight trajectory that the guidance law cannot model alone. It is hypothesised that there are several effects that might influence each flight such as: wind gusts and turbulence, bird motivation and other experimental noise?

By removing the worst fitting flights, the most significant disturbance effects are removed from the dataset, allowing a reevaluation of the fitted guidance constants to assess whether the data is overfitted or not - or the effects of these worst fitting flights on the fitted guidance constants.

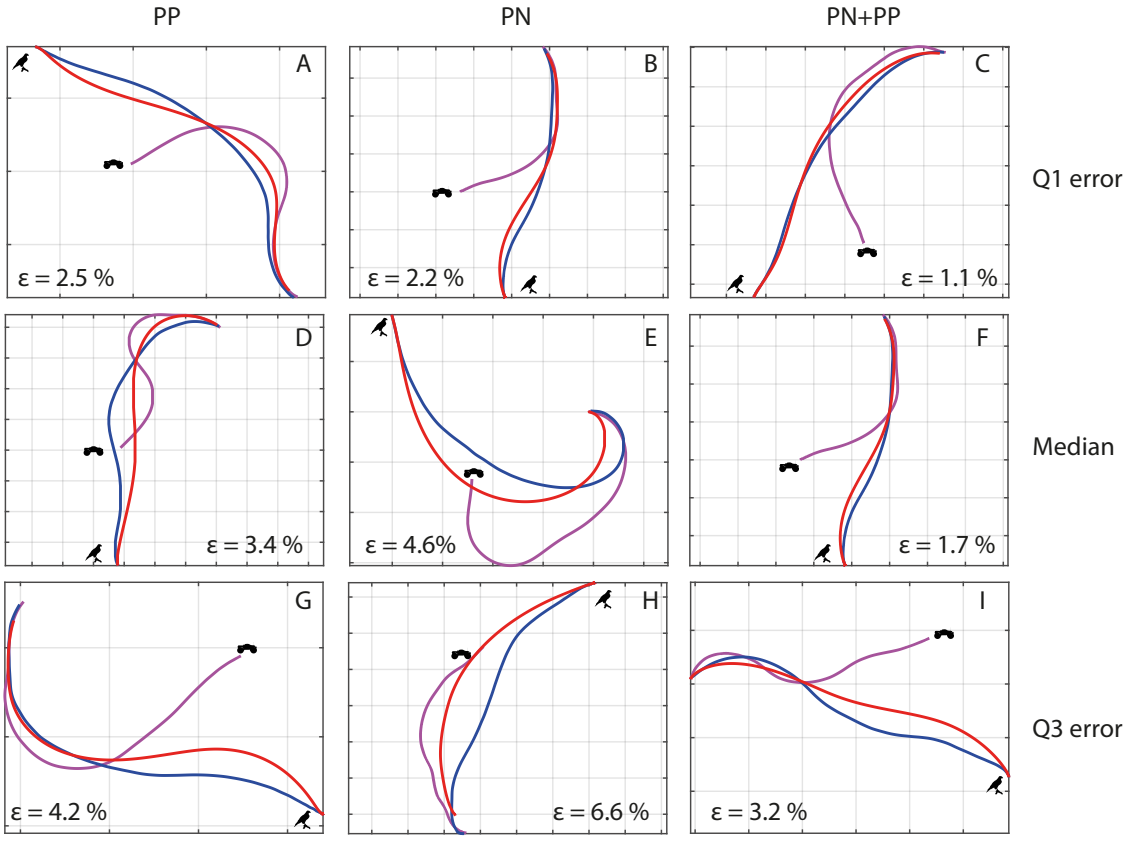


Figure 3.4: Comparison between measured and simulated intercept trajectories. Displaying best fitting simulated trajectories (red), measured attack trajectories (blue) and the measured target tracks (purple) over three flights using Q1, Q2 and Q3 error with the three guidance laws: PN+PP, PN and PP. Relative error (ε) (root mean square distance error/flight length) displayed on each panel. Grid spacing 10m. Bird and car start locations are marked.

We then checked for obvious explanations of the poor fit including the impact of takeoff, wind and sudden target accelerations. Firstly we explored the possibility of the highly dynamic takeoff phase affecting the fit in the region where the bird is not locked onto the target and guidance hasn't begun. Using IMU data, the takeoff phase was taken as the first 1.5 s of flight, which was removed from each flight before performing global guidance parameter optimisation and relative error between trajectories was assessed. This was compared to the fit results of removing

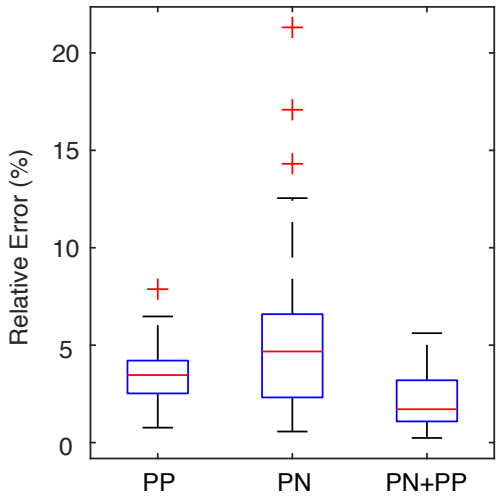


Figure 3.5: Comparison of guidance law fit performance. Box plot showing relative error distribution over all 54 flights between measured and simulated flight trajectories for each guidance law using the guidance parameters found from global optimisation. The centre line of each box denotes the median for all flights. The upper and lower bounds of the box denote the 3rd and 1st quartiles. Crosses indicate outliers falling >1.5 times the interquartile range beyond the 1st or third quartile.

the last 1.5 seconds of flight. There was no statistical evidence of fit improvement when removing the takeoff phase compared to using the full flight (Wilcoxon test: $p = 0.4564$, $z = -0.7448$). We investigated at the points of divergence in the flight whether the bird suddenly accelerated; however, after reviewing several flights where this occurred, rapid changes in acceleration were not distinctly apparent or captured. We hypothesised that the bird might respond to target acceleration, which is an internal perturbation not factored into the PN+PP model. Augmented PN (APN) is an alternate form of PN used in missile literature which uses an additional term that allows response to target acceleration perpendicular to the line-of sight-vector [49]. This was incorporated into the mixed guidance law model and parameter optimisation over all flights was run, but due to the noise present in the acceleration signal this did not make an improvement to fit performance (see supplementary text in Appendix B for more detail).

Overall, the results indicate that the mixed guidance law is the optimal model for the observed attack behaviour from this experiment and we now investigate

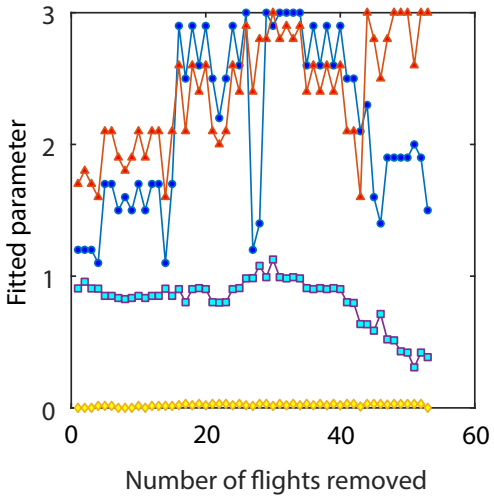


Figure 3.6: Sensitivity analysis of PN+PP optimal guidance parameters. Showing the effect of removing flights from the sample set with the highest relative error between measured and simulated trajectories on the optimal guidance parameters of N (red triangle), K (s^{-1}, blue circle), τ (s, yellow diamond) and the median mean root square distance $\tilde{\varepsilon}$ (m, blue square).

whether the mixed guidance law as used here is optimal for modelling guidance in the presence of wind.

3.3.3 Generating a lift-based mixed guidance model for gliding flight in wind

In the current form of the guidance equations, ground velocity- defined as the sum of air and wind velocities ($\boldsymbol{v}_g = \boldsymbol{v}_a + \boldsymbol{v}_w$) - is used to estimate the sensory input vectors δ, ω and it also defines the direction of the commanded centripetal acceleration via the definition of pure PN in the mixed guidance law. Given however, that the presence of wind affects a bird's flight trajectory in the form of wind drift for which it must compensate if within the limits of their control system, it seems prudent to account for this and generate the best physical model to suit these conditions. Presence of wind may be a contributing external perturbation affecting the simulated trajectory error for some flights.

When considering the PN part of the guidance law, centripetal acceleration can be commanded perpendicular to the ground velocity vector as in pure pro-

portional navigation (PPN) (the definition of PN used in the above simulations), or alternatively commanded perpendicular to the air velocity vector. Previous modelling assumes that the bird commands its turning force perpendicular to its ground velocity. However, commanding turning perpendicular to air velocity is equivalent to the assumption that bird's control force is lift-based. Since birds use lift to control the orientation of their body and implement turning primarily though banking, this model is best suited for gliding flight, where lift is perpendicular to air velocity. Through this, we generated a new mixed guidance model based on proportional navigation implemented with air velocity, which we denote as banked turn PN (BPN). The structure of the model implementation is seen in Fig. 3.7.

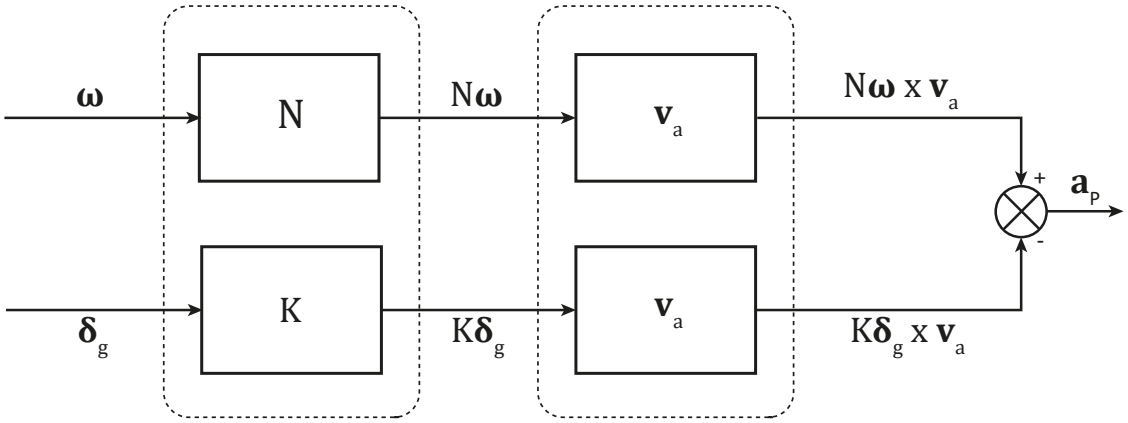


Figure 3.7: Wind modelling implementation flow diagram. Showing a control flow of the $BPN+PP_g$ model implementation using the sensory inputs of line-of-sight vector (ω) and deviation angle defined by ground velocity (δ_g) and air velocity ($\boldsymbol{v}_a$) as the acceleration direction modifier as defined by BPN.

We start with the full ground velocity-based implementation of PN+PP and rewrite this in the form:

$$\boldsymbol{a}_{PPN+PP_g}(t) = N\boldsymbol{\omega}(t-\tau) \times \boldsymbol{v}_g(t) - K\boldsymbol{\delta}_g(t-\tau) \times \boldsymbol{v}_g(t) \tag{3.12}$$

Where subscript $PPN + PP_g$ indicates ground velocity-based pure PN and PP components. The mixed guidance model implemented with BPN can be written as:

$$\boldsymbol{a}_{BPN+PP_g}(t) = N\boldsymbol{\omega}(t-\tau) \times \boldsymbol{v}_a(t) - K\boldsymbol{\delta}_g(t-\tau) \times \boldsymbol{v}_a(t) \tag{3.13}$$

As this equation shows, the definition of PPN or BPN dictates the direction of acceleration for both PN and PP parts of the mixed model.

The optimal guidance parameters were then identified for this new mixed guidance model, which minimised the median root mean square distance error between simulated and measured trajectories for a sample size of 50 flights; reduced from 54 due to the lack of wind data available for the four omitted flights. Optimal parameters of $N = 1.90$, $K = 1.35$ and $\tau = 0.02\,s$ were identified for the $BPN+PP_g$ model and resulted in a median prediction error of$\bar{\varepsilon} = 0.82\,m$ (Bootstrapped 95% CI: $\bar{\varepsilon} = 0.69,\ 1.17\,m$, $N = 1.65,\ 3.0$,$K = 1.2,\ 3.0\,s^{-1}$, $\tau = 0.00,\ 0.02\,s$). Marginal improvement in IQR and median (see Fig. 3.8) suggests that $BPN + PP_g$ is a better model in wind; however, there is no statistical evidence of an improvement (Wilcoxon signed-rank test: $p = 0.173$, $z = 1.36$).

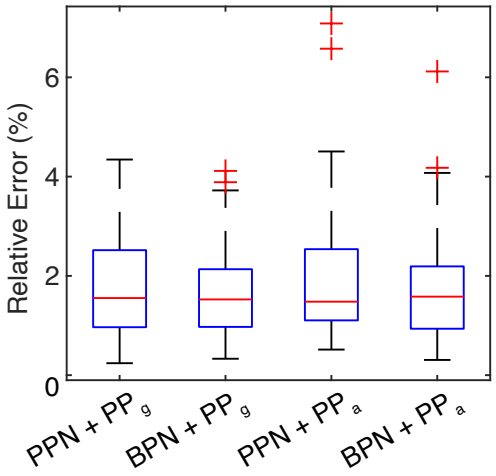


Figure 3.8: Comparison of wind modelling guidance law fit performance. Box plot showing relative error distribution over all 50 flights between measured and simulated flight trajectories for each guidance law using the guidance parameters found from global optimisation. $PPN + PP_g$ is the ground velocity defined law, $BPN + PP_g$ uses air velocity in the definition of the PN part of the model, $PPN + PP_a$ uses air velocity in the PP definition of deviation angle and $BPN + PP_a$ uses air velocity in the definition of both PN and PP parts of the mixed guidance law. The centre line of each box denotes the median for all flights. The upper and lower bounds of the box denote the 3rd and 1st quartiles. Crosses indicate outliers falling > 1.5 times the interquartile range beyond the 1st or third quartile.

3.3.4 Incorporating air velocity to definition of deviation angle

The line-of-sight rate is always estimated using ground velocity, since it is an inertial measurement between the target and pursuer positions. The deviation angle; however, can be estimated as the angle between either $\boldsymbol{v}_g$ or $\boldsymbol{v}_a$ and the target LoS vector. This leads to two options when configuring the PP part of the mixed guidance law, allowing investigation of whether deviation angle derived from ground or air velocity is optimal in the presence of wind. This allows two further mixed guidance models to be tested incorporating PP with deviation angle defined by air velocity in combination with PPN or BPN. These are written as:

$$\boldsymbol{a}_{PPN+PP_a}(t) = N\boldsymbol{\omega}(t-\tau) \times \boldsymbol{v}_g(t) - K\boldsymbol{\delta}_a(t-\tau) \times \boldsymbol{v}_g(t) \tag{3.14}$$

$$\boldsymbol{a}_{BPN+PP_a}(t) = N\boldsymbol{\omega}(t-\tau) \times \boldsymbol{v}_a(t) - K\boldsymbol{\delta}_a(t-\tau) \times \boldsymbol{v}_a(t) \tag{3.15}$$

The best fitting guidance parameters across the 50 flights were then found for these two models. The median prediction error was $\bar{\varepsilon} = 0.97\,m$ for $PPN + PP_a$ with $N = 1.80$, $K = 0.65\,s^{-1}$ and $\tau = 0.01\,s$ (Bootstrapped 95% CI: $\bar{\varepsilon} = 0.70,\ 1.21\,m$, $N = 1.6,\ 3.0$, $K = 0.5,\ 2.4\,s^{-1}$,$\tau = 0.00,\ 0.02\,s$). For $BPN + PP_a$, where both guidance parts are dependent on air velocity, median error was slightly lower than $PPN + PP_a$ at $\bar{\varepsilon} = 0.87\,m$ with with $N = 1.70$, $K = 0.55\,s^{-1}$ and $\tau = 0.01\,s$ (Bootstrapped 95% CI: $\bar{\varepsilon} = 0.70,\ 1.17\,m$, $N = 1.6,\ 5.0$, $K = 0.6,\ 5.0\,s^{-1}$, $\tau = 0.00,\ 0.02\,s$). See Fig. 3.8 for a comparison of the two new models to the ground velocity PN+PP model. Neither model provided a statistical improvement to the fit (Wilcoxon test: $p = 0.836$, $z = -0.208$ and $p = 0.066$, $z = 1.839$).

3.4 Discussion

This work presents the first time a long-range outdoor target pursuit experiment has been performed with highly accurate and precise position data using PPK GNSS biologgers. It is also the first time that the effect of external perturbations

on guidance in the form of wind disturbance has been quantified and analysed. There are several other improvements in the data captured in this experiment in comparison to our previous studies. Here we used a velocity validation using independent sensors (GNSS and IMU) to remove flights that did not meet a threshold discrepancy, whilst previously, we have had to use the GPS Doppler speed measure to validate GPS position [10]; two dependent measures. Further to this, we have no accuracy measure from trajectories produced using 3D photogrammetry [11] due to distorted camera calibrations.

The first key finding of this work is that for differing target behaviour, individuals and intercept distance, the mixed guidance law best models the guidance behaviour of Harris's hawks. We have previously found the PN+PP law to best model Harris's hawk flight in close pursuit of erratic targets with globally optimized parameters of $N = 0.7$, $K = 1.2\,s^{-1}$, $\tau = 0.09\,s$ [11], whereas it does so in this study under long range flight to a smoothly manoeuvring target with different guidance tuning of $N = 1.5$, $K = 0.9\,s^{-1}$, $\tau = 0.0003\,s$. The difference in target behaviour is clear; whilst here the target executes large radius turns with low jerk, the target in [11] displays abrupt turning at inflection points of the trajectory with high jerk motion. The key questions are: how does changing values of N, K and τ affect the simulated trajectory and is there is any significance in the different parameter tuning for each target type? We first look at the mechanisation of the mixed guidance law via the bird's sensory outputs.

3.4.1 Sensory Inputs

The mixed guidance law uses inputs of deviation angle and line-of-sight rate. The deviation angle between the bird's velocity vector and the line-of-sight to target vector can be estimated egocentrically between the axes of the bird's body and head via neck proprioception if the head is assumed to be level and tracking the target (and assuming negligible eye movement). Relative angle between head angle and optic flow direction could also be used. The wings of the bird are always aligned with the flow velocity, otherwise, there would be an additional control force required

and additional drag penalty in flight. The velocity direction is therefore aligned with the body axis under the assumption that displacement between the body and wings is minimal. The line-of-sight rate is measured in the inertial frame of reference and could be extracted in one of two ways dependent on the visual tracking strategy used by the bird. If the bird uses its head to continuously track the target, LoS rate could be approximated using head yaw rate by integration of the head acceleration from the vestibular system. Alternatively, if the bird uses a fixed head bearing and saccadic mode tracking of the target, the drift of the target across the bird's retina could be used. Alternatively, a combination of both vestibular and visual systems could be used as in an inertially stabilized missile seeker [17].

3.4.2 Comparison in guidance law behaviour

In guidance fitting over all flights, the mixed guidance law resulted in the lowest minimum median error and a statistically significant improvement over fitting with either PP or PN. Optimisation of the mixed guidance law involves balancing the linear contributions of PN and PP. To understand the physical implications of the different parameter tuning, it is important to first consider the effect different values of N and K have on the trajectories produced by the PN and PP components of the mixed guidance law. Proportional pursuit has the characteristic of driving the pursuer into a tail-chase trajectory through driving the deviation angle to zero. In PP, gains of $K > 1$ are required for intercept. Although PP simulated the intercept trajectories with a lower median error when compared to PN, the CI ranges overlap and so it cannot be concluded that it models the data better overall. The best fitting parameters found when fitting PP were the maximum tested gain of $K = 6\,s^{-1}$ and the minimum tested delay of $\tau = 0.0003\,s$. Given a larger range for K, this would be driven to the highest gain possible. Maximal turning gain (K) and minimal delay (τ) drive the pursuer into tail-chase behaviour more rapidly and causes the end point of the simulated trajectory to align more closely to the interception point of the measured data; thus, reducing the overall error, as the

simulations run using the same flight distance as was measured. High gains such as these can lead to large deviations in position due to measurement error.

PN has the characteristic of generating an intercept trajectory rather than a tail-chase (except when $N = 1$ and $\delta(0)$ is small). It does this by driving the line-of-sight rate to zero, which results in a constant bearing (λ) approach to target interception [17]. This is best described as parallel navigation, where the line-of-sight angle is kept constant throughout the trajectory and is a key requirement for target intercept. Proportional navigation is proportional control that incorporates an element of prediction due to the use of the derivative term ($\dot{\lambda}$). Higher values of the navigation constant increase the turning rate commanded by the bird, which will lead the bird to intercept the target more rapidly until overshoot, which is caused by too high a gain amplifying measurement noise. PN is a more efficient strategy than PP in terms of time to target capture; however, it is not suited to all pursuit behaviours and operating environments.

To investigate the effect of different optimal guidance tuning in simulation, we tested the two sets of optimal parameters; one identified in this study to the smooth target and the other identified to the erratic target [11] and simulated the bird's intercept to two datasets of measured target trajectories. Fig. 3.10 displays this for illustration only over two separate flights, whilst the relative error distributions over all flights in each dataset are presented in Fig. 3.9. In comparing our mixed guidance parameters to those in Brighton and Taylor [11], we find that there is a considerable increase in the navigation constant from $N = 0.7$ to $N = 1.5$ and a slight decrease in PP gain from $K = 1.2\,s^{-1}$ to $K = 0.9\,s^{-1}$. The effect of the increase in the N to K ratio when simulating on smooth target trajectories is to better model the turning characteristics and intercept the target in the same distance the measured bird flew. When simulating using the parameters identified on the erratic target, the simulated bird does not intercept (see Fig. 3.9 A, B). On the contrary, when simulating the optimal smooth target parameters on erratic target behaviour, the turning is not modelled well and the target is not intercepted with a relative error of 0.97% vs 0.35% for the optimally tuned parameters (see Fig. 3.9 C, D). When

looking at the results over all flights, the best performance is achieved when using guidance parameters fitted to the target being tested (see Fig. 3.10). For the smooth target, this resulted in an improvement in the median relative error from 3.1% to 1.7% (minimum median root mean squared error from $\bar{\varepsilon} = 2.22\,m$ to $\bar{\varepsilon} = 0.94\,m$) and 1.4% to 0.84% for the erratic target dataset. The improvements when using the parameters tuned to the target behaviour was significant in both cases at the 95% level (Wilcoxon test: $p_{erratic} = 1E-5$, $z_{erratic} = -3.88$, $p_{smooth} = 7E-9$, $z_{smooth} = 5.79$). Different parameter tuning for alternate target types might indicate that overfitting has occurred; however, the sensitivity analysis conducted (Fig. 3.6) indicates that the fitted parameters to the smooth target are robust to removal of around 7 flights. The improvement in modelling error when testing the correct tuned parameters for the target type is significant enough to also suggest otherwise.

The significant increase in N tuning is unsurprising given the smoothly manoeuvring target used in this experiment follows a predictable path. A greater contribution of PN guidance indicated by a higher N gain to K gain ratio suggests that there is a lower tail-chase demand on the bird typically associated with pursuing an unpredictable target, which enables it to implement the intercept type trajectory obtained with PN guidance to shorten the time to intercept. The τ value in guidance simulations using PN+PP, PN or PP provides an indication of the optimal sensorimotor delay fitted to the measured data. Whilst visual response time in other species varies widely from 25ms in the fruit fly [105] to $< 5ms$ in *Condylostylus* flies (*Diptera: Dolichopodidae*) [106], in birds, Stitt et al [107] found the visuomotor delay in pigeons to be a minimum of around 30ms and Pomeroy and Heppner [108] found a delay of around 70ms in starlings to a light flash stimulus. Given these figures in avian species, we assume that we might expect sensorimotor delay values from simulation between 30-70ms. The optimal delay of 90ms fitted in Harris's hawks to erratic targets is above this expected range. However, in that experiment, the target exhibits large accelerations with jerk (if the bird uses target acceleration as a guidance input, a delay is required). We optimally fitted a very low delay of 0.3ms (0.0003s) across all flights which was robust in the sensitivity analysis

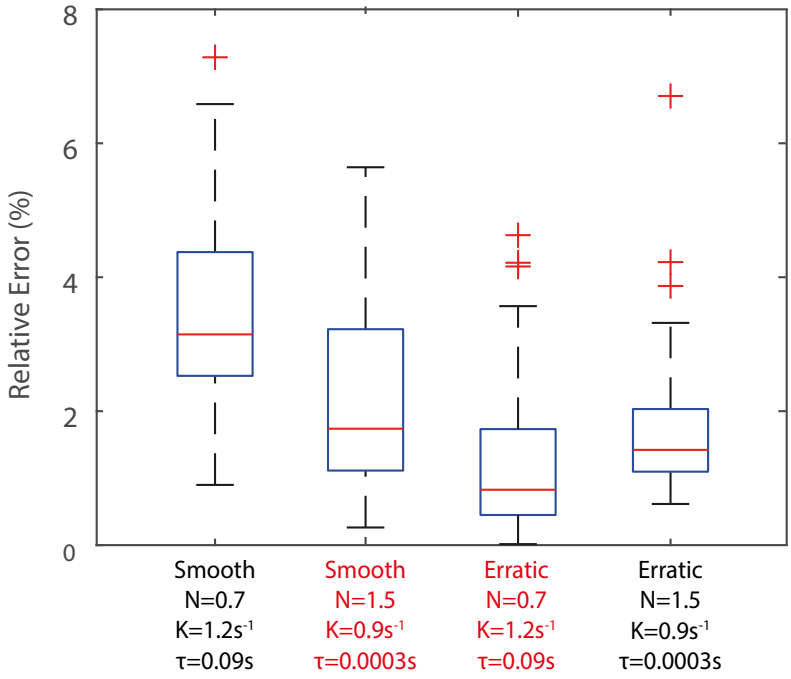


Figure 3.9: Comparison of simulated trajectories using optimal guidance parameters tuned with smooth and erratic targets. Showing results of simulation with two trajectories from different target behaviours: A, B show the simulated interception trajectory to the smooth target using A) optimal guidance parameters tuned to smooth target and B) optimal guidance parameters tuned to erratic target. C, D show the simulated interception trajectory to the erratic target using C) optimal guidance parameters tuned to smooth target and D) optimal guidance parameters tuned to erratic target. Also shown is the measured trajectory flow by the hawk (blue). The optimal guidance parameters of navigation constant, N, PP gain, K and sensorimotor delay,τ are given on each panel in addition to the relative error (ε) (root mean square distance error/flight length). Grid spacing 10m.

to a reduction in several flights in the sample. The temporal synchronization between the GNSS receiver pair was accurate at a maximum of around 50 μs in addition to a maximum offset of 0.12 μs due to the accuracy of the receiver time pulse [99]. The zero-delay fitted here may not be representative of the visuomotor delay, which includes a delay in the visual system and in muscle actuation but may represent a delay in the guidance. A guidance delay of zero is plausible given that we hypothesise the hawks are able to effectively predict the future position and velocity of the target using visual filtering, which is mathematically trivial with a target that follows smooth, large radius turns. This target type also exhibits smoother acceleration with low jerk, and so zero-delay indicates that the bird

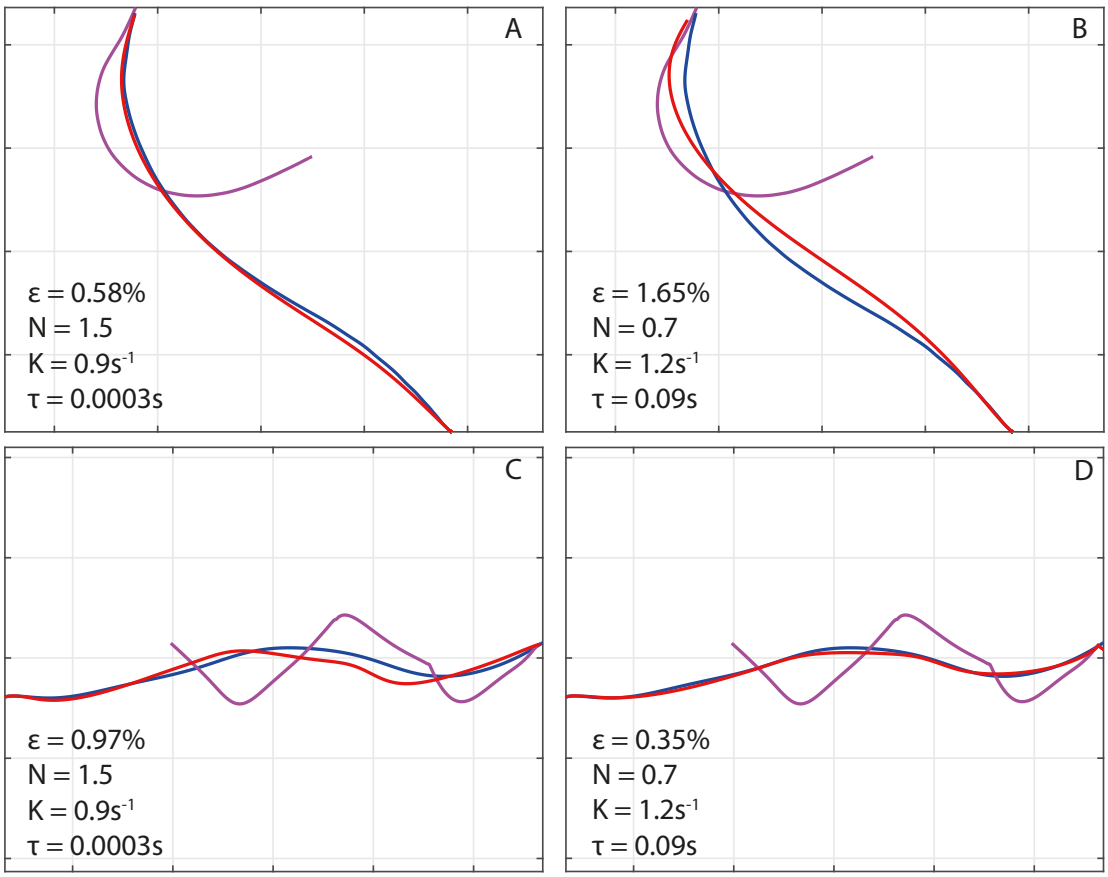


Figure 3.10: Comparison of simulation error using optimal guidance parameters tuned with smooth and erratic targets. Showing relative error from simulating trajectories to smooth and erratic target trajectories using two sets of globally fitted optimal guidance parameters (N, K, τ) to: 1) smooth target and 2) erratic target. Optimal parameters fitted to the target trajectories from which they were identified are shown in red text.

doesn't use target acceleration as guidance input.

The hawks may be tuning their guidance to suit the target behaviour, but there may be other factors that cause these differences. The instrumentation used to measure bird position in each experiment differs, with the 2019 study [11] using 3D photogrammetry with high-speed cameras whereas high accuracy GNSS is used here. We were also unable to directly compare the guidance output of the same bird. Of the five birds used in this study, only one was used in the previous study. Since there are not enough flight samples across each bird to investigate individual tuning, a reliable comparison could not be made as it is likely that guidance tuning between individuals differs with morphology and experience. Assumptions in the model contribute to uncertainty in the results, for example we assume that the values of

N and K are constant throughout the flight, but may not be the case. Overall, the presented modelling framework allows the measured flight trajectory dynamics to be described and compared with two or three parameters (PN/PP or PN+PP) with the knowledge that this is not a complete model of the observed behaviour.

3.4.3 The mixed guidance law is robust to wind

When flying in the presence of wind, a bird must implement additional control input to counter wind drift when performing a goal-oriented behaviour such as prey pursuit. Turning control is implemented via banking to reorient the lift vector laterally, so in wind it makes sense to command turning relative to air velocity rather than ground velocity. Here, we tested three alternative formulations of the mixed guidance law; using BPN, where the air velocity vector was used to direct the acceleration vector and combinations using PP_a, where air velocity was used as the reference for the deviation angle sensory input. For the birds to obtain this sensory information, we assume that in the presence of wind, the bird aligns its wings to the air velocity vector, making control perpendicular to this direction intuitive. From this reference, the deviation angle is obtained in the same manner as previously described, by measuring head angle or retinal position to the target. Results from this testing (see Fig 3.8) indicate that the mixed guidance law ($PPN + PP_g$) is robust to wind, as the improvements in error by any of the three alternatives across all flights are minimal. $BPN + PP_g$ appears to be the best alternative wind model, providing a slightly lower median error and lower IQR, yet any improvements are statistically insignificant. This formulation makes the most sense via first principles, by using the air velocity direction to control the force and using the deviation angle definition relative to ground velocity extracted via optic flow. However, observations of IMU data indicate that there is little gliding done by all birds throughout each flight and that from takeoff to intercept flapping is the dominant mechanism. This may explain the limited improvements by the model, since in a flapping wing model, the bird has the ability to perform thrust vectoring to guide flight relative to ground velocity rather than air velocity as is performed when gliding in a fixed

wing model. Further to this, averaging of wind velocity from a point source rather than an accurate wind field measurement over the entire flight area means that we do not accurately know the wind field at the bird's location and therefore cannot model sudden perturbations caused by wind gusts.

Guidance during flapping suggests that gaze stabilization is highly effective, which presents questions for how the birds use gaze strategy to fixate and track their targets. This is an opportunity to understand the method through which the sensory inputs (δ, $\dot{\lambda}$) are extracted through gaze which will be explored in the next chapter.

4

Gaze Strategy in Harris's Hawks

Abstract

Aerial pursuit in raptors has been characterised using simple behavioural algorithms known as guidance laws which input target information available to the bird using the visual and vestibular systems. The attack trajectories of Harris's hawks (*Parabuteo unicinctus*) have been well modelled by a mixed guidance law, which combines the rate of change in the line-of-sight between predator and prey and the deviation angle between the predator's velocity vector and line-of-sight bearing to target to generate a steering command. It is not understood what gaze strategy birds use to measure this target information during flight. Here we take inertial measurements of the hawk's head and GNSS position data of the body during n=42 flights from N=5 birds to assess their gaze strategy. We find that a saccadic tracking strategy is used which combines a saccade and fixate technique with high frequency catch-up corrections; keeping the target within the binocular overlap of the visual field. We use this to suggest how gaze movements allow target guidance to be mechanised and hypothesise about the physiological pathways that control guidance.

4.1 Introduction

An aerial predator relies on its ability to direct its attack trajectory to intercept its prey. Behavioural algorithms known as guidance laws have been well studied in their ability to model the pursuit flights of Harris's hawks (*Parabuteo unicinctus*), peregrine falcons (*Falco peregrinus*) and gyrfalcons (*Falco unicinctus*) [10–12]. Guidance laws; typically used in homing missile guidance, model flight based on generating steering commands dependent on inputs derived from a target's position relative to the pursuer. A mixed guidance law (PN+PP) has been found to best model attack trajectories in Harris's hawks [11]. The PN+PP law combines proportional navigation (PN) and proportional pursuit (PP). A PN algorithm commands turning proportionally to the angular rate of the line-of-sight (LoS) vector (λ), which is the vector between the inertial positions of attacker and target in the form $\dot{\gamma} = N\dot{\lambda}$, where $\dot{\gamma}$ is the turn rate, N is the navigation constant (a constant gain) and $\dot{\lambda}$ is the LoS rate. A PP algorithm commands turning proportionally to the deviation angle (δ), which is the angle between the pursuer's velocity vector and its line-of-sight (LoS) to target vector in the form $\dot{\gamma} = -K\delta$, where K is a constant gain. Brighton and Taylor's results [11] suggest that the hawks are able to estimate the LoS rate and deviation angle to facilitate execution of PN+PP and likewise previous results in peregrines and gyrfalcons [10, 12] suggest that they are able to estimate LoS rate to execute PN. Whether these raptors possess the sensory ability to directly measure these quantities or whether they use alternate sensory information to approximate these inputs to guide their flight has been inadequately explored. To estimate LoS rate, either the retinal drift rate of the target or the yaw rate of the head could be used depending on whether the head is stabilised on the background or constantly redirected towards the target. An intermediate combination of both is also possible. For deviation angle, measurement of the angle between the target location and centre of expansion of the translational optic flow field on the retina would enable acquisition of this information for input into the guidance loop.

During flight, a hawk has available the visual, vestibular and proprioceptive systems to estimate environmental stimuli. When hunting, the visual system is the primary input used to facilitate target detection, tracking and intercept. To obtain target information via visual tracking, the bird requires a gaze strategy to reorient its field of view during flight. Common in insects [45] and birds [43, 44, 109, 110] is a strategy of gaze stabilization combined with saccadic gaze shifts. Walls [28] suggested that a saccade and fixate strategy evolved to stabilize the environment during locomotion to eliminate motion blur [111] where gaze shifts are rapid so to maximise the period of head stabilisation to survey the visual environment. Hateren and Schilstra found the saccade and fixate strategy in blowflies (*Calliphora vicina*) [45] to separate flight into periods where either rotational or translational optic flow are dominant, which is beneficial as information about the visual environment can be readily obtained when there is only translational optic flow. Head saccades are a characteristic of visual behaviour in birds, with their light heads and flexible necks enabling rapid movements akin to eye saccades in primates [111]. Kress et al [109] found that lovebirds utilise a gaze strategy that optimises frontal feature stabilisation facilitating optic flow-based flight control in between rapid (up to $2700\,^\circ\,\mathrm{s}^{-1}$) head saccades. Ros and Biewener [44] suggested that visual and proprioceptive cues are used as steering inputs for turning flight in birds. They found that pigeons (*Columba livia*) direct head saccades into the turn rather than the flight trajectory and may use head offset to reorient their body after turning. Experiments in red-tailed hawks (*Buteo jamaicensis*), Cooper's hawks (*Accipiter cooperii*) and American kestrels (*Falco sparverius*) show eye movements in the range of $2^\circ - 8^\circ$ in head fixed individuals [19]; a situation where the birds are likely to compensate for the lack of a moving head leading to exaggerated movements [112]. Ros and Biewener [44] also found limited eye movements in pigeons. It is therefore reasonably assumed that eye movements have an insignificant contribution to angular gaze shifts; however, the vestibulo-ocular reflex (VOR) of the eye does appear to function to maintain constant gaze direction as the head turns [111]. Specific to the task of target tracking, humans and other primates have the ability to perform smooth

pursuit; where objects are continuously rather than saccadically tracked with eye movements [1]. It has not yet been observed whether birds possess the ability to perform this type of visual tracking.

The strategy by which a hawk foveates its target determines what information it receives and how it can implement guidance. In the eye of predatory birds exist two regions of high visual acuity called foveae: the forward-facing temporal fovea and the laterally directed central fovea [24]. In Harris's hawks there is a binocular overlap of 47° between the two temporal foveae, and in each eye, the central fovea is approximately located at an angle of 57.5° from the mid-sagittal plane [22]. Tucker [113] proposed that peregrines may be implementing a geometric guidance rule dependent on keeping the target fixed on the central fovea for maximum visual acuity. Although Brighton et al [10] found the hypothesised rule describing the attack trajectories of peregrines to be inconsistent with their results, the possibility of raptors using a gaze strategy during pursuit that uses a fixed single fovea or one that switches between temporal and central foveae to optimise target acquisition is yet to be explored.

In homing missiles, there exist two sensor arrangements used to extract target information for guidance known as the strapdown seeker and the space-stabilised seeker. Strapdown seekers are fixed to the missile body in all axes, analogous to a bird that does not move its head. Space-stabilised seekers are mounted in a 2-axis pitch and roll gimbal arrangement (with roll stabilisation from a missile control system) that allows sensor movement for increased field-of-regard in target tracking and mechanical isolation from body motion. This mechanism performs analogously to the function of the bird's head-neck motor system in head stabilisation and shifting gaze direction. In a typical missile implementing PN guidance, gimballed seekers extract LoS rate information via rate gyros to measure seeker angular rate, and a feedback control loop using one of a variety of methods that all rely on the seeker centreline continuously tracking the target [49].

Given knowledge of the saccade and fixate gaze strategy in birds, we hypothesise that during target tracking in pursuit flight the hawk may use this technique with

inertial head stabilisation in the intersaccade period. In this case, LoS rate may be estimated using the rate of target drift across the retina. This strategy would be characterised by rapid head saccades to prevent the target reaching the limits of the visual field and limit the time over which retinal drift information is unavailable due to motion blur. Alternatively, taking inspiration from gimballed seekers in homing missiles, the hawk may utilise a continuous tracking gaze strategy. As in missile systems, the angular rate of the bird's head could be used to measure the LoS rate via the vestibular system; where modelling has suggested the semicircular canals are able to directly measure angular displacement, rate and angular acceleration [114]. Finally, a combination of both of these may be implemented; allowing target LoS information to be obtained via angular head rate and retinal drift rate. We do not expect the birds to be using a fixed head strategy akin to a strapdown missile seeker since birds make head movements during flight.

To mechanise the mixed PN+PP guidance law, deviation angle must also be estimated. Deviation angle is an egocentric measurement local to the bird's coordinate system rather than the inertial coordinate system. With a rotationally stabilised head, δ could be measured as the angle between the retinal position of the target and the optic flow singularity, which represents the local velocity direction. This would be valid when using a saccade and fixate strategy with an inertially stabilised head, but with a continuous gaze strategy, the introduction of rotational and translational self-motion causes the singularity to longer represent the bird's velocity vector. When the head is not rotationally stabilised the velocity vector may be estimated using feather airflow sensors to align the head gaze direction with the flow direction in a still air environment (no wind). This would allow deviation angle relative to air velocity rather than ground velocity to be determined. In this work, we aim to understand how Harris's hawks mechanise pursuit guidance through the use of gaze strategy to orient their head and visual system.

We present flight trajectories and head gaze data from 42 Harris's hawk pursuit flights from n=5 birds chasing a food lure target fitted to a radio-controlled car using custom precision Global Positioning System and Inertial Measurement Unit

(GPS-IMU) loggers. The IMU was mounted to the head of the bird to record gaze data throughout the flight. Time domain analyses gave insights into gaze strategy and valid approximations (proxies) for LoS rate and deviation angle guidance inputs. Guidance simulations of PN, PP and PN+PP were then performed and the results of this using proxy and true values of the input parameters were compared. We conclude by providing a suggestion of the guidance and gaze feedback control loop that may be used in the bird to mechanise pursuit guidance.

4.2 Materials and Methods

4.2.1 Data Collection

We flew n=5 captive-bred Harris's hawks (*Parabuteo unicinctus*) at a smoothly manoeuvring target simulating a fast-moving ground prey item. The birds consisted of 4 males and 1 female, having mass that ranged between 0.62 kg - 0.84 kg during experimentation. A meat lure attached to a Savage XS (HPI Racing, Denmark) radio-controlled car was used as the pursuit target. Tests were conducted at the cricket pitch in Wytham, UK. For each flight, the target start direction was randomised from one of four perpendicular directions and the bird start direction was randomised from one of three directions relative to the target's start position (avoiding the scenario where the car exits towards the bird). The target start location was fixed over all flights and was concealed in a box such that the bird did not anticipate the exit direction.

Each bird flew 3 consecutive flights per day leading to a possible total of 15 flights per day across all individuals. The car was driven manually in an evasive trajectory with smooth turning. The evasive trajectory was not controlled statistically and was manually reactive to the observed behaviour of the bird in an attempt to force the bird to turn as much as possible. Turn rates were limited by the performance envelope of the car. The car's speed was modulated based on the performance of the bird; as such it was reduced if the bird's speed dropped to motivate it to continue pursuit. For the fittest individuals, the maximum speed was not sufficient

to outpace them. The bird start position was set at an offset of 30m from the target. Please see figure 4.1 in section 3.2 for the experimental setup and procedure.



Figure 4.1: Schematic of experimental setup and inset photograph from flight trials. This shows the car start position in the centre of the Wytham cricket field that was hidden inside a box with 4 potential exit directions labelled 1-4. The 4 random bird start positions are labelled as orange dots and also labelled 1-4 at a constant 30m from the box. The inset figure shows the falconer holding the bird before takeoff with the car box in view.

The hawks were fitted with a custom designed post processed kinematic (PPK) GNSS-IMU biologger, comprising a back-mounted ZED-F9P GNSS receiver (u-Blox, Switzerland) and external 9 degree of freedom BNO055 IMU (Bosch Sensortec, Germany) attached to the head of the bird using Velcro. An identical logger was placed on the car without the IMU. The biologger was attached to the bird with a falconry harness, which uses a plastic mounting plate held between the shoulders by

a pair of Teflon ribbons drawn once around the bird's body in a figure-of-eight. A local GNSS base station also using an identical GNSS receiver was placed at a fixed location on the cricket strip for GNSS post processing and to provide a fixed reference for calibration of the head IMU. These loggers recorded GNSS position data at 10Hz and IMU data at 50Hz. In addition to measuring angular velocity (gyro), linear acceleration (accelerometer) and magnetic field strength (magnetometer), the IMU outputted a fused orientation output relative to magnetic north in quaternions.

The GNSS receiver output both raw satellite data to process a PPK solution and also the internal satellite-based augmentation system (SBAS) solution; a message that notably includes longitude, latitude, height and Doppler speed. A PPK GNSS solution is a post processing method that enables high precision and centimetre-level accuracy to the ground truth and relatively between two receivers. This operates using a moving receiver (bird/car) and a static base station receiver concurrently to reduce satellite and receiver clock errors. For data recorded from bird-mounted loggers, an interpolated PPK technique was developed to recover centimetre accuracy from the internal receiver SBAS position solution over short timescales. This uses a linear correction that interpolates between the endpoint offset between PPK and SBAS positions in the stationary region either side of a flight to correct the position of the SBAS data.

4.2.2 Data Processing

For each flight, we obtained synchronised GNSS position data from the hawk and target. We extracted angular rate, acceleration, magnetic field strength and head orientation from the IMU fitted to the head of the hawk and synchronised this to the GNSS data. For more detail in extracting a PPK position solution, processing the SBAS position data, IMU head data and in quality control of flights see the supplementary methods in Appendix C.

4.2.3 Guidance Simulations

The guidance simulations processed in this work are based upon 2D planar motion in which the geometric and kinematic equations are written in the inertial reference frame. The simulation method used is the same as that developed by Brighton & Taylor, 2019 [11], from which the remainder of this section is drawn. The line-of-sight vector or range ($\boldsymbol{r}$) between the pursuer (P) and the target (T) defines the distance between the two objects and the line-of-sight direction directed from P to T. Using the measured position vector of the pursuer ($\hat{\boldsymbol{x}}_P$) and the measured position vector of the target ($\hat{\boldsymbol{x}}_T$), the line-of-sight vector can be defined as:

$$\boldsymbol{r} = \hat{\boldsymbol{x}}_T - \hat{\boldsymbol{x}}_P \tag{4.1}$$

For a constant velocity, the centripetal acceleration of the pursuer ($\boldsymbol{a}_P$) can be written in relation to the turn rate extracted from the guidance law in vector form as:

$$\boldsymbol{a}_P = \dot{\boldsymbol{\gamma}} \times \hat{\boldsymbol{x}}_P \tag{4.2}$$

The line-of-sight rate vector ($\boldsymbol{\omega}$) can be written as:

$$\boldsymbol{\omega} = \frac{\boldsymbol{r} \times (\hat{\boldsymbol{v}_T} - \hat{\boldsymbol{v}_P})}{|\boldsymbol{r}^2|} \tag{4.3}$$

The deviation angle $\boldsymbol{\delta}$ is given in vector form as:

$$\boldsymbol{\delta} = \left(cos^{-1} \frac{\boldsymbol{r}.\hat{\boldsymbol{v}}_P}{|\boldsymbol{r}||\hat{\boldsymbol{v}}_P|} \right) \left(\frac{\boldsymbol{r} \times \hat{\boldsymbol{v}}_P}{|\boldsymbol{r} \times \hat{\boldsymbol{v}}_P|} \right) \tag{4.4}$$

The forward Euler method is used to solve the guidance equations in discrete time using the following two difference equations:

$$\boldsymbol{v}_{P_{n+1}} = \hat{v}_{P_{n+1}} \frac{\boldsymbol{v}_{P_n} + \Delta t\, \boldsymbol{a}_{P_n}}{|\boldsymbol{v}_{P_n} + \Delta t\, \boldsymbol{a}_{P_n}|} \tag{4.5}$$

$$\boldsymbol{x}_{P_{n+1}} = \boldsymbol{x}_{P_n} + \Delta t \boldsymbol{v}_{P_n} \tag{4.6}$$

Where $\hat{v}_P = |\hat{\boldsymbol{v}}_P|$ denotes the measured GPS speed of the bird and where the subscript notation indicates variables at successive timesteps such that $t_{n+1} = t_n + \Delta t$. The centripetal acceleration a_P commanded by the guidance law is first used to determine the direction of the simulated velocity at the next time step. The magnitude of the rotated simulated velocity vector is then normalised to match the actual measured speed of the bird. The simulated velocity is then used to calculate the simulated position of the attacker at the next time step $\boldsymbol{x}_{P_{n+1}}$ as commanded by the guidance law. The step size (Δt) in the simulations was made small enough to guarantee the accuracy of the fitted guidance parameters and the prediction error to the level of precision at which they are reported.

4.2.4 System identification

We fitted the guidance constants N and K for different values of time (sensorimotor) delay τ for each of the 42 flights independently under PP, PN and PN+PP guidance laws. The time delay was varied from $0 < \tau \leq \tau_{max}$, where $\tau_{max} = 0.2\,s$ with an interval of $0.005\,s$. Each delay (τ) represented a time shift between the bird and lure trajectories, which were simulated from $t = \tau_{max}$ (here $\tau_{max} = 0.2\,s$) to the point of intercept to ensure that the same section of the flight was simulated independent of the delay for a particular run. For each flight and delay value, we used a Nelder-Mead simplex algorithm in MATLAB to find the value of N and K that minimised the prediction error (ε), defined as the mean absolute distance between the measured ($\hat{\boldsymbol{x}}_{P_n}$) and simulated positions ($\boldsymbol{x}_{P_n}$) of the bird at each time point (n):

$$\varepsilon = \frac{1}{k} \sum_{n=1}^{k} |\boldsymbol{x}_{P_n} - \hat{\boldsymbol{x}}_{P_n}| \tag{4.7}$$

The optimal delay value was identified as the one that minimised the prediction error across the tested range per flight.

4.3 Results

4.3.1 Gaze Analyses

To understand the characteristics of the bird's head movements during pursuit, we conducted observations of the data in the time and frequency domains across 42 recorded flights. Our dataset includes synchronised GNSS position data for hawk and target and inertial data from the bird's head for each flight categorised by individual. In the main text, we present data from a single flight representative of the characteristics observed throughout the dataset and statistical comparisons across all flights, whilst a larger selection of time domain data can be seen in the supplementary text (see Fig. C.3). Fig. 4.2A presents the inertially and locally derived angles that define the bird's head and body motion relative to a target. Inertially derived angles are defined relative to north (N). The line-of-sight vector between the bird and target has LoS angle, λ, the track angle, γ is defined as the inertial angle of the velocity vector and the gaze direction bearing, θ is the inertial angle of the bird's head direction. Deviation angle, δ is defined as the angle between the bird's velocity vector and the LoS vector, the head-velocity angle, ϕ is the angle between the bird's gaze direction and its velocity vector and the head tracking error ε represents the tracking error of the head to the target and is defined as the local position of the target in the bird's head coordinate frame centred about the mid-sagittal plane ($\varepsilon = 0$ as shown by the dotted line in Fig. 4.2B). In this analysis, we approximated the retinal coordinate of the target using the head tracking error since we have no knowledge of eye movement. Fig. 4.2B presents the visual field of a Harris's hawk as measured by Potier et al [22]. The Harris's hawk has a binocular field covering 47°, a total visual field of 162° and a blind area of 83°. The location of the temporal fovea (TF) and central fovea (CF) have been approximately marked. Using foveal location identified in the little eagle (Hieraaetus morphnoides) [21], which is in the same family as Harris's hawks (Accipitridae), we assumed that the temporal foveae are approximately located around $5° - 10°$ from the mid-sagittal plane. We also assumed that the central

fovea is located centrally in the field of view of each eye, which in Harris's hawks is located at 57.5° from the mid-sagittal plane of the head.

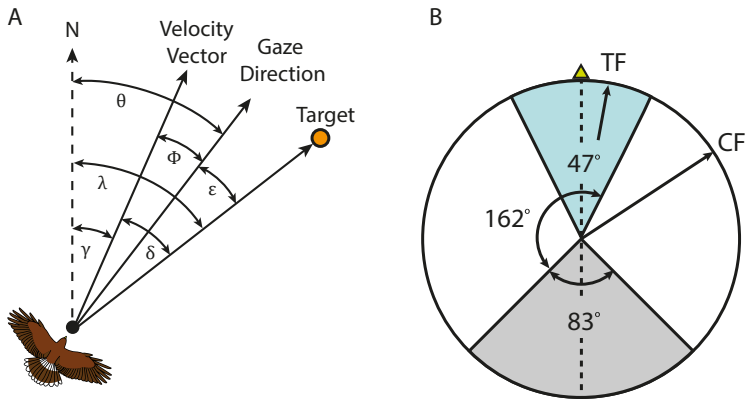


Figure 4.2: Inertial angle definitions and visual field of the Harris's hawk. (A) Definition sketch showing: North inertial reference (N), the line-of-sight angle λ, the deviation angle, δ, track angle, γ, head tracking error ε, inertial head direction bearing, ω and the gaze direction to velocity vector angle, ϕ. Inertial angles are defined anticlockwise positive relative to North (N), bird and target locations are as shown. (B) Horizontal section showing the Harris's hawk visual field with the binocular overlap of the temporal foveae in blue, the lateral field in white and the blind area in grey. The full field of each eye is shown as 162°. The approximate locations of the temporal and central foveae are marked as TF and CF respectively. The mid-sagittal plane is depicted by the dotted line and the bill tip is marked by the yellow triangle.

Although we analyse data from all the flights in subsequent sections, we begin by looking at a single flight to introduce the structure of the time series data. Figure 4.3 presents data from a single flight that exhibits significant bird turning. The gyro measurements from the head-mounted IMU provide insight into the angular rate of the head in three axes. Evident throughout each flight are head saccades visible as peaks in yaw rate. Fig. 4.3B presents both the yaw rate and the vertical acceleration (a_Z) (from the accelerometer) of the head during a single flight in addition to the gaze bearing. Peaks in Z acceleration are a result of the bird's wingbeats. The power spectra in Fig. C.1 show that these occurred at a frequency of approximately 4 Hz (the peak around 0 Hz indicates the DC offset of the yaw rate signal). This 4 Hz peak is also present in the power spectra of yaw rate. Periods where the bird was gliding (no flapping) can be seen where the acceleration is approximately

$a_Z \approx 0\,\mathrm{m\,s^{-2}}$. At the same time, yaw rate peaks are present, indicating that head saccades occurred in phase with the wingbeat frequency.

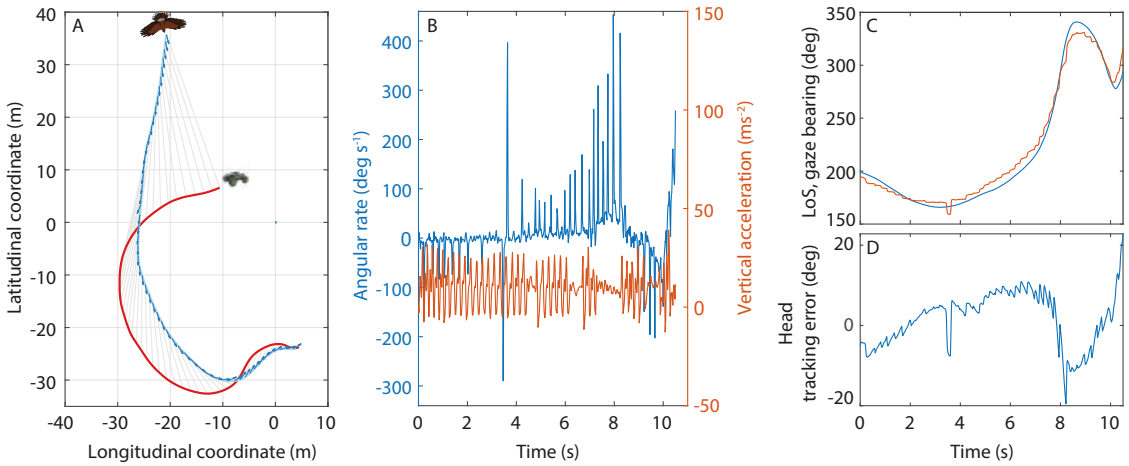


Figure 4.3: Time histories over the single flight shown in (A): 2D trajectory plot showing how the head gaze bearing (blue arrows) and instantaneous line-of-sight (grey) between the hawk (blue) and the target (red) varies throughout the flight. Hawk and target start locations are indicated by the overlaid images. (B) shows the angular rate and vertical acceleration as recorded by the IMU on the head of the bird. (C) presents the head gaze bearing (red) and the line-of-sight bearing, λ (blue). (D) shows the head tracking error ε between the target LoS and gaze bearing.

Step changes in gaze bearing, θ were also an indicator of head saccades and varied in magnitude dependent on bird-to-target range. Measurement of saccade angular velocity was hindered by the 50 Hz IMU sample rate but reached measured speeds above $400\,^\circ\,\mathrm{s^{-1}}$. For the majority of the flight in Fig. 4.3C, saccades were regular and amplitude between 2° and 8°; however, in the terminal phase, when the range to the target was $<4\,\mathrm{m}$, saccades increased in amplitude to between $10^\circ - 15^\circ$ during large turns to allow the required gaze redirection. Over the flight, the gaze bearing can be seen to closely track the inertial line-of-sight, with an offset that is equal to the head coordinate. According to Fig. 4.3D (and Fig. C.5), throughout the majority of the flight with the exception of very large saccades, the bird keeps the target within ±10° in the head coordinate frame. This range is within the ±23.5° range of the binocular field of the temporal foveae and suggests that the bird does not use unilateral foveation of the target, which would lead to a fixed head coordinate at approximately +10° or −10°, but rather allows the target to

drift in the retina within the region of binocular overlap. The head coordinate shifts in a sawtooth pattern; a feature typical of the optokinetic reflex (OKR) of the eye.

In Fig. 4.4, we present a focused view over a single head motion sequence characterised by a saccade with high yaw rate (between 6.38 s and 6.44 s) and then a longer period of minimal yaw rate in the intersaccade region between 6.44 s and 6.66 s (see Fig. 4.4 A-B). A prior note on IMU accuracy in the interpretation of this figure: heading accuracy of the IMU was ±2.5 degrees [98] and the observed shifts in head gaze bearing, LoS bearing and track angle have magnitudes greater than this. Firstly, the head was always oriented ahead of the target due to the positive positioning of the target in the head coordinate frame ($\sim 8 - 11°$). During the saccade, the head yaw rate was high and rapidly shifted the head's orientation by 4°, offsetting the head relative to the body by approximately 6°, which also turns during this time in synchrony with the wingbeat. The target head coordinate shifted by 3° (see Fig. 4.4). During the intersaccade period, the bird is turning as seen by the change in track angle (see Fig. 4.4B), which we approximate to represent the orientation of the bird's body in the absence of sideslip motion. Here, we can see that the head turn rate is lower than both the turn rate of the body (as approximated by track angle) and the LoS, which suggests that the head-neck motor compensation is commanded at a rate lower than the turn rate of the bird. To explore this further, we calculated the gain of the head motion defined as the ratio of the yaw rate of the head relative to the yaw rate of the body. This gain represents head stabilisation, where a gain of 0 represents no head stabilisation and a head orientation fixed to the body motion, whereas a gain of 1 represents perfect stabilisation and fixation on the background during a turn. Using the linear regression slope, we identified the head gain during this saccade to be 0.44, which is consistent with a low gain OKR which has a function to stabilise the background. The physical representation of this response will be for the head to move backwards relative to the body during a turn as it attempts to stabilise the background. This observation is replicated in other flights (see Fig. C.4). The drift of the head backwards relative to the body is also essential to reset the head-body angle to allow subsequent saccades throughout

the flight without resulting in excessive head-body offsets. We see that this also resets the position of the target in the head coordinate frame (Fig. 4.4C). All panels in Fig. 4.3 show that the target starts on the left side of the bird, transitions to the right and returns to the left at intercept. Given that the head coordinate is located within the binocular region, it is unclear which eye the bird is using to view the target and whether it switches between the two during the flight.

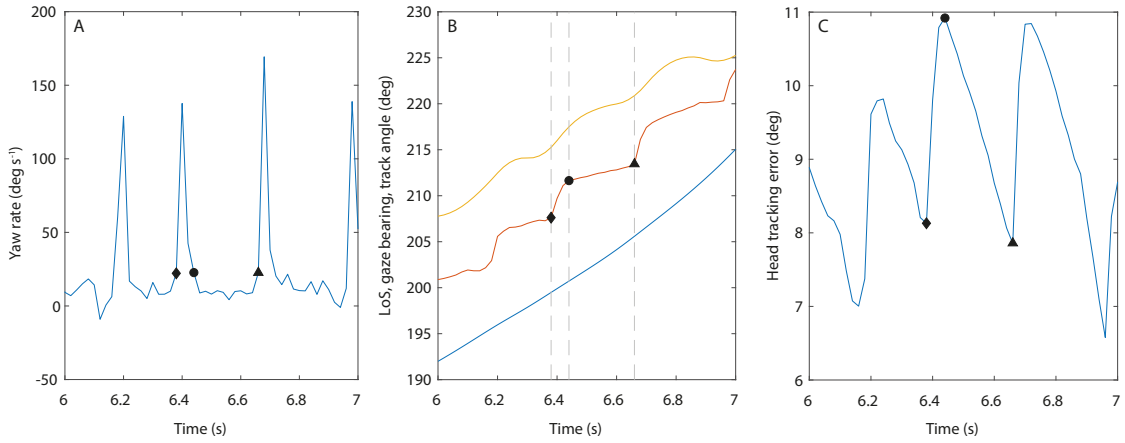


Figure 4.4: Time histories cropped between 6 and 7 seconds to display behaviour during saccade that starts at $t = 6.38\,\text{s}$ (diamond) and ends at $t = 6.44\,\text{s}$ (circle) with intersaccade period lasting until $t = 6.66\,\text{s}$ (triangle). (A) shows yaw rate measured using the gyro, showing peaks of angular velocity for 3 saccades. (B) shows head gaze bearing (red), LoS bearing (blue) and track angle (yellow) with dotted grey lines representing the three time points over all measurements and (C) shows the head coordinate between the target LoS and gaze bearing.

In Fig. 4.5, we plot the head tracking error for every sample measurement over the flight duration across all flights. The concentration of sample points in the binocular region (highlighted by the grey box centred around 0° agrees with findings observed in Fig. 4.3D) suggests that all five birds foveate the target in the temporal foveae in the binocular region and are not fixating the target using the central foveae. Using a single-sided distribution to assess foveation over both eyes together, the median tracking error of the data was 7.9°. Large values of head tracking error ($> 30°$) with low frequency are associated with takeoff and suggests that the bird is not fixated on the target during this period. Overall, this is consistent with the hypothesis that hawks use gaze shifts to reorient the head towards the target, but within a range defined by the binocular overlap of their visual field.

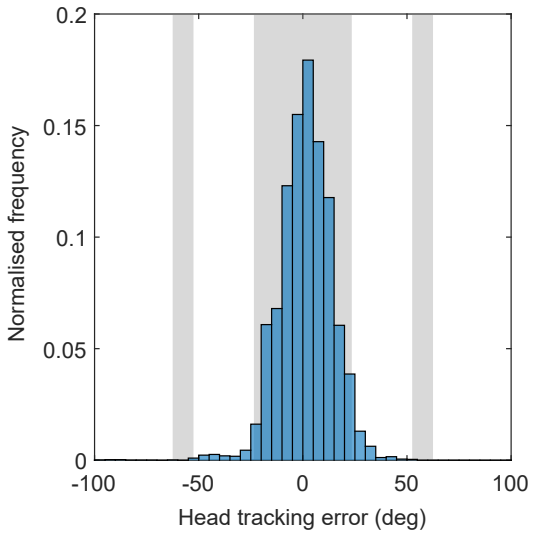


Figure 4.5: Histogram of the 2D head tracking error, ε in degrees for every sample over all flights. Y-axis values are normalised by relative probability calculated as the number of samples in each bin divided by total number of samples. Grey shading represents the binocular overlap region of the temporal foveae covering 47° of the frontal visual field (central) and the proposed region of acuity in the central foveae (side) centred around ±57.5° in the visual field from the mid-sagittal plane.

We suggest the observed gaze strategy of the head to be a saccadic tracking strategy that is characterised by high frequency, small angle saccades that regularly update the target position in the field of view similarly to a continuous tracking technique, but with periods of fixation where a low gain OKR is active, which stabilises the image to the background and resets head position. Hawks may be unable to perform smooth (continuous) pursuit with their heads as a primate can, but this strategy would be unlikely to provide the target information that the birds require for guidance during rapid turns that they perform during pursuit. The saccade and fixate strategy that prioritises continual target tracking is able to sufficiently reduce image blur and allow high frequency target information updates to input to their guidance system.

4.3.2 Proxies

Guidance model fitting to bird flight trajectories in Harris's hawks, peregrine falcons and gyrfalcons [10–12] to date have utilised the line-of-sight rate and deviation

angle (where fitting the PN+PP mixed guidance law) derived using knowledge of the positions of the attacker and target; however, the bird does not have this information available to it to calculate these parameters based on position and instead it must use its local sensory systems (visual, vestibular, proprioceptive). In the frame of the attacker, the line-of-sight rate of the target can be derived as the sum of the head yaw rate and the retinal drift rate of the target if the bird executes a gaze strategy where the head is constantly tracking the target. From our results (see Figs. 4.3, 4.4 and 4.5), we suggest the birds are implementing a discontinuous gaze strategy to do this. We therefore use the head yaw rate as a proxy for line-of-sight rate in proportional navigation measured via the vestibular system. We propose that the bird is able to measure the angle between the singularity of their optic flow (representing the velocity vector) and the target position in the retina (retinal coordinate) to determine the deviation angle. Again, using the observed gaze strategy where the head continuously tracks the target ($\varepsilon = 0$), we use the angle between the velocity vector (track angle) and the head bearing as a proxy.

To use head yaw rate as a proxy for line-of-sight rate, the noise on the signal due to flapping, head saccades and other disturbances needed to be filtered to extract the low frequency component. Straka et al [115] suggested the presence of low-pass and band-pass neuronal filters in the VOR pathway. Likewise, the thalamus, the relay centre for sensory information acts as a low-pass filter [116]. Since self-angular rate is measured by the bird using the vestibular system, these neuronal filters likely apply across any vestibular output. We therefore used a low-pass digital filter to modify the yaw rate signal. The cutoff frequency of this filter was optimised using an exhaustive search between the range:$f_c = [0.5 : 0.1 : 5]$ Hz, using 5 Hz as an upper limit based on the identified wingbeat frequency, which give an optimal cutoff frequency of 1.5 Hz (see Fig. C.2). For consistency, we applied the same low-pass filter to the gaze-velocity angle ψ, deviation angle δ and LoS rate λ for use in the below comparisons and guidance modelling.

The spatial histograms presented in Figs. 4.6 A-B show that across all flights, the head yaw rate and the gaze-velocity angle are good proxies to the LoS rate and

deviation angle respectively. The wider spread in gaze-velocity proxy indicates a lower correlation that physically represents an offset between the proxy and truth resulting from omission of the head tracking error. The proportionality indicates that the proxies approximate the target parameters well and that gradients of both truth and proxy measures are very similar. Time domain analyses in Figs. 4.6 C-D support these findings; showing that yaw rate is a good proxy to LoS rate and gaze-velocity is a good proxy to deviation angle. We now use these proxies in guidance modelling to assess their performance in simulating the measured bird pursuit trajectories to understand whether these inputs may be used rather than the traditional parameters of LoS rate and deviation angle in PN, PP and PN+PP guidance.

4.3.3 Guidance Modelling

The hawk's measured flight trajectories were simulated using a forward Euler method with three guidance laws: PP, PN, PN+PP, which generate a centripetal acceleration command. Please refer to the material presented in section 3.2.5 for detail.

See Fig. 4.2A for a definition of the angles that define the geometry of pursuit in the inertial frame.

The goal of simulating the intercept trajectories was to assess the performance of head yaw rate as a proxy for LoS rate and the gaze-velocity angle as a proxy for deviation angle. Head data was only available as a time history of recorded measurements from the bird over each flight. To enable a paired statistical test to ascertain fit performance with proxy inputs, we compared simulations using head data derived proxies to the truth LoS rate and deviation angle derived from the recorded positions of the bird and target during each flight. Simulations were run given knowledge of the attacker's initial position and velocity and the time history of the attacker's ground speed and the target's position. With a free running simulation, the simulated velocity and position at the previous time step would then influence the acceleration commanded by each guidance law (as in Brighton and Taylor [11]). However, in these simulations we used the values of bird and target position and velocity (lagged by tau) as measured from each flight as the input to the guidance

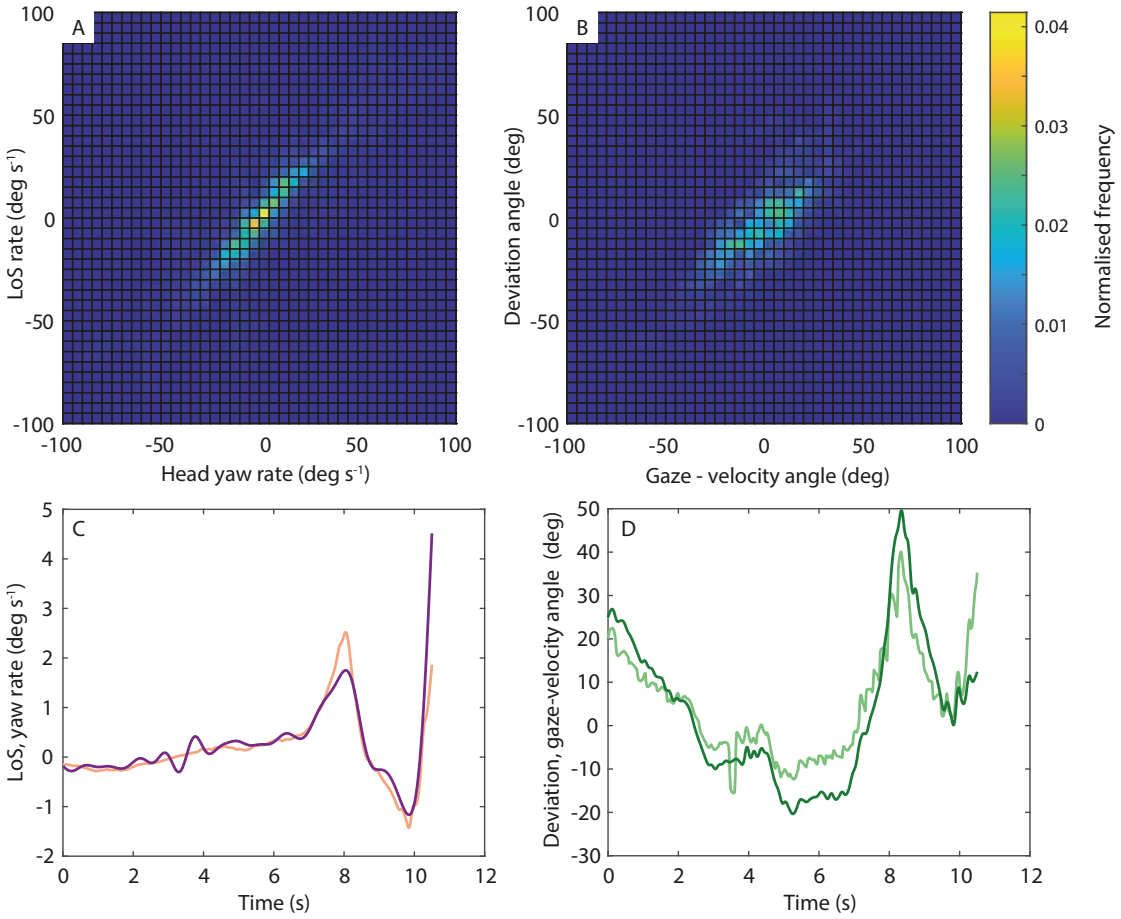


Figure 4.6: Time history and correlation spatial histograms to assess the suitability of head yaw rate as a proxy to line-of-sight rate and gaze direction to velocity angle as a proxy to deviation angle. (A) presents the correlation between the bird's head yaw rate and line-of-sight rate and (B) presents the correlation between deviation angle and gaze-velocity angle. Both spatial histograms (A, B) show correlation over all sample points for all flights with frequency normalised by relative probability. (C) presents a time history of measured LoS rate $\dot{\lambda}$ (red) and filtered head yaw rate $\dot{\theta}$ (purple), whilst (D) presents the deviation angle δ (dark green) and the gaze-velocity angle φ (light green) for a single flight.

acceleration command. The hawk's simulated ground speed was always matched to the measured GPS ground speed. Overall, there were two scenarios tested for PP, PN and PN+PP guidance laws with measured inputs of true LoS rate $\dot{\lambda}_T$ and deviation angle $\dot{\delta}_T$ and proxy inputs of head yaw rate $\dot{\theta}$ and gaze-velocity angle ϕ.

Previous work found that optimising the parameters N, K, τ for PN+PP and N and τ for PN globally across all flights resulted in good fit performance that eliminated the risk of overfitting to the data. Using the measured inputs in the way described above from each flight resulted in high fit error when fitting

Table 4.1: Results of guidance fitting with proxy and truth input guidance parameters for PP, PN and PN+PP guidance models. Bootstrapped 95% confidence intervals are presented in parentheses.

Model	Input	Median (95% CI) of RMS Error (m)	Median (95% CI) of N	Median (95% CI) of K (s^{-1})	Median (95% CI) of delay (s)
PP	Proxy	4.26 (2.64, 5.45)	-	-0.08 (-0.78, 0.17)	0.07 (0.00, 0.10)
	Truth	4.71 (3.14, 6.40)	-	-0.38 (-0.87, -0.08)	0.00 (0.00, 0.04)
PN	Proxy	2.73 (1.78, 4.10)	0.95 (0.62, 1.25)	-	0.00 (0.00, 0.10)
	Truth	3.38 (2.39, 4.99)	1.00 (0.60, 1.21)	-	0.00 (0.00, 0.10)
PN+PP	Proxy	0.70 (0.40, 1.40)	1.15 (0.98, 1.35)	0.36 (-0.03, 0.65)	0.02 (0.00, 0.09)
	Truth	1.42 (0.80, 1.97)	1.53 (1.14, 2.03)	0.68 (-0.09, 0.96)	0.06 (0.00, 0.10)

globally with measured data from the bird. We therefore optimised the parameters individually to each flight.

4.3.4 Guidance modelling results

Using the three guidance models in equations 1.2, **??** and 1.3, we identified the unique combination of N, K and τ that minimised the prediction error, ε (root mean squared error between the measured and simulated bird trajectory) for each flight using two parameter definitions of LoS rate and deviation angle: proxy and truth. The distribution of prediction error (ε) and the distribution of fitted values (N, K) over all 42 flights are plotted as histograms in Figs. 4.7 and 4.8 for PN, PP and PN+PP and each parameter definition. We then calculated the parameter medians; $\tilde{\varepsilon}$, $\tilde{N}$, $\tilde{K}$ and their respective bootstrapped 95% confidence intervals using 10000 bootstrap samples. Results are presented in Table 4.1.

Our results show that the mixed guidance law is the best fitting model of the data and presents a reduction in median error when compared to PP and PN; an observation that is in accordance with findings from Brighton and Taylor [11]. Simulation using proxy rather than truth inputs improves the model fit through a reduction in median RMS error independent of the guidance law used. With the mixed guidance law, fitting with $\text{PN+PP}_{\text{proxy}}$ improved the median (denoted by tilde) prediction error to $\tilde{\varepsilon}_{Proxy} = 0.70\,m\,(0.40, 1.40\,m)$ from $\tilde{\varepsilon}_{Truth} = 1.42\,m\,(0.80, 1.97\,m)$.

Given the very low RMS error when simulating with PN+PP$_{\text{proxy}}$, we have chosen to present the median and IQR of fitted trajectories using this guidance law in Fig. 8. The median value of the fitted parameter $\tilde{N}_{PN+PP} = 1.15$ and has a narrow confidence interval around 1; however, there is a lack of certainty around the constant $K_{PN+PP} = 0.36\,s^{-1}\,(-0.03, 0.65)\,s^{-1}$ since the confidence interval overlaps 0. We conducted a sign test ($p = 0.16$) which shows that K is not significantly different from 0 at the 95% confidence level; however, the negative overlap is marginal and this may simply reflect low statistical power. If modelling using PN+PP, it is best to use proxy input parameters of head yaw rate and gaze-velocity angle.

Of the two single parameter models, PN appears to fit the data better than PP, but this is not statistically significant at the 95% confidence level (Wilcoxon test: $p = 0.095$, $z = -1.67$). A larger sample size would improve the robustness of our statistical comparisons. We are able to statistically compare the results of PN and PP since they both have the same number of fitted parameters (84); however it is not possible to make a similar comparison to PN+PP which has 126 fitted parameters and will always fit the data at least as well as either PN or PP, which are just special cases of PN+PP with $K = 0$ and $N = 0$, respectively. For PP, although the median error was improved by using the gaze-velocity angle proxy input, given the very high error and wide confidence intervals we conclude that the bird is not using proportional pursuit in flight. Interestingly, fitting proportional navigation with Harris's hawks typically leads to an fitted value of the navigation constant N around 1 [11]. This is not the case with fitted data found in peregrines. The best fitting value of N fitted for PN+PP$_{\text{proxy}}$ is also within this range.

Overall, the reduction in median prediction error across all flights when using proxy measures when compared to truth values indicates that head yaw rate and gaze-velocity angle provide a better fit to the bird's behaviour in simulation and suggests that these measures could be closer to the parameters that the bird uses to guide its flight.

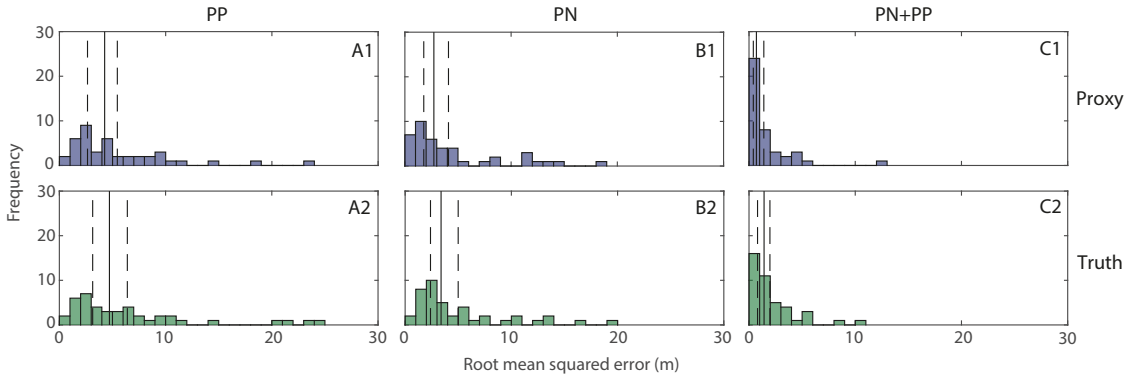


Figure 4.7: Histograms of the root mean squared error over all flights for PP (A), PN (B) and PN+PP (C) guidance models when using input proxy (1) or truth (2) guidance parameters. Row 1 indicates use of proxy values; head yaw rate $\dot{\theta}$ and gaze-velocity angle φ (for PN+PP) as input parameters. Row 2 indicates the use of the true line-of-sight rate $\dot{\lambda}$ and deviation angle δ as measured from the bird in flight as input parameters. Vertical solid line indicates the median error and dotted lines show the 95% confidence interval around the median.

4.4 Discussion

4.4.1 Gaze Strategy

Stabilisation of gaze is a low-level optomotor response that is essential for vision-based tasks allowing a stable view to assess behaviourally relevant features in the environment and to determine self-motion and orientation in space (balance and aerodynamic stability, orientation relative to gravity). Goal-directed behaviours such as prey pursuit are a higher-level process that rely on both gaze stabilisation for target identification and a gaze strategy to redirect the visual system in support of a task such as target tracking or collision avoidance. These two processes can be separated into a control system, where stabilisation reflexes occur in an inner loop and the outer loop controls goal-directed behaviour [117]. Inner loop gaze stabilisation operates as reflexes and is multimodally controlled via the OKR and VOR. Outer loop control modifies the inner loop gaze stabilisation since otherwise, the animal would be unable to perform voluntary movements without being driven back to the current equilibrium. Identifying the system in this way, we can associate the gaze strategy of the bird during pursuit with the outer control loop.

When taking a system overview in terms of target guidance as the outer loop

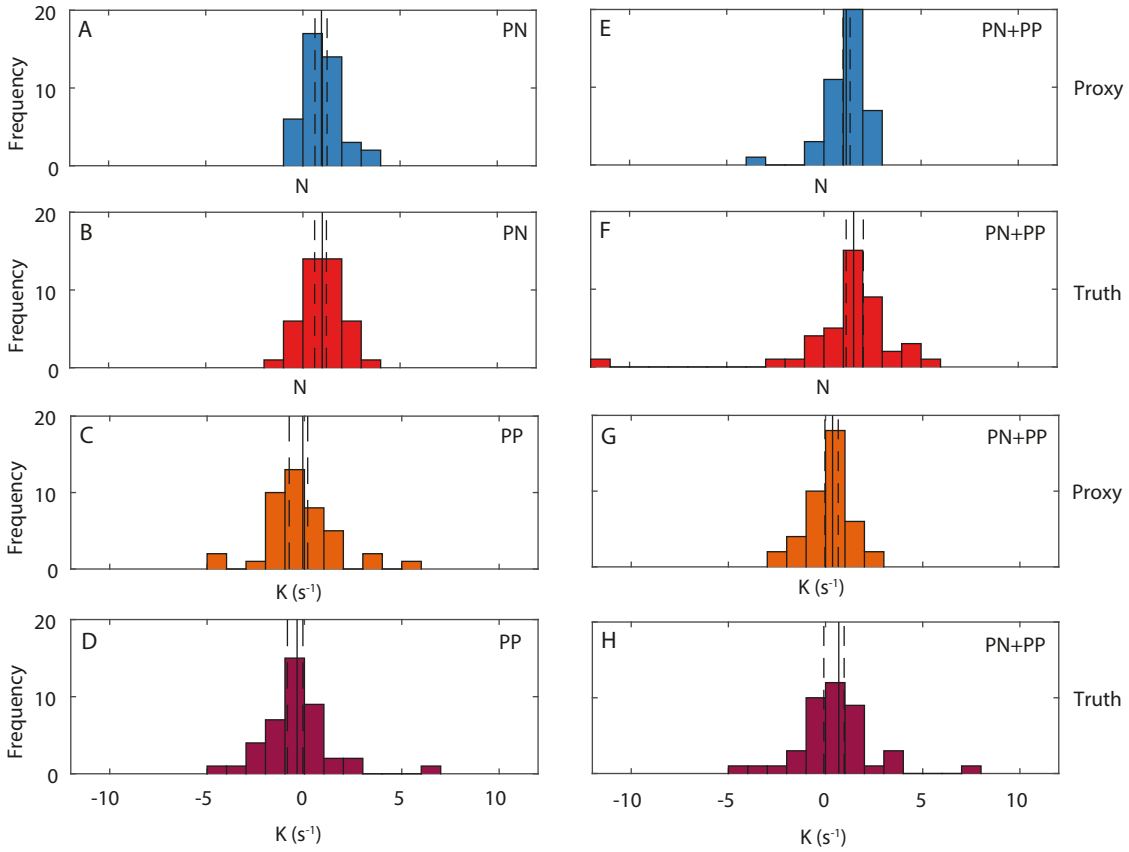


Figure 4.8: Histograms of the fitted guidance parameters N and K for PN (A-B), PP (C-D) and PN+PP (E-H) guidance laws simulated using proxy and truth inputs. Proxy inputs use head yaw rate $\dot{\theta}$ and gaze-velocity angle φ, whilst truth inputs use the true line-of-sight rate $\dot{\lambda}$ and deviation angle δ as measured from the bird in flight. Vertical solid line indicates the parameter median and dotted lines show the 95% confidence interval around the median.

controller, the inner loop control is defined by the gaze strategy of the bird, which itself has an inner loop that stabilises gaze. Initially we hypothesised that the hawks may be using a gaze strategy that either continuously tracks the target similarly to a primate using smooth pursuit or a gimballed missile seeker, where the head would continuously be driven to foveate the target or alternatively a strategy that leverages the bird's saccade and fixate behaviour, where the head is held fixed inertially and the target is able to drift across the retina. However, in our analyses, we identify a saccadic tracking strategy. The observed head saccades were often and small angle adjustments. This is in contrast to large head saccades ($> 20°$) observed in pigeons [44, 110] and lovebirds [109] when engaged in non-pursuit behaviours and the high amplitude head saccades found during blowfly flight to the

order of several tens of degrees up to 90 degrees [46]. Small saccade amplitude in the range of 5° implies an attempt at a continuous tracking strategy such as that used in primates with smooth pursuit [118] and in gimballed missile seekers [49], but with the limitation of the hawk's neck motor system only permitting saccadic motion of the head. We identified this behaviour as a saccadic tracking technique which regularly updates gaze direction with small angular changes in phase with the wingbeat frequency ($\sim 4\,\mathrm{Hz}$) (in accordance with findings in pigeons [44] and lovebirds [109]). The identified behaviour is consistent with a gaze strategy that drives the head parallel to the line-of-sight vector between the bird and the target, with an offset defined by the coordinate of the target in the head frame, which is allowed to drift across the binocular field of the retina. The head is neither fixed to the body nor fully stabilised, as we identified a head gain relative to body rotation of 0.44; indicating low gain OKR head stabilisation during in the intersaccade region. This gain is similar to that identified in hawkmoths, which was around 0.5 [119]. One can apprehend the lack of perfect head compensation (gain=1) during the intersaccade region since without, there would be no error feedback for correction when using the OKR or VOR for gaze stabilisation.

These findings are interesting, since there are two beneficial outcomes for a bird using this saccadic tracking strategy: a proxy for the LoS rate in the low-pass filtered head yaw rate because the smoothed version of the signal tracks the target, and a stabilised view of its world because the head is reasonably well stabilised during the intersaccadic periods, with the observed low-gain OKR.

The observed sawtooth motion of the head coordinate caused by OKR of the head during body turning is often small ($< 5°$) and perhaps compensated for by vestibular-ocular eye movements which stabilise the eyes relative to the external background and therefore may stabilise the target on the retina, since they are within the known measured range of eye movement in similar species; the red-tailed and Cooper's hawk [19]. We also postulate the presence of some additional reflexes that control head motion that result from the target not being in the visual field and when there is a high offset angle of the head relative to body (far from equilibrium).

4.4.2 Mechanisation of guidance

In guidance simulation, we found the mixed guidance law with proxy inputs of head yaw rate and gaze-velocity angle to best model the data over simulations using truth inputs. Previous experimentation has found the mixed guidance law effective in modelling Harris's hawk pursuit, but PN has also been found to model flights well with fewer fitted parameters [11] and in this study, we find PN to be an acceptable single parameter model when using proxy inputs. To implement guidance using PN in homing missiles, determination of the LoS rate is required and is achieved through a gaze strategy that minimises tracking error between the seeker centreline and the target LoS by continuously driving the seeker centreline to the target line-of-sight. In missile terminology, the seeker is analogous to a birds' head and the tracking error is analogous to the head coordinate. This inner tracking loop has the effect of always keeping the target within the field of view and allows approximation of the inertial LoS rate by equating this to the seeker yaw rate [49]. There are several methods by which the missile system obtains LoS rate information for input into PN guidance using either LoS reconstruction or LoS rate reconstruction. For example, LoS reconstruction takes the sum of the seeker yaw rate and the tracking error, whilst rate reconstruction takes the sum of the seeker yaw rate (from gyro) and the differential of the tracking error. In missile systems, guidance filters are used to derive required states (e.g. LoS rate, relative velocity) and mitigate the impact of noise on the input measurements. LoS rate reconstruction may suffer from excessive measurement noise amplification resulting from the differential method [49]. In hawks, we propose a combination of rate measurements in birds that would not be subject to these amplification issues.

In Harris's hawks, mechanisation of target guidance using PN or PN+PP requires measurement of target information from the bird's sensory systems to input into the guidance loop. We found similarity between the gaze strategies employed by missile seekers and Harris's hawks. Both the continuous and saccadic tracking strategies attempt to maintain the head directed towards the target so are conducive to using the low-pass filtered head yaw rate signal as an approximation to LoS rate (see Figs.

4.6 A, C). Since our results showed this to be a good approximation, we modelled guidance in simulation using the assumption that the hawks measure angular head rate via the vestibular system and input this information into their guidance loop. Given that median simulation error across all flights when using the head yaw rate proxy was lower than when simulating using measured inertial LoS rate, we propose that the hawks may be using this as an input to PN and PN+PP guidance. We draw comparison to missile systems, where LoS rate is approximated as seeker (head) yaw rate summed with tracking error rate. Although we modelled guidance using only head rate, with the use of the saccadic gaze strategy which does not perfectly track the target on a fixed retinal coordinate, it is more likely that the hawks would approximate target LoS rate as the tracking error rate obtained as the drift of the target across the retina during the intersaccade period in addition to the filtered head yaw rate signal much like in the missile system. Our results also showed that the angle between gaze bearing and the bird's track angle (the inertial angle of the bird's velocity vector) is a good proxy to the deviation angle. We suggest that gaze-velocity angle can be measured by the hawk as the angle between the head bearing determined via the vestibular (or proprioceptive) system and the singularity of optic flow obtained using the visual system. In guidance modelling, we model the delay τ to represent the motor delay present between the visual system receiving target information and steering motor output. In modelling PN and PN+PP with proxy inputs, we find best fitting delay values of 0 and 0.02s respectively; much lower than the minimum associated with avian visuomotor control (0.03s) [109]. Since the head yaw measurement already has embodied sensory input and motor command delays associated with target tracking, it is unsurprising to find that we only need to add minimum to no delay in the model fitted with the head rate proxy. Missile system guidance filters use Kalman filtering to estimate input states; removing noise and delay, which would perform better than the low pass filtering implemented here. It is likely that the hawks are also able to do this.

The block diagram in Fig. 4.10 presents a hypothesis on how inner and outer loop control is implemented for prey pursuit in the Harris's hawk when using PN

guidance. Here, the LoS rate approximation is shown as the sum of head tracking error and head yaw rate, but the scenario that we simulated with head yaw rate as the only input can be achieved by removing the summing block and only taking input from the output of the vestibular system. The block diagram in Fig. 4.11 suggests how PN+PP guidance could be mechanised in the Harris's hawk when using a true measurement of deviation angle. By removing the addition of ε_m from the calculation of δ_m, the control flow that was simulated using a proxy estimate is obtained, where $\delta_{Proxy} = \theta - \gamma$.

The sketch in Fig. 4.9 presents the 2D angle definitions used in analysis of control flow in guidance. For the definitions not presented in Fig. 4.2 for the guidance analysis, λ_m is the measured or approximated line-of-sight angle, ψ is the inertial angle of the bird's body, β represents the angle offset of the head to the body described in the diagrams as neck angle. ε is the true head coordinate or tracking error, ε_m is the measured head coordinate, ε_{eye} represents the error in the visual system in determining the LoS angle and α represents the aerodynamic sideslip angle.

The block diagrams for PN and PN+PP guidance laws (Fig. 4.10 and 4.11) show an inner loop that drives head rate proportionally to the rate of change of the tracking error between the mid-sagittal plane and the true LoS angle to direct the head towards the target according to the discontinuous gaze strategy and extract guidance parameters via this process. Looking first at the block diagram for PN (Fig. 4.10), we first take the true LoS angle and subtract the body angle and neck angle to obtain the head coordinate. This is then measured by the target detection visual processing centre to obtain the measured head coordinate. We differentiate the signal to obtain the effective retinal drift rate and input this into the inner head tracking loop. The commanded neck yaw rate is the sum of the retinal drift rate and the current measured head rate. This accounts for body yaw rate so that commanded neck yaw rate is reduced if the body is already turning. We depict the inner loop that controls gaze strategy as the red box in Fig. 4.10. This keeps the head directed towards the target (as observed in a discontinuous gaze strategy). This is actioned by the neck-motor system to give an achieved

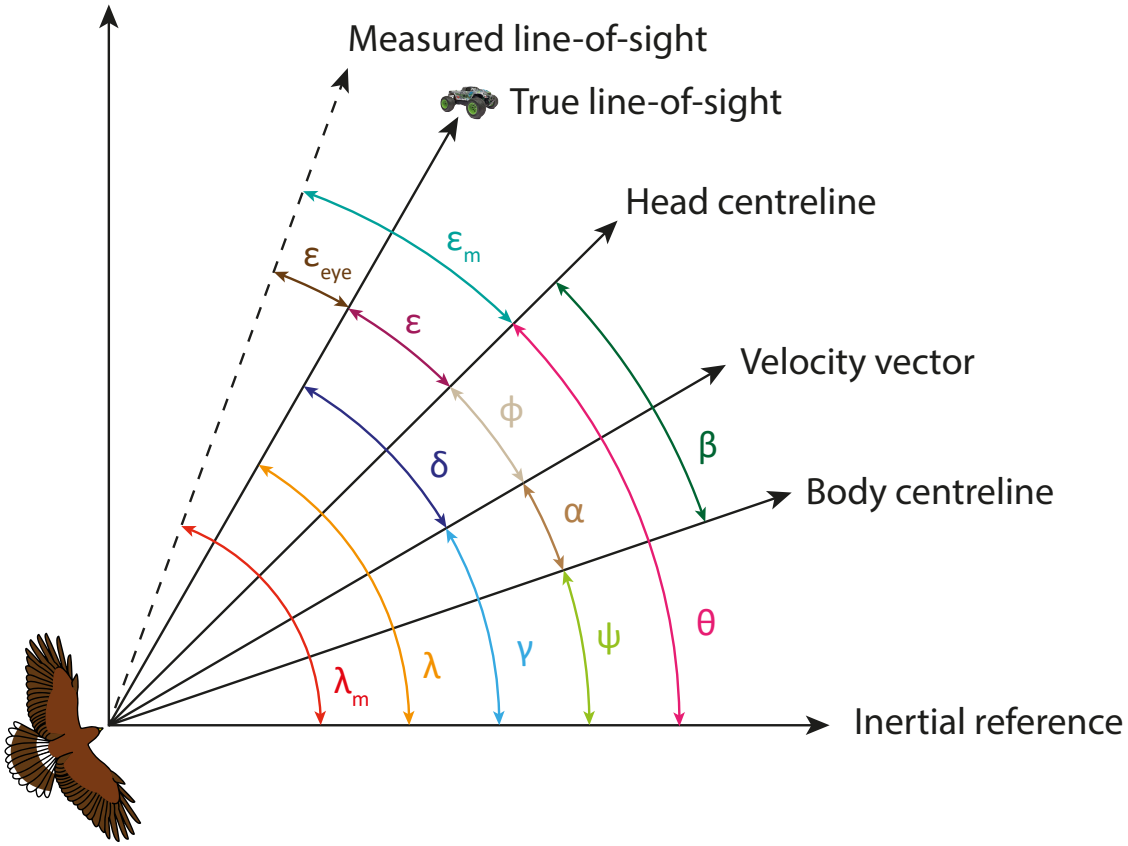


Figure 4.9: Definition sketch showing 2D angles used in guidance control analysis. Axes are relative to an arbitrary inertial reference. Arrowed lines show the body centreline, head centreline, velocity vector, true line-of-sight vector and the measured line-of-sight vector, which accounts for measurement error from the bird's visual system ε_{eye}, λ represents the inertial line-of-sight angle, λ_m represents the measured inertial line-of-sight angle, γ represents the inertial track angle, δ is the deviation angle, ψ is the inertial body angle, θ is the inertial head angle, β is the neck angle between the head and body, φ is the head gaze bearing to velocity vector angle, ε represents the head tracking error between the mid-sagittal plane of vision and the line-of-sight angle, ε_{eye} represents the measured head tracking error accounting for visual system measurement error and α represents the aerodynamic sideslip angle.

neck yaw rate $\dot{\beta}$ which is integrated to feed neck angle β back to the loop start and separately summed to the body yaw rate as:

$$\dot{\theta} = \dot{\beta} + \dot{\psi} \tag{4.8}$$

which can subsequently be measured by the vestibular system to obtain an estimate of head yaw rate $\dot{\theta}_m$ (includes vestibular measurement error). In our simulations, only the head yaw rate is input into a low pass (guidance) filter before

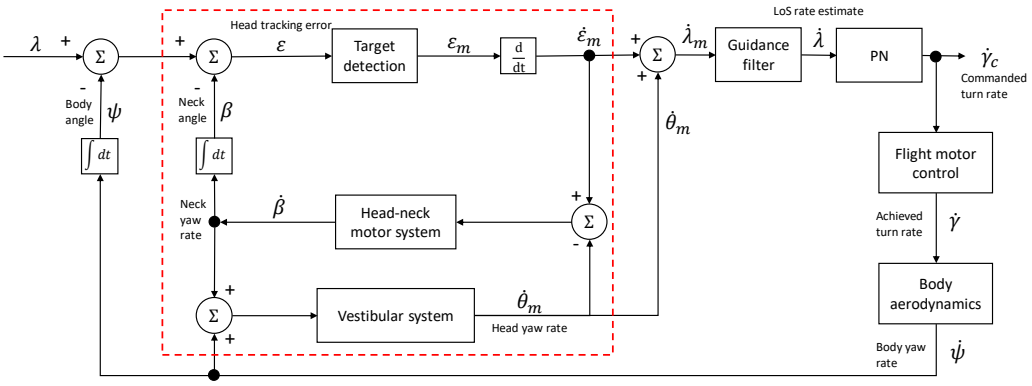


Figure 4.10: Block diagram for PN: presenting a hypothesis on the physiological pathways involved in the inner gaze stabilisation loop (in red) and how this feeds head yaw rate information into the outer PN guidance loop.

being input to the PN guidance law as a proxy for LoS rate. Due to the observed head coordinate drift observed in our data, it is likely that the bird also uses the retinal drift rate (ε_m) to estimate measured LoS rate as:

$$\dot{\lambda} \approx \dot{\varepsilon}_m + \dot{\omega}_m \tag{4.9}$$

which is shown in Figs. 4.10 and 4.11. The guidance law commands a turn rate, which is actuated by the bird's flight motor system (muscles) in a banking manoeuvre, which results in the achieved turn rate. This differs from the commanded turn rate due to limitations in control and actuation. Body aerodynamics must be considered to remove any sideslip angle α before integrating body yaw rate to the inertial body angle to feed back into the loop.

The requirement to estimate deviation angle distinguishes the PN+PP guidance law from PN and the control flow required to estimate this parameter. In Figure 4.11, we present the control loop for the mixed guidance law through estimation of the deviation angle δ_m. Using the visual coordinate system only, we hypothesise that the bird could measure the angle between the target and the singularity of the

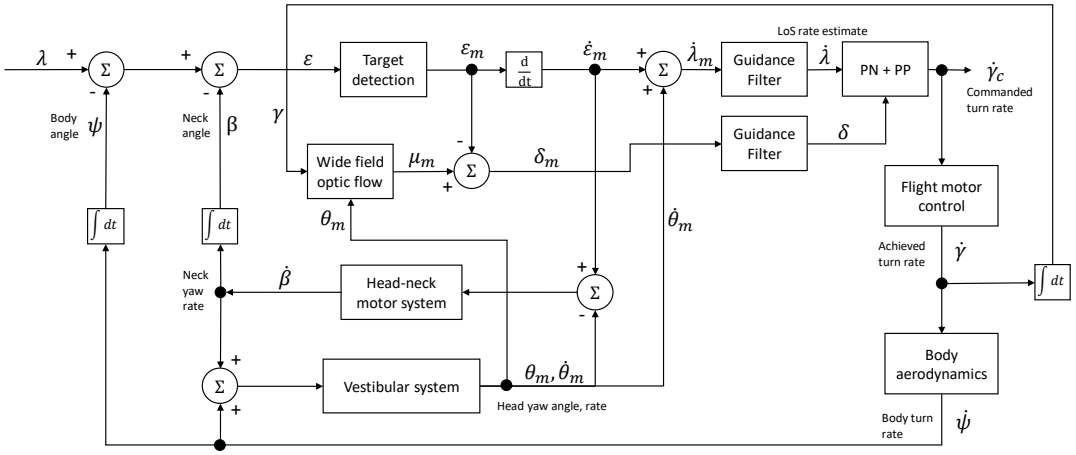


Figure 4.11: Block diagram for PN+PP: presenting a hypothesis on the physiological pathways involved in the inner gaze stabilisation loop and how this feeds line-of-sight-rate and deviation angle information into the outer PN+PP guidance loop.

optic flow field (δ_m) using wide field optic flow processing. In the block diagram, we illustrate the output of wide field optic flow processing as the angle between the mid-sagittal plane of the head and the optic flow singularity. This would estimate the deviation angle given a continuous gaze strategy; however, as we observed a discontinuous gaze strategy, the target is not always fixed on the head centreline so we include the tracking error from the target detection process to account for this discrepancy. Therefore, the measured deviation angle is the sum of:

$$\delta_m = \mu_m + \epsilon_m \tag{4.10}$$

We use the suggestion from Muller [114] that the vestibular system is likely able to measure angular displacement in addition to angular velocity and acceleration and so take the head yaw angle as a direct output. The approximated deviation angle is then input to a guidance filter and then into the guidance block in addition to the LoS rate estimate as described for PN to generate a steering command for the bird.

4.4.3 Limitations

The results of these analyses have provided insight into the gaze strategy utilised by Harris's hawks during pursuit flight and enabled hypotheses regarding the physiological pathways that mechanised guidance in the brain. There are however some limitations to the study that are described below.

There are uncertainties in the bird's gaze direction since we have assumed in the analysis that the bird's eye movements are negligible. At present, limited knowledge of eye movements in the Harris's hawk (during this task in particular) prevents a clear understanding of the retinal coordinate and where the target is fixated in the field of view or foveae of the bird. Given that eye movements measured in Cooper's and red-tailed hawks have been measured in the range $2° - 8°$ [19] it is possible that in Harris's hawks, these might contribute to further stabilisation of the image on the retina. In the head coordinate frame, we see that the head tracking error varies in a sawtooth pattern, which is indicative of a head OKR. We hypothesise that eye movements may correct this target motion and imply that the bird is smoothly tracking the target using combined head and eye movements. The amplitude shift is around 3° and eye movements of the order of $\pm 1.5°$ are biologically plausible. Less movement than this would result in imperfect image stabilisation whilst more movement would make the image unstable. We did not include eye movements in the block diagrams, which would constitute a separate inner loop to control eye direction.

Additional uncertainty in head orientation measurements may result from the IMU calibration procedure. We used meat to draw the attention of the hawk to the base station antenna from which the true gaze bearing was established. Using a camera behind the base station antenna to determine the time at which the bird is fixating in the correct direction. During this procedure, the birds changed gaze direction often and may have been fixating on other objects in the background. Using this method, it was difficult to determine the exact time which often lasted a duration less than 1 s. Timecode synchronization across the camera and two GNSS loggers was also difficult to establish and there may be some systematic error

present from this. We did have high confidence in the position accuracy of the GNSS data however, particularly from a stationary measurement, which reduced position uncertainty. In addition to calibration uncertainty, the low 50 Hz sample rate of the IMU led to peaks in yaw rate being severely reduced as this only allows a maximum measurement frequency of 25 Hz. This has implications for the measurement of maximum saccade angular rate and also may affect the result of low pass filtering the head yaw rate for use as a LoS rate proxy for guidance modelling.

We ran our analyses on a relatively small sample of flights (42) with unbalanced number of flights for each bird that ranged between n=5 and n=11. A larger dataset would allow a better understanding of gaze strategy across all flights and to determine any inter-individual variations in behaviour between the five hawks. This larger sample set would enable greater statistical power.

We modelled guidance to comparatively assess the performance of head yaw rate and gaze-velocity angle as proxies to LoS rate and deviation angle. To enable a paired test, we compared the simulation performance of this to $\dot{\lambda}_T$ and δ_T obtained from the measured flight data. Whilst this allows the most similar comparison, using truth parameters $\dot{\lambda}_T$ and δ_T is logically inconsistent. This is because the truth parameters only represent truth data at the true location of the bird, which the simulation deviates from. A better comparison would be to allow N to vary at every time step and see the difference in the variation of N between both methods; using the assumption that less variation in N is a better model.

4.4.4 Future work

Results from our behavioural experiment suggest that Harris's hawks mechanise a guidance law to guide their flight. Whether PN+PP or PN are true representations of the guidance loop active in the hawk's brain is undetermined; however, guidance simulations [11, 120] suggest that the mixed guidance law fits well to the measured trajectories over all flights and proportional navigation fits well but with a higher median error, which is to be expected given that it is a single parameter model compared to a two-parameter mixed model that contains proportional navigation

as a special case with $K = 0$. The block diagrams presented in Figs. 4.10 and 4.11 present hypotheses on the physiological pathways that might be present in the Hawk to guide pursuit flight. These include predictions on how sensory information could be obtained and combined to mechanise guidance using proportional navigation or the mixed guidance law. The obvious avenue for future work would be to test these hypotheses by analysing the neural encoding of sensory stimuli and guidance behavioural output. Currently, our guidance models do not include physics modelling and should include the physical constraints of the hawk's flight envelope, which would also be subject to variation based on individual flight morphology and physiology [121]. The assumption of fixed guidance constants throughout the pursuit flight is unlikely to be true and therefore we should allow for time variance in guidance constants.

5
Conclusions and Future Work

In this thesis, I investigated the visually guided flight behaviour of Harris's hawks; focusing on understanding prey pursuit through guidance modelling and analysis of gaze strategy and the potential influence of gaze strategy on the mechanisation of guidance via biological experimentation. To do this, I developed and validated a highly accurate and precise GNSS-IMU biologger that used a post processing correction to achieve this. I developed an 'interpolated PPK' method to use this correction when quality GNSS data is unavailable. Position and inertial data collected from Harris's hawks over N=54 pursuit flights was used to model their guidance and identify gaze strategy. This was then used to hypothesise the control loop that mechanises guidance during prey pursuit. The following chapter summarises the main conclusions from the preceding chapters, the limitations of the methods used and proposes directions for future research.

5.1 Conclusions

The work in this thesis presents a number of firsts in the areas of biologging and pursuit behaviour in raptors; encompassing guidance modelling and understanding gaze strategy through the recording of head movements during flight.

In Chapter 1, I introduced the limitations of existing studies in guidance modelling and the lack of knowledge in how gaze strategy influences how guidance is mechanised. The drawbacks in biologging technology used in current and former studies were outlined, which reinforced the need for an accurate and precise measurement system to measure animal movements. This established the rationale for the development of a PPK GNSS-IMU biologger for use in this experiment that is also widely applicable in the field of animal behaviour.

In Chapter 2, I outlined the development process of a PPK GNSS-IMU biologger. Whilst RTK; the real time equivalent of PPK has been used in similar studies, it had not been used with such high accuracy or low mass requirements as were used here. The logger constructed here was able to record raw satellite data for PPK processing, SBAS standard accuracy GNSS data and high sample rate inertial data from two IMUs. Furthermore, the novel correction method known here as interpolated PPK was developed and allowed a simple correction to standard accuracy SBAS data to achieve near PPK levels of accuracy (~ 0.01 m). The system was validated in stationary and dynamic tests to have an accuracy of under 0.02m; a significant improvement over other loggers used in similar studies. This was then used in data collection and analyses that were presented in Chapters 3 & 4.

Chapter 3 introduced the biological pursuit experiment and presented the results of guidance modelling to N=54 flights from n=5 Harris's hawks. Simulations were run for three guidance laws (proportional pursuit (PP), proportional navigation (PN), and the mixed guidance law (PN+PP)) and the mixed PN+PP guidance law was statistically found to perform the best when fitting globally to all flights. This was determined by establishing the unique combination of guidance constants (N,K,τ) that minimised the median root mean squared error over all flights. Given that the mixed guidance law was also found to best fit the flights of Harris's hawks to an erratically manoeuvring target [11], I compared the fitted model parameters between both studies which differed in the behaviour of the target (smooth vs erattic target). In comparing the trajectories simulated to each measured target dataset using the two sets of optimally fitted parameters (N,K,τ) I found that the

improvement in median RMS error when using the parameters fitted to that dataset was statistically significant. However, I was not able to draw any conclusions on the significance of the changes in guidance parameter tuning due to a small sample size. This study was also the first to make measurements of wind and to attempt to account for this. Wind has a significant impact on the accuracy of the pursuer and target trajectories since the pursuer is airborne and affected by wind, yet the target is a ground vehicle and unaffected. If both were either air or ground vehicles, the relative trajectories would be valid. This impacts guidance modelling, as in flight, the bird must apply flight control for target guidance and to counter wind drift. In this case, aerodynamic control is applied relative to the air velocity and so I established three alternative formulations of the mixed guidance law using parameters and control force relative to air velocity. Results indicated that the standard mixed guidance law is robust to the wind.

Chapter 4 presents the first time that the head movements of a raptor have been recorded and used in the analysis of gaze strategy during pursuit flight. Using GNSS position and inertial head gaze data from experimentation, a qualitative analysis of gaze strategy was conducted. This indicated that for the majority of a pursuit flight, Harris's hawks use a discontinuous gaze strategy in a saccadic tracking technique which combines high frequency saccade and fixate head movements that attempt to centre the target within the region of binocular overlap of the visual field. To understand mechanisation of guidance, I then explored what sensory system outputs are available for feedback of target movement to the guidance control loop. I formulated proxies for LoS rate and deviation angle that were based on measurements available to the bird from the visual and vestibular systems. Using correlation between the true and proxy values of LoS rate and deviation angle with a spatial histogram, I found these proxies to be good approximations to the true measure. I then ran guidance simulations to assess the ability of the proxy measure to reconstruct the measured trajectories and found that the mixed guidance law best modelled the data and whilst I did not have enough data to draw statistical significance, the simulated RMS error was always lower when using proxy measures.

These results indicate that the birds may be using these head derived sensory outputs to provide target information to the guidance loop. Finally, based on new knowledge of gaze strategy and guidance modelling and using knowledge from missile guidance system architecture, I devised hypotheses in block diagram format for PN+PP and for PN guidance laws indicating how the physiological pathways that control guidance might exist in the Harris's hawk. This leaves opportunity for future studies to test these hypotheses further.

5.2 Limitations and Recommendations

In Chapter 2, I presented the development and validation of a lightweight and highly accurate GNSS-IMU biologger with wide ranging applications to the field of animal behaviour. In Chapters 3 and 4 I presented the biological experiment that saw these GNSS loggers used in the field, with two sensors logging the position of the hawk and the target. There are limitations in the sensor design of the sensor that impacted the time synchronisation between the two loggers and the quality of the head IMU data captured from the bird. Firstly, whilst the two sensors are synchronised to the nearest 100ms in GPST, there is error in the time synchronisation between the two loggers so the data reported at the same apparent time may be offset slightly leading to misalignment in trajectories. There were challenges in software design in storing data to memory that resulted in the use of a real-time-operating-system. The data storage issues were a limitation in the sample rate of the IMU, which was limited to 50 Hz, despite having the capacity to output at twice the sample rate. However, in Chapter 4, I calculated that to obtain more detailed information on the maximum yaw rate and duration of head saccades, the required IMU sample rate would have to be > 400 Hz due to the Nyquist theorem. This would require a redesign of the sensor, which ideally uses an integrated single PCB design that optimises operational reliability and with electromagnetic compatibility (EMC) considered from the initial stages. Such a redesign would be a good opportunity to improve the GNSS receiver and antenna components such that the interpolated PPK method is not required such that PPK quality satellite data is available at all times.

In the wider field, there are some issues in the deployment of this sensor for behaviour studies. The first is the issue of using this sensor on animals with a mass below 1 kg, since the overall sensor mass is approximately 50g and following the ethical limit of 5% body mass. This limits the accuracy available to measure flight in other birds such as passerines for example. To achieve true accuracy, it is necessary to conduct research in a location within 20 km of a GNSS base station. Taking the OS Net network in the United Kingdom as an example, there are 115 stations distributed throughout the country, which leaves a significant area without access to this correction data (most locations are within 75 km of a base station [102]; a distance too large for confidence in the accuracy of a PPK solution). The conclusion therefore is that centimetre level relative accuracy between a pair of receivers is the most applicable solution for this technology that would apply worldwide. This is particularly relevant for the cases where it is not possible to choose the location of data collection, dissimilar to the circumstance in this study. Additionally, the short operational duration of 35 minutes (limit on battery capacity due to mass requirements) makes it impossible at the present to use this design for applications where continual sensor data is required over many hours or days. The high current draw is due to the high data rates and bandwidth required to save the GNSS messages to enable the use of PPK, so there is possibility in the software stage to make compromises in the data recorded.

To understand the gaze strategy of the Harris's hawk, accurate orientation data from the IMU mounted to the head of the bird was required; however this presented some challenges. Firstly, there were some issues with the chosen IMU calibration procedure. This is a twofold problem that is caused by error in placement and orientation of the sensor on the bird's head; such that alignment of the IMU axes with the sagittal plane of the bird is extremely unlikely. Due to the presence of this error that must be quantified, there is a second source of error that originates from measurement error. Calibration relied on calculating the offset between the measured gaze bearing of the bird using the orientation output of the IMU and the known bearing determined by the bearing between the bird's GNSS location

and the location of a fixed GNSS receiver that the bird's attention was directed towards. A camera was placed behind the fixed GNSS antenna (desired point of fixation for the bird's gaze) and this video recording used to establish the timing of the fixation period. Another issue with this method was the bird's short period of fixation when their attention was focused in the direction of the camera. This compounded with synchronisation errors between the timecode (UTC) embedded in the video and the GPST recorded from GNSS loggers, which made identification of the exact time of fixation difficult. The likelihood that the bird was not fixating on the camera and instead an alternative background object was also a possibility that is difficult to eliminate using this setup. If this experiment were to be conducted indoors, it would be possible to first fit the IMU to the head of the bird and perform the calibration using marker-based motion camera. Marker-based motion capture allows 3D reconstruction of an object defined by a set of reflective markers and has been used in a number of studies in bird flight [122, 123]. A marker object could be constructed for use with the head IMU to enable definition of a rotation matrix to a marker set that defines the geometry of the head. Alternatively, an orthogonal set of three cameras could be used alongside image analysis to obtain the offset of the sensor on the bird's head in comparison to the three digitally defined centrelines that define the neutral pitch, roll and yaw angle of the head. The benefit of this method would be that it could be used in the field without the need for a calibrated motion capture system.

This method of calibration is reliant on the assumption that the bird's gaze direction is aligned with the sagittal plane of the head, which is valid only if the bird's eye movements are negligible. Here I suggested that the low degree of eye movement would help stabilise the image on the retina using the VOR or OKR. Previous studies on the eye movements of raptors with a fixed head report degree of eye movement to be in the range of 2-8 degrees [19]. This was done by fixing the head of the bird; a practice that is thought to increase the degree of eye movement since it is not possible for the bird to use head saccades to alter gaze direction in

this situation. A study into the eye movements of Harris's hawks during pursuit flight (without fixing the head) could inform conclusions made on gaze strategy.

In Chapter 3, guidance modelling was conducted in a similar process to that already conducted in Harris's hawks [11, 120], peregrines [10] and gyrfalcons [12]. In this modelling process using guidance laws of PP, PN and a PN+PP mixed guidance law, it was assumed that the gains of N and K are constant throughout the flight. Whilst this might be reasonable when modelling short sections of flight over 20 metres or so, it is unlikely to be the case when in a long distance pursuit.

Guidance modelling was conducted with constant gains (N and K) throughout the simulation. However, it is likely that this assumption is inaccurate and that the hawks might change gain based on target behaviour. Additionally, when visual distractions take place during flight, the birds attention is not focussed on the target. During this time, it is unlikely that the bird is performing guidance based on sensory feedback from the target. In this case, a segmented guidance fit, where different sections of the flight are fitted separately with different gains could be more appropriate. Segmented fitting might also identify a two different tuning regimes of flight defined by 'far' and 'close' distances to the target. However, it is more likely that this can be continually altered throughout the flight.

5.3 Future Work

One of the initial aims of this research was to develop a bio-inspired vision-based tracking strategy for use in aerial robotics; however due to the need to develop an accurate GNSS biologger and delays due to the COVID pandemic, further work on this was not possible within the time frame of the DPhil. The field of bio-inspired engineering aims to use concepts learned from biological systems to improve on current and develop new technology.

Whilst the hypotheses established here on the mechanisation of guidance in the hawks were formulated using knowledge from homing missile systems, it is unclear as to whether this has been applied in the field of aerial robotics; with most of the publicly available systems using simple continuous tracking strategies with the

centre of the camera FOV fixed to the target. It is also unclear whether UAV systems designed for aerial target pursuit regularly use proportional navigation or other guidance laws in practice. The first step in deploying a Harris's hawk-inspired gaze strategy is to program a UAV to intercept a target using a guidance law.

I started investigating this (in collaboration with S. Golodetz) using the smglib drone simulation framework developed by Golodetz et al [124] to control a Tello camera-equipped drone (DJI, Shenzhen, China). This framework enables algorithm development both using a 3D simulation environment and simultaneous drone control using a Vicon motion capture system for ground truth of the drone's position. Commands are applied as pitch, roll and yaw commands, but it is not possible to modify the behaviour of the proportional-integral-derivative (PID) controller that stabilises the aircraft. We began to implement some simple guidance algorithms (including PN) to intercept a chosen target with good success, but there was insufficient time to continue development. Smglib has the ability to leverage the visual output of the camera that is integrated to the drone, which would enable one to build in computer vision capability. This would be seen as the next step in the development of the hawk-inspired UAV system; integrating target information obtained via the visual system (camera) and via gyroscopes to generate guidance commands. There is opportunity to take this further to test in simulation and on hardware (closed loop using motion capture) the performance of a Harris's hawk-inspired visual guidance algorithm. This has the potential to make improvements to existing methods of pursuit tracking and interception in robotics.

With regards to the fitting of guidance laws; whilst the mixed PN+PP guidance law modelled globally for all N=54 recorded flights provided the lowest RMS error distribution when compared to PN or PP separately, the simulated trajectories do not show a convincing reproduction of the path taken by the bird for every flight (despite the low RMS error). This suggests that the models fitted to the data do not completely capture the animal's behaviour. This might be a result of the birds using these guidance laws with an alternative combination of input variables or with additional input variables. For example, the inclusion of target

acceleration as an input parameter in augmented PN or non-constant guidance parameters might lead to a better model of the bird's guidance behaviour. I began exploring this in Chapter 3; however a lack of flight data reduced the statistical power and prevented the ability to make conclusions on the results of these tests. We were also unable to establish whether Harris's hawks are able to adapt their guidance tuning to the target behaviour. More broadly, this work and others [10], [11], [12], [120] have incompletely answered how the guidance behaviour of raptors is controlled. This is potentially constrained by our model driven analytical approach, which assumes that the finite number of models chosen to fit to the data, if they fit well, describe the animal's behaviour exactly. Whilst the fitting of guidance laws provides a simple and effective approach of describing the pursuit trajectories measured in experimentation, this approach doesn't allow us to extract any more from the data other than whether one model fits better than another. This modelling approach takes inspiration from guided missiles and will not represent the mechanisms by which animals implemnent guidance; however, it adds value in the understanding of the behaviour, allowing complex trajectories to be captured across species and individuals with a few parameters.

References

[1] Michael F Land and Dan-Eric Nilsson. *Animal eyes*. OUP Oxford, 2012.

[2] Suzanne Amador Kane, Andrew H Fulton, and Lee J Rosenthal. "When hawks attack: animal-borne video studies of goshawk pursuit and prey-evasion strategies". In: *Journal of Experimental Biology* 218.2 (2015), pp. 212–222.

[3] Robert M Olberg. "Visual control of prey-capture flight in dragonflies". In: *Current opinion in neurobiology* 22.2 (2012), pp. 267–271.

[4] Kaushik Ghose et al. "Echolocating bats use a nearly time-optimal strategy to intercept prey". In: *PLoS biology* 4.5 (2006), e108.

[5] Norbert Boeddeker, Roland Kern, and Martin Egelhaaf. "Chasing a dummy target: smooth pursuit and velocity control in male blowflies". In: *Proceedings of the Royal Society of London. Series B: Biological Sciences* 270.1513 (2003), pp. 393–399.

[6] SW Zhang et al. "Visual tracking of moving targets by freely flying honeybees". In: *Visual neuroscience* 4.4 (1990), pp. 379–386.

[7] Andreas F Haselsteiner, Cole Gilbert, and Z Jane Wang. "Tiger beetles pursue prey using a proportional control law with a delay of one half-stride". In: *Journal of the Royal Society Interface* 11.95 (2014), p. 20140216.

[8] Michael F Land and Thomas S Collett. "Chasing behaviour of houseflies (Fannia canicularis)". In: *Journal of comparative physiology* 89.4 (1974), pp. 331–357.

[9] Andrew M Hein et al. "An algorithmic approach to natural behavior". In: *Current Biology* 30.11 (2020), R663–R675.

[10] Caroline H Brighton, Adrian L R Thomas, and Graham K Taylor. "Terminal attack trajectories of peregrine falcons are described by the proportional navigation guidance law of missiles". In: *Proceedings of the National Academy of Sciences of the United States of America* 114 (51 2017), pp. 13495–13500. URL: %3CGo%20to%20ISI%3E://WOS:000418321600063.

[11] Caroline H Brighton and Graham K Taylor. "Hawks steer attacks using a guidance system tuned for close pursuit of erratically manoeuvring targets". In: *Nature Communications* 10 (1 2019). URL: https://doi.org/10.1038/s41467-019-10454-z.

[12] Caroline H Brighton et al. "Attack behaviour in naive gyrfalcons is modelled by the same guidance law as in peregrine falcons, but at a lower guidance gain". In: *Journal of Experimental Biology* 224 (5 2021), jeb238493.

[13] Samuel T Fabian et al. "Interception by two predatory fly species is explained by a proportional navigation feedback controller". In: *Journal of The Royal Society Interface* 15.147 (2018), p. 20180466.

[14] Robert M Olberg et al. "Eye movements and target fixation during dragonfly prey-interception flights". In: *Journal of comparative physiology A* 193 (2007), pp. 685–693.

[15] Matteo Mischiati et al. "Internal models direct dragonfly interception steering". In: *Nature* 517.7534 (2015), pp. 333–338.

[16] Paloma T Gonzalez-Bellido et al. "Eight pairs of descending visual neurons in the dragonfly give wing motor centers accurate population vector of prey direction". In: *Proceedings of the National Academy of Sciences* 110.2 (2013), pp. 696–701.

[17] Neryahu A Shneydor. *Missile guidance and pursuit: kinematics, dynamics and control*. Elsevier, 1998.

[18] Graham R Martin. "Visual fields and their functions in birds". In: *Journal of Ornithology* 148.2 (2007), pp. 547–562.

[19] Colleen T O'Rourke et al. "Hawk eyes I: diurnal raptors differ in visual fields and degree of eye movement". In: *PloS one* 5.9 (2010), e12802.

[20] Colleen T O'Rourke et al. "Hawk eyes II: diurnal raptors differ in head movement strategies when scanning from perches". In: *PLoS One* 5.9 (2010), e12169.

[21] Josh Wallman and John D Pettigrew. "Conjugate and disjunctive saccades in two avian species with contrasting oculomotor strategies". In: *Journal of Neuroscience* 5.6 (1985), pp. 1418–1428.

[22] Simon Potier et al. "Visual abilities in two raptors with different ecology". In: *Journal of Experimental Biology* 219.17 (2016), pp. 2639–2649.

[23] Graham R Martin. "What is binocular vision for? A birds' eye view". In: *Journal of Vision* 9.11 (2009), pp. 14–14.

[24] Katherine V Fite and Sheila Rosenfield-Wessels. "A comparative study of deep avian foveas". In: *Brain, Behavior and Evolution* 12.1-2 (1975), pp. 97–115.

[25] David B Meyer. "The avian eye and its adaptations". In: *The visual system in vertebrates*. Springer, 1977, pp. 549–611.

[26] George M Siouris. *Missile guidance and control systems*. Springer Science & Business Media, 2004.

[27] James Walker. "Visual guidance of target-oriented flight behaviours in birds". PhD thesis. University of Oxford, 2018.

[28] G L Walls. "The evolutionary history of eye movements". In: *Vision Research* 2 (1-4 1962), pp. 69–80.

[29] Raymond Dodge. "Five types of eye movement in the horizontal meridian plane of the field of regard". In: *American journal of physiology-legacy content* 8.4 (1903), pp. 307–329.

[30] Do A Robinson. "The mechanics of human smooth pursuit eye movement." In: *The Journal of Physiology* 180.3 (1965), p. 569.

[31] Stephen G Lisberger, Edward Joseph Morris, and Lawrence Tychsen. "Visual motion processing and sensory-motor integration for smooth pursuit eye movements". In: *Annual review of neuroscience* 10.1 (1987), pp. 97–129.

[32] Jolande Fooken, Philipp Kreyenmeier, and Miriam Spering. "The role of eye movements in manual interception: A mini-review". In: *Vision Research* 183 (2021), pp. 81–90.

[33] Leigh A Mrotek and John F Soechting. "Target interception: hand–eye coordination and strategies". In: *Journal of Neuroscience* 27.27 (2007), pp. 7297–7309.

[34] Cristina de la Malla, Jeroen BJ Smeets, and Eli Brenner. "Potential systematic interception errors are avoided when tracking the target with one's eyes". In: *Scientific reports* 7.1 (2017), p. 10793.

[35] Jolande Fooken et al. "Eye movement accuracy determines natural interception strategies". In: *Journal of vision* 16.14 (2016), pp. 1–1.

[36] Frederic R Danion et al. "More precise tracking of horizontal than vertical target motion with both the eyes and hand". In: *Cortex* 134 (2021), pp. 30–42.

[37] AF Fuchs. "Saccadic and smooth pursuit eye movements in the monkey". In: *The Journal of physiology* 191.3 (1967), p. 609.

[38] Martha G MacAvoy, Jacqueline P Gottlieb, and Charles J Bruce. "Smooth-pursuit eye movement representation in the primate frontal eye field". In: *Cerebral Cortex* 1.1 (1991), pp. 95–102.

[39] Clara Bourrelly et al. "Learning the trajectory of a moving visual target and evolution of its tracking in the monkey". In: *Journal of Neurophysiology* 116.6 (2016), pp. 2739–2751.

[40] Norbert Boeddeker and Martin Egelhaaf. "A single control system for smooth and saccade-like pursuit in blowflies". In: *Journal of experimental biology* 208.8 (2005), pp. 1563–1572.

[41] Thomas S Collett and MF Land. "Visual control of flight behaviour in the hoverflySyritta pipiens L." In: *Journal of comparative physiology* 99.1 (1975), pp. 1–66.

[42] Huai-Ti Lin and Anthony Leonardo. "Heuristic rules underlying dragonfly prey selection and interception". In: *Current Biology* 27.8 (2017), pp. 1124–1137.

[43] Dennis Eckmeier et al. "Gaze strategy in the free flying zebra finch (Taeniopygia guttata)". In: *PLoS One* 3.12 (2008), e3956.

[44] Ivo G Ros and Andrew A Biewener. "Pigeons (C. livia) follow their head during turning flight: head stabilization underlies the visual control of flight". In: *Frontiers in neuroscience* 11 (2017), p. 655.

[45] J H V Hateren and C Schilstra. "Blowfly flight and optic flow. II. Head movements during flight". In: *Journal of Experimental Biology* 202 (11 1999), pp. 1491–1500.

[46] C Schilstra and J H Van Hateren. "Stabilizing gaze in flying blowflies". In: *Nature* 395 (6703 1998), p. 654.

[47] Vance A Tucker. "The deep fovea, sideways vision and spiral flight paths in raptors". In: *Journal of Experimental Biology* 203.24 (2000), pp. 3745–3754.

[48] Suzanne Amador Kane and Marjon Zamani. "Falcons pursue prey using visual motion cues: new perspectives from animal-borne cameras". In: *Journal of Experimental Biology* 217.2 (2014), pp. 225–234.

[49] Neil F Palumbo, Ross A Blauwkamp, and Justin M Lloyd. "Basic principles of homing guidance". In: *Johns Hopkins APL Technical Digest* 29.1 (2010), pp. 25–41.

[50] Rexford D Lord, Frank C Bellrose, and William W Cochran. "Radiotelemetry of the Respiration of a Flying Duck". In: *Science* 137 (3523 1962), pp. 39–40.

[51] Cobert D LeMunyan et al. "Design of a Miniature Radio Transmitter for Use in Animal Studies". In: *The Journal of Wildlife Management* 23 (1 1959), pp. 107–110.

[52] Sivan Toledo et al. "Lessons and experiences from the design, implementation, and deployment of a wildlife tracking system". In: *2016 IEEE International Conference on Software Science, Technology and Engineering (SWSTE)*. IEEE. 2016, pp. 51–60.

[53] Simon P Ripperger et al. "Thinking small: next-generation sensor networks close the size gap in vertebrate biologging". In: *PLoS biology* 18.4 (2020), e3000655.

[54] R Kays et al. "Tracking Animal Location and Activity with an Automated Radio Telemetry System in a Tropical Rainforest". In: *The Computer Journal* 54 (12 2011), pp. 1931–1948.

[55] "Migration and Stopover in a Small Pelagic Seabird, the Manx Shearwater Puffinus puffinus: Insights from Machine Learning". In: *Proceedings: Biological Sciences* 276 (1660 2009), pp. 1215–1223.

[56] W J Fuller et al. "Utility of geolocating light loggers for indicating at-sea movements in sea turtles." In: *Endang Species Res.* (4 2008), pp. 139–146.

[57] Roger D Hill. *Theory of geolocation by light levels*. Ed. by B J Le Boeuf and R M Laws. 1994, pp. 227–236.

[58] Adam M Fudickar, Martin Wikelski, and Jesko Partecke. "Tracking migratory songbirds: accuracy of light-level loggers (geolocators) in forest habitats". In: *Methods in Ecology and Evolution* 3 (1 2012), pp. 47–52.

[59] Tim Guilford et al. "A Dispersive Migration in the Atlantic Puffin and Its Implications for Migratory Navigation". In: *PLoS ONE* 6 (7 2011), e21336.

[60] John J Craighead et al. "Satellite Monitoring of Black Bear". In: *BioScience* 21 (24 1971), pp. 1206–1212.

[61] Collecte Localisation Satellites. *Argos User's Manual*. 2016. URL: `www.argos-system.org/wp-content/uploads/2016/08/r363_9_argos_users_manual-v1.6.6.pdf`.

[62] Mark R Fuller, William S Seegar, and Linda S Schueck. "Routes and Travel Rates of Migrating Peregrine Falcons Falco peregrinus and Swainson's Hawks Buteo swainsoni in the Western Hemisphere". In: *Journal of Avian Biology* 29 (4 1998), pp. 433–440.

[63] BJ Le Boeuf et al. "Foraging ecology of northern elephant seals". In: *Ecological monographs* 70.3 (2000), pp. 353–382.

[64] Max Planck Institute of Animal Behavior. *Icarus*. 2022. URL: `https://www.icarus.mpg.de/en`.

[65] "Biological Earth observation with animal sensors". In: *Trends in Ecology and Evolution* 37 (4 2022), pp. 293–298. URL: https://www.sciencedirect.com/science/article/pii/S0169534721003165.

[66] Navigation National Executive Committee for Space-Based Positioning and Timing. *GPS Accuracy*. 2021. URL: https://www.gps.gov/systems/gps/performance/accuracy/#sa.

[67] Novatel Inc. *An introduction to GNSS*. 2015.

[68] Arthur R Rodgers, Robert S Rempel, and Kenneth F Abraham. "A GPS-Based Telemetry System". In: *Wildlife Society Bulletin (1973-2006)* 24 (3 1996), pp. 559–566. URL: http://ezproxy-prd.bodleian.ox.ac.uk:2154/stable/3783345.

[69] Max Planck Institute of Animal Behavior. *Movebank*. 2022. URL: https://www.movebank.org/cms/movebank-main.

[70] Ariana Strandburg-Peshkin et al. "Shared decision-making drives collective movement in wild baboons". In: *Science* 348.6241 (2015), pp. 1358–1361.

[71] Oliver Padget et al. "Shearwaters know the direction and distance home but fail to encode intervening obstacles after free-ranging foraging trips". In: *Proceedings of the National Academy of Sciences* 116.43 (2019), pp. 21629–21633.

[72] Deane Bunce. "Wide area augmentation system (WAAS) status and history". In: ed. by F A A. 2014. URL: https://www.gps.gov/multimedia/presentations/2014/09/ION/bunce.pdf.

[73] European Global Navigation Satellite Systems Agency. *EGNOS Open Service (OS) Service Definition Document,* 2.3, 2017. URL: https://egnos-user-support.essp-sas.eu/new_egnos_ops/documents/egnos-sdd/egnos-open-service-sdd.

[74] US Department of Defense. "Global positioning system standard positioning service performance standard". In: (2020). URL: https://www.gps.gov/technical/ps/2020-SPS-performance-standard.pdf.

[75] European Global Navigation Satellite Systems Agency. *EGNOS Open Service (OS) Service Definition Document,* 2.3, 2017. URL: https://egnos-user-support.essp-sas.eu/new_egnos_ops/documents/egnos-sdd/egnos-open-service-sdd.

[76] Amedeo Rodi Vetrella et al. "Multi-UAV Carrier Phase Differential GPS and Vision-based Sensing for High Accuracy Attitude Estimation". In: *Journal of Intelligent and Robotic Systems* 93 (1-2 2019), pp. 245–260.

[77] Julián Tomaštík et al. "UAV RTK/PPK Method—An Optimal Solution for Mapping Inaccessible Forested Areas?" In: *Remote Sensing* 11 (6 2019), p. 721. URL: https://www.mdpi.com/2072-4292/11/6/721/pdf.

[78] B Richard. Langley. "RTK GPS". In: *GPS World* (1998).

[79] Johannes Traugott. "Precise flight trajectory reconstruction based on time-differential GNSS carrier phase processing". PhD thesis. Technische Universität München, 2011.

[80] G Sachs. "In-flight measurement of upwind dynamic soaring in albatrosses". In: *Progress in Oceanography* 142 (2016), pp. 47–57. URL: %3CGo%20to%20ISI%3E://WOS:000373863800004.

[81] G Sachs et al. "Experimental verification of dynamic soaring in albatrosses". In: *Journal of Experimental Biology* 216 (22 2013), pp. 4222–4232. URL: http://jeb.biologists.org/content/216/22/4222.full.pdf.

[82] Gottfried Sachs et al. "Flying at No Mechanical Energy Cost: Disclosing the Secret of Wandering Albatrosses". In: *PLoS ONE* 7 (9 2012), e41449. URL: https://journals.plos.org/plosone/article/file?id=10.1371/journal.pone.0041449&type=printable.

[83] Hamed Haddadi et al. "Determining association networks in social animals: choosing spatial–temporal criteria and sampling rates". In: *Behavioral Ecology and Sociobiology* 65 (8 2011), pp. 1659–1668. URL: http://ezproxy-prd.bodleian.ox.ac.uk:2154/stable/41414626.

[84] Andrew J King et al. "Selfish-herd behaviour of sheep under threat". In: *Current Biology* 22 (14 2012), R561–R562. URL: https://www.sciencedirect.com/science/article/pii/S0960982212005295.

[85] James R Usherwood et al. "Flying in a flock comes at a cost in pigeons". In: *Nature* 474 (7352 2011), pp. 494–497. URL: http://europepmc.org/articles/pmc3162477?pdf=render.

[86] Steven J Portugal et al. "Upwash exploitation and downwash avoidance by flap phasing in ibis formation flight". In: *Nature* 505 (7483 2014), pp. 399–402. URL: https://researchonline.rvc.ac.uk/8076/1/8076.pdf.

[87] A M Wilson et al. "Locomotion dynamics of hunting in wild cheetahs". In: *Nature* 498 (7453 2013), pp. 185–189.

[88] Alan M Wilson et al. "Biomechanics of predator–prey arms race in lion, zebra, cheetah and impala". In: *Nature* 554 (7691 2018), pp. 183–188. URL: https://researchonline.rvc.ac.uk/11143/1/11143.pdf.

[89] Hattie Bartlam-Brooks et al. "There and back again - a zebra's tale". In: *Journal of Experimental Biology* 223 (23 2020), jeb232140.

[90] Tatjana Y Hubel et al. "Movement patterns and athletic performance of leopards in the Okavango Delta". In: *Proceedings of the Royal Society B: Biological Sciences* 285 (1877 2018), p. 20172622.

[91] Oliver P Dewhirst et al. "Improving the accuracy of estimates of animal path and travel distance using GPS drift-corrected dead reckoning". In: *Ecology and Evolution* 6 (17 2016), pp. 6210–6222. URL: https://onlinelibrary.wiley.com/doi/pdf/10.1002/ece3.2359.

[92] Monica A Daley et al. "Preferred gait and walk–run transition speeds in ostriches measured using GPS-IMU sensors". In: *Journal of Experimental Biology* 219 (20 2016), pp. 3301–3308. URL: http://jeb.biologists.org/content/219/20/3301.full.pdf.

[93] Hamideh Keshavarzi et al. "Validation of Real-Time Kinematic (RTK) Devices on Sheep to Detect Grazing Movement Leaders and Social Networks in Merino Ewes". In: *Sensors* 21 (3 2021), p. 924.

[94] Tomoji Takasu. *RTKLIB: An Open Source Program Package for GNSS Positioning*. URL: https://www.rtklib.com. (accessed: 19.12.2022).

[95] u-Blox. *ZED-F9P Integration manual*. R08. 2020. URL: https://www.u-blox.com/en/product/zed-f9p-module#tab-documentation-resources.

[96] Vaughan Pratt. "Direct least-squares fitting of algebraic surfaces". In: *SIGGRAPH Comput. Graph.* 21 (4 1987), pp. 145–152. URL: https://ezproxy-prd.bodleian.ox.ac.uk:2102/10.1145/37402.37420.

[97] Nikolai Chernov. *Circle Fit (Pratt Method)*. 2022. URL: https://uk.mathworks.com/matlabcentral/fileexchange/22643-circle-fit-pratt-method.

[98] Bosch Sensortec. *BNO055 Datasheet*. 1.8. 2021. URL: https://www.bosch-sensortec.com/media/boschsensortec/downloads/datasheets/bst-bno055-ds000.pdf.

[99] *ZED-F9P Datasheet*. UBX-21044850. u-Blox. May 2022.

[100] Bednarz JC Dwyer JF. "Birds of the world". In: 1.0. Cornell Lab of Ornithology, Ithaca, NY, USA, 2020. Chap. Harris' Hawk (Parabuteo unicinctus).

[101] rtklibexplorer. *RTKLIB demo5*. 2022. URL: https://github.com/rtklibexplorer/RTKLIB/releases. (accessed: 19.12.2022).

[102] Ordnance Survey. *OS Net RINEX Data*. 2022. URL: https://www.ordnancesurvey.co.uk/gps/os-net-rinex-data/. (accessed: 19.12.2022).

[103] Network EPG. *ETRF/ITRF Coordinate Transformation Tool (ECTT)*. 2022. URL: https://www.epncb.oma.be/_productsservices/coord_trans/. (accessed: 19.12.2022).

[104] UNAVCO. *Plate motion calculator*. 2022. URL: https://www.unavco.org/software/geodetic-utilities/plate-motion-calculator/plate-motion-calculator.html. (accessed: 19.12.2022).

[105] Haleh Fotowat et al. "A novel neuronal pathway for visually guided escape in Drosophila melanogaster". In: *Journal of neurophysiology* 102.2 (2009), pp. 875–885.

[106] Andrei Sourakov. "Faster than a flash: the fastest visual startle reflex response is found in a long-legged fly, Condylostylus sp.(Dolichopodidae)". In: *The Florida Entomologist* 94.2 (2011), pp. 367–369.

[107] Christopher L Stitt et al. "Modification of the pigeon's visual startle reaction by the sensory environment." In: *Journal of comparative and physiological psychology* 90.7 (1976), p. 601.

[108] Harold Pomeroy and Frank Heppner. "Laboratory determination of startle reaction time of the starling (Sturnus vulgaris)". In: *Animal Behaviour* 25 (1977), pp. 720–725.

[109] Daniel Kress, Evelien Van Bokhorst, and David Lentink. "How lovebirds maneuver rapidly using super-fast head saccades and image feature stabilization". In: *PLoS ONE* 10 (6 2015), e0129287.

[110] Fumihiro Kano et al. “Head-mounted sensors reveal visual attention of free-flying homing pigeons”. In: *Journal of Experimental Biology* 221 (17 2018).

[111] Michael F Land. “Motion and vision: why animals move their eyes”. In: *Journal of Comparative Physiology A* 185 (4 1999), pp. 341–352.

[112] Michael Land. “Eye movements in man and other animals”. In: *Vision Research* 162 (2019), pp. 1–7.

[113] Vance A Tucker et al. “Curved flight paths and sideways vision in peregrine falcons (Falco peregrinus)”. In: *Journal of Experimental Biology* 203 (24 2000), pp. 3755–3763.

[114] Mees Muller. “Mechanical aspects of the semicircular ducts in the vestibular system”. In: *Biological Cybernetics* 114 (4 2020), pp. 421–442.

[115] Hans Straka et al. “Vestibulo-ocular signal transformation in frequency-tuned channels”. In: *Annals of the New York Academy of Sciences* 1164.1 (2009), pp. 37–44.

[116] William M Connelly et al. “The thalamus as a low pass filter: filtering at the cellular level does not equate with filtering at the network level”. In: *Frontiers in neural circuits* 9 (2016), p. 89.

[117] Ben J Hardcastle and Holger G Krapp. “Evolution of biological image stabilization”. In: *Current Biology* 26 (20 2016), R1010–R1021.

[118] Kikuro Fukushima et al. “Cognitive processes involved in smooth pursuit eye movements: behavioral evidence, neural substrate and clinical correlation”. In: *Frontiers in systems neuroscience* 7 (2013), p. 4.

[119] Shane P Windsor and Graham K Taylor. “Head movements quadruple the range of speeds encoded by the insect motion vision system in hawkmoths”. In: *Proceedings of the Royal Society B: Biological Sciences* 284 (1864 2017), p. 20171622.

[120] James Kempton. “The dynamic flight behaviour of birds in different frames of reference”. PhD thesis. University of Oxford, 2022.

[121] Robin Mills et al. “Physics-based simulations of aerial attacks by peregrine falcons reveal that stooping at high speed maximizes catch success against agile prey”. In: *PLoS Computational Biology* 14 (4 2018), e1006044.

[122] Marco KleinHeerenbrink et al. “Optimization of avian perching manoeuvres”. In: *Nature* 607.7917 (2022), pp. 91–96.

[123] Sofia Miñano. “Visually guided flight in Harris’ hawks: a computer vision approach”. PhD thesis. University of Oxford, 2022.

[124] Stuart Golodetz et al. “Real-Time Hybrid Mapping of Populated Indoor Scenes using a Low-Cost Monocular UAV”. In: *IEEE/RSJ International Conference on Intelligent Robots and Systems (IROS)*. Oct. 2022.

[125] US Coast Guard. *Navstar GPS user equipment introduction*. 1996. URL: `https://www.hsdl.org/?abstract&did=22298`.

[126] Elliott D Kaplan et al. *Understanding GPS: principles and applications*. 2nd. Artech House, 2006.

[127] B Bidikar et al. "Satellite Clock Error and Orbital Solution Error Estimation for Precise Navigation Applications". In: *Positioning* 5 (1 2014), pp. 22–26.

[128] European Space Agency. *Galileo and GPS 'synchronise watches': new time offset helps working together*. 2013. URL: https://www.esa.int/Applications/Navigation/Galileo_and_GPS_synchronise_watches_new_time_offset_helps_working_together.

[129] G M V. *Delay Lock Loop (DLL)*. Ed. by GMV. 2011. URL: https://gssc.esa.int/navipedia/index.php/Delay_Lock_Loop_(DLL).

[130] J Sanz Subirana, J M Juan Zornoza, and M Hernandez-Pajares. *GPS Navigation Message*. 2011. URL: https://gssc.esa.int/navipedia/index.php/GPS_Navigation_Message.

[131] van Diggelen Frank. "GPS accuracy: Lies, damn lies and statistics". In: (1998). URL: https://www.gpsworld.com/gps-accuracy-lies-damn-lies-and-statistics/%20https://www.gpsworld.com/gpsgnss-accuracy-lies-damn-lies-and-statistics-1134/.

[132] Jean-Marie. Zogg. *GPS: Essentials of Satellite Navigation,* 2009.

[133] European Union Agency for the Space Programme. *What is SBAS?* 2021. URL: https://www.euspa.europa.eu/european-space/eu-space-programme/what-sbas.

[134] Peter. Joosten and Tiberiusm Christian. "Fixing the Ambiguities: Are you sure they're right?" In: *GPS World* (May 2000 2000). URL: http://www2.unb.ca/gge/Resources/gpsworld.may00.pdf.

[135] Oxford Technical Solutions Ltd. *What is RTK?* 2020. URL: https://www.oxts.com/rtk/.

[136] Battery University. *Is lithium-ion the ideal battery?,* 2016. URL: https://batteryuniversity.com/article/is-lithium-ion-the-ideal-battery.

[137] National Geodetic Survey. *The NOAA CORS Network (NCN)*. 2022. URL: https://geodesy.noaa.gov/CORS/.

[138] European Plate Observing System. *EPOS GNSS Data Gateway,* 2022. URL: https://gnssdata-epos.oca.eu/#/site.

[139] u-Blox. *ZED-F9P Interface Description*. R08. 2020. URL: https://www.u-blox.com/en/product/zed-f9p-module#tab-documentation-resources.

[140] Angelo Joseph. "GNSS Solutions: Measuring GNSS Signal Strength". In: *Inside GNSS* (2010), pp. 20–25. URL: https://insidegnss.com/wp-content/uploads/2018/01/novdec10-Solutions.pdf.

[141] u-Blox. *GNSS antennas: RF design considerations for u-blox GNSS receivers*. R03. 2019. URL: https://www.u-blox.com/sites/default/files/products/documents/GNSS-Antennas_AppNote_%28UBX-15030289%29.pdf.

[142] Renesas Electronics. *General RTOS Concepts,* 2010. URL: https://www.renesas.com/eu/en/document/apn/general-rtos-concepts?language=en.

Appendices

A

Supplementary for Chapter 2 - Developing a High Accuracy, High Precision GNSS Biologger

A.1 Supplementary Text: A GNSS Primer

This section begins with an introduction to the GNSS system and basic code positioning. It then progresses to introduce the errors that affect GNSS solutions and the methods that are available to reduce or mitigate these. An assessment of GNSS accuracy follows with a summary of the limitations of many current GNSS biologgers. This presents the rationale behind the GNSS biologger developed in this paper.

A.1.1 System Overview

A GNSS system describes any constellation of global positioning satellites and their supporting ground network that provide geospatial positioning to the user. Available GNSS systems that provide global coverage are GPS (USA), Galileo (Europe), GLONASS (Russia) and BeiDou (China) [67].

The GNSS system comprises of space, control and user segments. The space segment is the constellation of satellites in orbit. Each satellite broadcasts ranging and navigation signals for positioning. In the control segment, a global network of monitor ground stations and a master control station maintain the satellites and ensure proper function. Satellite signals are analysed to control station-keeping manoeuvres and satellite navigation messages are updated, to be transmitted to the user by the satellite [67, 125]. The user segment consists of the GNSS receiver equipment that processes the received signals to generate a position, velocity, time (PVT) solution.

The constellation of satellites transmits data to the user segment on the same frequency bands. This is possible due to the use of the code division multiple access

(CDMA) transmission scheme; where signals are modulated by a pseudorandom noise (PRN) code unique to each satellite; ensuring that each satellite is individually identifiable [126]. It is the norm for satellites to transmit signals across two frequencies; however, provision for three is becoming more common as new satellites are put into orbit with this capability. Using GPS as an example, ranging data is transmitted on two codes which contain two frequencies known as Link 1 (L1) and Link 2 (L2), which occupy the 1575MHz and 1227MHz bands. Galileo, GLONASS and BeiDou emit ranging signals on similar frequencies to GPS [67].

A.1.2 GNSS Code Positioning

Code positioning (without augmentation) is the most basic in GNSS positioning techniques. To determine user position, GNSS systems use the distance from multiple satellites to localise the receiver on Earth. Distance is determined by measuring the propagation time for a ranging signal transmitted by a satellite (antenna) to when it is received at the receiver antenna on Earth using the signal speed (speed of light). With knowledge of the distance to multiple emitters, satellite location in orbit (from ephemerides) and other correction factors, the 3D position of the receiver can be determined.

A precise measure of time is required in the system to enable distance to be measured. Satellites use very precise, stable atomic clocks to maintain internal time. Due to their size and weight, it is not possible to use these in GNSS receivers and so these operate using a far less precise temperature compensated crystal oscillator, which provides a 1KHz local reference clock signal [95].

Each constellation operates on a distinct system time; defined by the control segment, which is coordinated for all satellites (e.g. GPS Time (GPST), Galileo System Time (GST)). Satellite atomic clocks are not perfectly synchronised to the system time and therefore the transmitted signals contain clock errors. These errors are monitored by the constellation control segment, which transmits clock error parameters to the satellite to be broadcast via the navigation message for correction by user receivers [127]. GNSS receiver clocks are also not synchronised and so have an offset to system time that needs to be determined. There are offsets between the system time for each constellation; for example, GPST and GST are around 50ns apart [128]. The GNSS receiver usually coordinates the solution to a common time such as coordinated universal time (UTC).

Receivers use signal tracking loops to determine propagation time. Delay-locked loops (DLL) measure the time delay between the incoming signal code and a PRN code replica for each satellite signal using correlation [129]. The replica code is time shifted until the correlation between this and the incoming signal is maximised. The shift and embedded transmit time are used to determine the propagation time of the transmission. Due to the non-synchronized clocks, the calculated range is subject to three components of time delay; (i) the propagation time from satellite to user; (ii) offset of receiver clock from system time; (iii) offset of satellite atomic clock from system time. For this reason, it is known as the pseudorange [126].

To determine 3D position, the pseudoranges from 4 satellites are required, to account for the clock errors in the system/signal chain. Multi-constellation receivers require a minimum of 5 satellites (with at least one in another constellation)

such that the inter-constellation system time difference can be determined [67]. Information from the navigation message is also required; such as: ephemeris, clock corrections, satellite health data, the ionospheric delay model and coefficients for calculating UTC [125, 130]. Using this and the pseudorange measurements, the user position can be determined using a system of equations to solve for the four unknowns of X,Y,Z position and clock bias/offset. Measurement error can be further reduced by increasing the number of satellite fixes.

A.1.3 GNSS Error Sources and Techniques to Improve Position Accuracy

GNSS 2D horizontal position accuracy is commonly measured in circular error probable (CEP), which is determined directly from the position error distribution. CEP 50% defines the radius of the circle where 50% of measured points fall [131] and from this point forward, CEP will denote the 50% probability threshold.

GNSS systems are subject to several error sources that affect the accuracy of the position solution with the primary sources being receiver and satellite clock uncertainty, atmospheric error (tropospheric and ionospheric delay), satellite position (ephemeris), multipath (signal blockage and reflection), satellite geometry (dilution of precision), relativistic effects and receiver and antenna hardware [66]. There are a range of techniques that can be used to mitigate the effects of these error sources to improve horizontal position accuracy.

Code positioning is the least accurate positioning technique since it does not address any of the errors mentioned above. Typically a receiver using GPS code positioning, which is known as the standard positioning service (SPS) will achieve the specified user PVT accuracy of 3.3m CEP horizontal error and 5.7m vertical error CEP [74]. It should be noted that GNSS device specifications quote static accuracy figures and do not necessarily represent dynamic accuracy. By using techniques that account for these errors, it is possible to achieve a position accuracy of 1.5m CEP using Satellite-Based Augmentation Systems (SBAS) or at centimetre level using carrier phase differential methods, such as Post-Processed Kinematic (PPK) and Real Time Kinematic (RTK). Additionally, the use of multi-frequency and multi-constellation data is beneficial to achieving optimal error resolution in positioning [67].

Multi-Frequency and Multi-Constellation

The benefit of multi-frequency data is the ability to estimate and eliminate ionospheric delay. The ionosphere slows signal propagation below the speed of light; adding an additional time delay component, which affects the calculated receiver position [132]. As the effect of ionospheric delay on code and carrier phase measurements is frequency dependent, it can be eliminated using dual frequency measurements [126]. This is known as ionosphere-free combination. Single frequency receivers use the ionospheric delay model transmitted as part of the navigation message, which is less effective in removing error. Using dual frequency measurements also provides some immunity to RF interference, since either L1 or L2 can be used in the case that interference is present in either frequency band.

Receivers capable of multi-constellation measurements can track many more of the satellites in view when compared to their single constellation counterparts. This enables improved position and time accuracy, reduced signal acquisition time, reduced effects of multipath and improved satellite geometry in the sky (reduced PDOP) [67].

SBAS (EGNOS, WAAS, MSAS, SDCM)

Pseudorange code positioning accuracy can be improved by using differential corrections from regional Satellite-Based Augmentation Systems (SBAS). These satellite systems improve the accuracy, integrity and availability of GNSS signals [133]. SBAS consists of a space segment of geostationary satellites and a ground segment of monitor and control stations. The ground segment determines ionospheric error corrections and corrections for ephemerides and satellite clocks. It broadcasts this as a navigation message, which provides a more accurate and localised set of correction information when compared to the standard navigation message [132]. A modern receiver using SBAS correction has an achievable accuracy of around 1.4m CEP [73]. EGNOS, WAAS, MSAS, SDCM are the main regional SBAS systems around the world.

PPK and RTK

PPK and RTK are both carrier phase differential methods that perform corrections to raw pseudorange, carrier phase and Doppler GNSS data. As in code positioning, propagation delay and satellite to user range (pseudorange) need to be determined. In this case, this is done with higher precision through measurement of the integer carrier phase cycles of the incoming signal, which is possible because the carrier has much higher frequency than that of the PRN code. This enables a more precise wavelength measurement (in order of millimetres). The inter-cycle measurements are very precise; however, the total number of wavelengths (elapsed over the transmission) that form the range is ambiguous, giving rise to carrier phase integer ambiguity [67]. To solve ambiguity, a double differencing algorithm is used alongside a pair of GNSS receivers; a moving rover and a static base station. This can reduce or eliminate common errors between the two receivers such as clock, satellite ephemeris and atmospheric errors. Once the integer ambiguities are known, the corresponding carrier phase measurements act as if they are high precision pseudorange measurements and allow receiver position to be calculated with comparable precision [134]. This method outputs position in two solution types: fixed and float. A fixed solution outputs the highest accuracy up to 0.01m. If ambiguities cannot be solved with the input data, the solution is known as a float, where position accuracy is in the decimetre region; approximately 0.2-0.4m [135].

The difference between PPK and RTK is in the time at which these corrections are made. Both require a pair of receivers capable of accessing raw satellite messages: a base station of known location and the user receiver. The difference is that whilst PPK corrections are done after the data is recorded using post processing software, RTK systems require an input feed of correction messages from a base station to the rover in real time to calculate the solution. One of the primary disadvantages of this over PPK is that a constant connection is required between the base station and the rover and so, if this is lost, it will not be possible to correct the position solution. This also comes with a mass penalty on the animal-mounted sensor due to the additional communications equipment required.

A.1.4 Reference Coordinate System

Typically, receivers resolve position in a chosen coordinate datum; with WGS84 being the worldwide accepted default and the one that is used by GPS satellites. If the coordinate were to be plotted on a map, translation to a local coordinate datum may be required. For example, the European Terrestrial Reference System 1989 (ETRS89), a coordinate datum unaffected by tectonic plate shift is used for mapping in the UK. If a differential correction is used (i.e. PPK), the coordinate system of the post processed position solution is the same as that of the reference station used.

A.2 Supplementary Methods

A.2.1 Sensor Design Specifications

This sensor was designed to record short duration flight trajectories with high accuracy (centimetre level) GNSS using PPK and at high data rates of at least 10Hz. This accuracy requirement was essential for this experiment because determination of the relative position and direction between two receivers at close range was very unreliable using standard SBAS GPS receivers with accuracy at metre level (CEP). PPK was the chosen processing method to ensure this accuracy requirement was met. An operational duration of 30 minutes was chosen. For this experiment, it was possible to change batteries frequently and retrieve the data after each day of data collection. For this reason, it was not necessary for this logger to be optimised for very low power operation, as the battery duration was sufficient for the experimental requirements. The sensor was also designed to meet typical environmental requirements such as vibration, moisture and weight constraints imposed by the study species.

A.2.2 Component Choices

To make a PPK GNSS logger, the following components are required: GNSS receiver, GNSS antenna, microprocessor, flash storage and card reader, battery and optionally inertial measurement units can be incorporated. The rationale behind the specific chosen components of each category is mentioned in the following sections.

GNSS Receiver

The u-Blox ZED-F9P is available for consumers in small PCB breakout board format from Sparkfun, USA with accessible pinouts. This board requires sourcing a separate antenna as discussed below in 3.3.2. This sensor can access dual frequency bands for all satellite constellations with a suitably chosen antenna. When using all satellite constellations, this receiver can sample at a maximum of 20Hz when recording RAW data (raw satellite data used for PPK correction) only and a maximum of 10Hz when recording the PVT solution. Higher data rates up to 25Hz for both solution types are possible if reducing the number of constellations to GPS+GLONASS for example. Making use of these higher rates may be desirable if the reference base station service does not provide all constellations in their correction file, since data from the other constellations will not be used in the solution.

Antenna

Correct antenna choice is essential in being able to collect data of sufficient quality from the PPK enabled GNSS receiver. Biologging applications are limited by the weight of the device; however, for successful implementation of this technology, the antenna may become a large proportion of the device mass.

To determine the antenna required for this device, Section 4.4 of the ZED-F9P receiver integration manual [95] was first consulted. For this receiver, an active antenna is required as only these have high enough gain for satellite tracking. This also gave values for each requirement of: antenna gain (band differentiation between L1 & L2/E5b), polarisation, axial ratio, phase centre variation and group delay variation in-band. With these requirements, it is possible to correspond these to RTK suitable antenna datasheets from manufacturers to shortlist viable options.

There are two main feasible active antenna types for this receiver that have sufficient gain: the first being a patch antenna and secondly a helical antenna. These differ in their physical construction and operational characteristics. Antennas have different radiation patterns which differ mostly on their type. This determines the receive/transmit gain for different directions of the oncoming signal incident to the antenna's nominal axis.

Patch antennas are usually designed to be highly directional and so have highest gain directly above the antenna; decreasing for the regions away from the vertical. This means that it is best oriented always facing towards the sky. These require ground planes to increase the gain (and help reduce multipath reflections from below). There is a compromise between the optimal ground plane size for maximising gain and minimising axial ratio. Axial ratio is a measure of the polarisation of the antenna and the ideal circular polarisation has a value of 1dB, which is same the polarisation scheme for the emitted signals from the satellite; meaning that no polarisation loss will be incurred. Generally, a 25x25mm patch antenna is recommended and the optimal ground plane size is approximately 50x50mm to 70x70mm, which can be made from a thin sheet metal or PCB. When choosing a patch antenna, this is an additional weight penalty to consider.

In a free space configuration (no ground plane), a helical antenna has an omni-directional radiation pattern and so is tolerant to a larger range of orientation angles when compared to a patch. These antennas also are generally of a lower mass, but with larger dimensions than a comparable patch antenna. Without an antenna ground plane, any ground planes within 5mm of the antenna (including PCBs) can affect performance and impairment of the radiation pattern [95].

Antennas are available in internal and external types. External antennas are tuned to their enclosure, whereas internal antennas are designed to be integrated into a PCB containing multiple components including the GNSS receiver. Typically, external antennas will use more robust signal connectors (such as SMA), which is ideal for prototyping. Internal antennas use press fit U.FL (and other compatible) connectors which have a design suited to only a few connect-disconnect cycles. Through proper testing, it is possible to successfully use an internal antenna in a design, where consideration has been made to placement and Electromagnetic Compatibility (EMC), which is discussed in SI Section 4.6.

In this study, ethical weight constraints limited the bird mounted sensor antenna choice to single band (L1) multi-constellation GNSS only. The two viable antennas

chosen were: the ADFGP.25A.07.0060A internal active patch antenna (Taoglas Ltd, Ireland) and the BT-103 external helical antenna (Shenzhen Beitian Communication Co, China). Due to optimal dynamic performance, the BT-103 antenna was chosen from the data collected in Section 4.

For the base station and radio-controlled car target, the ANN-MB-00 dual band (L1/L2) external patch antenna (u-Blox, Switzerland) was chosen, which gave consistent performance, and the low-profile form factor was ideal for use on the car target.

Inertial Measurement Unit

The BNO055 (Bosch Sensortec, Germany) absolute orientation sensor was chosen for this application; with one internally integrated to measure body orientation and an external IMU for head orientation estimation both running at 50Hz. This is a 9 axis IMU (gyroscope, accelerometer, magnetometer) with built in sensor fusion for orientation estimation with sample rates up to 100Hz. This provides an orientation solution in addition to all the raw sensor measurements. The breakout board from Pesky Products, USA is the smallest BNO055 that could be found at the time of manufacture. This also includes a BMP280 pressure sensor (Bosch, Germany) that could be used in altitude determination. IMU communication was performed using I2C.

Processor

A Teensy 4.0 (PJRC, USA) was the chosen microcontroller because of its wide range of I/O and high clock speeds. This was required to handle the large amounts of data throughput in this design. It is possible to lower the clock speed and reduce power usage on this device, making it very flexible.

Battery

Lithium batteries have the highest energy densities available (lithium polymer is lower energy density than lithium-ion; however, the polymer electrolyte in these batteries allows them to be manufactured with lightweight packaging rather than the metal shell of Li-ion [136]). Lithium polymer batteries were chosen due to their high discharge current and the availability of very low capacities (150mAh) in small, lightweight packages. 150mAh, 25C discharge (3.75A max) LiPos (E-Flite, USA) provided over 30-minute run times with a mass of 5g.

Data Storage

MicroSD data storage was used in conjunction with the external Breakout Board for microSD Card (Polulu, USA) that communicates over SPI (Serial Peripheral Interface). The MicroSD card chosen was of an SLC (single-level cell) variant due to their high write speed performance.

A.2.3 Base Station Reference Networks

To enable accurate PPK correction, the GNSS data from a reference base station (of known accurate geodetic coordinates) is required. These stations are usually part of a service supporting a larger network of base stations in a country; for example in the UK, this is called OS Net and is provided by the Ordnance Survey (OS) [102]. The equivalent in the US is called CORS (Continuously Operating Reference Stations) and are provided by the National Geodetic Survey (NGS) of the National Oceanographic and Atmospheric Administration (NOAA) [137]. European data are available from the European Plate Observing System (EPOS) GNSS Data Gateway [138]. Essentially, these reference stations consist of a GNSS receiver and antenna in a fixed location and the services provide the raw GNSS data download from these stations for use in correcting user GNSS measurements.

For PPK, it is necessary that this base station location is within 20km (baseline distance) for the best performance. As the base station to rover distance increases, reduction of atmospheric errors with double differencing becomes less effective. Both receivers need to view the same satellites concurrently and be as close as possible for the most optimal atmospheric error correction.

Base station reference networks offer a standard solution file in RINEX (Receiver INdependent EXchange) format, which is also the common format for post processing personal data. For OS Net, the standard solution contains GPS, GLONASS, GALILEO and BeiDou constellations across dual frequencies. If the local reference network does not provide all constellations from their GNSS products or if the baseline distance to the experimental location is far, it may be useful to use a personal base station to improve the solution quality of a dynamic rover receiver. The location of the personal base station can be accurately determined using the reference base network solution. PPK solution results are more accurate for static data, as the receiver is less likely to exhibit losses in satellite reception; known as cycle slips, compared to when a receiver is in unsteady dynamic motion. In this case, multi-constellation data captured by a personal base station for which its precise location has been resolved may help provide a more reliable PPK solution for a dynamic rover. However, it should be noted that the absolute accuracy of the rover correction can only ever be as accurate as the estimated personal base position and the quality of the rover and base observations [67].

A.2.4 GNSS Messages and ZED-F9P Configuration using u-Center

For SBAS trajectory data analysis, the most important GNSS output is the PVT (position, velocity, time) data. For PPK trajectory analysis using post processing, additional raw measurement and navigation messages are required.

Typically, consumer level GNSS receivers utilise NMEA message format as the main data output from satellite navigation modules. The u-blox receivers that are being used in this application also communicate via their proprietary message format; UBX and this format has been used for this project because it also supports the raw messages required to enable PPK post processing.

The UBX message protocol uses 8-bit binary data, is checksum protected and uses a 2-stage message identifier [139]. The UBX messages of interest are listed below:

1. UBX-NAV-PVT: This is the navigation position velocity time solution and includes all necessary GNSS information for trajectory analysis.

2. UBX-RXM-RAWX: This is the multi-GNSS raw measurement data message, which contains all necessary information to create a RINEX 3 observation file used in post processing. The data contained in this message is: pseudorange, Doppler, carrier phase, phase lock and signal quality information for GNSS satellites once signals have been synchronized.

3. UBX-RXM-SFRBX: This is the broadcast navigation data subframe message. This message reports a complete subframe of broadcast navigation data decoded from a single signal and is essential for post processing the raw message.

u-Blox GNSS receivers can be configured via USB using the u-Blox u-center application. Access to all constellations and SBAS satellites was configured, with a data rate of 10Hz. For the bird-mounted loggers only L1 frequencies were enabled due to the antenna choice. For the base station and car target loggers, dual frequency measurements were enabled for all constellations. The required messages to store to memory must be enabled (as listed above). The monitor RF Information message (UBX-MON-RF) was also enabled to monitor RF noise and interference of the satellite reception. The dynamic Kalman profile was set to the Airborne 4g setting as a reasonable upper boundary to the types of motion seen during experimentation. The serial port was set up to communicate at 234600 baud. The amount of data sent from the ZED-F9P when raw messages are enabled is far greater than when using PVT only and this baud speed was selected through manual testing. Output messages from ports other than serial Tx and USB were disabled, since overloading the system can prevent any data from being transmitted. The u-center software can also be used to update the receiver firmware.

A.2.5 Electromagnetic Compatibility

Received satellite signal quality can be degraded by emitted electromagnetic interference (EMI) from other components in the system and from the environment. Typically, with the compact nature of these loggers, direct noise emission from other electronic sensor components is the primary contributor to EMI in this application. The RF noise emitted from system components will occur as direct in-band frequencies (in L1/L2 bands) that directly interfere with the antenna and GNSS receiver. Additionally, this emitted RF noise can be induced back into the system through unshielded signal wires and PCBs in a process known as coupling. Additionally, antennas can become detuned based on the electrical and physical environment in which they are situated, which reduces the sensitivity to frequencies of interest and reduces the carrier to noise ratio [140].

Through testing, it was clear that the writing to the SD card was a major source of emitted radiation. The processor was also run at 600MHz, which is approximately half of the L1 GPS frequency; hence harmonics of this could have been a source. Without implementing countermeasures, the receiver was not able to maintain a good lock onto satellites. Performance and noise were assessed using the PVT solution and RF Information monitor messages in the u-center application.

The primary methods used to mitigate the impact of EMI concern antenna placement, power and ground planes, decoupling capacitors and shielding. The first consideration when designing component layout would be to use an external antenna placed as far away from other electronic components as possible. When small animals are a target species, it is not possible for this to be a large distance. To mitigate for any noise or coupled noise on the power and signal lines, 10nF decoupling capacitors were applied to the 5V power lines on the teensy and across the serial output of the GNSS receiver. To ensure that there were no ground loops, all ground connections were made to and from the Teensy MCU ground pads. Ferrite beads were also applied to the signal line and to the antenna cable to the patch antenna (not required for the helical antenna) to increase the impedance and reduce high frequency voltage fluctuations. The processor, SD card reader and body mounted IMU were placed in a shielded box to isolate emitted radiation from the GNSS receiver and antenna. This was shielded using tin plated copper tape The box and its lid were also grounded to ensure that there was a common ground between all components [141].

After implementing these changes, the effect of EMI on GNSS performance was minimised and data output was reliable.

A.2.6 Software Architecture

With the selection of the Teensy 4.0 platform, this project was programmed in C using the Arduino IDE (Arduino AG, Italy) with the PJRC Teensyduino software add-on, which enables compatibility between the Teensy and Arduino platforms. The main tasks to complete are reading the GNSS and IMU data and storage to memory. The sample rate of the IMU and GNSS sensors was set at 50Hz and 10Hz respectively, which therefore drove the maximum loop time to 20ms to avoid data asynchrony. There were several sources of latency in the system to consider, which were from the IMU that was likely due to the internal CPU that computes the sensor fusion output and also whilst writing to SD memory. These are both non-constant latency figures, which was observed to be in the order of 3-6ms to read from the IMU and up to 80ms for the SD write. For both IMUs, the read procedure can take up to 12ms to complete, which leaves a remaining 8ms to read the GNSS data and perform a write to memory, which presented an issue.

When performance testing using a simple loop programming architecture (which executed peripheral read and SD card write operations consecutively), loop duration often took longer than 20ms to complete and therefore, caused inconsistency in the timing of the data obtained. It is not possible for this system with these components to run on a simple loop architecture due to loop durations regularly exceeding 20ms. Therefore, to solve issues in this a real time operating system (RTOS) was introduced to schedule tasks.

The premise of an RTOS is to split the program into schedulable and sequential tasks, where certain tasks can possess a priority over others to ensure that they are executed at the correct time [142]. Using the RTOS, the code flow was programmed into two main scheduled tasks; IMU task and data storage and GNSS task. An architecture implementing prioritisation, pre-emptive scheduling and a counting semaphore for task synchronisation and intertask communication was used.

The IMU task was scheduled with highest priority, ensuring that the IMU data was always retrieved at the correct time. The second task saves the IMU data to the excel file, retrieves the GNSS messages from the buffer and saves them to file.

The RTOS architecture can be seen in the sequence diagram in Figure A.1 below. The IMU is subject to a built-in calibration procedure at start up before any other events occur. Logging does not commence until the GNSS receiver reaches a threshold of 8 minimum satellite fixes and a PDOP <1.2, which are considered as reasonable values in this case. After this condition has been met, the logging commences and the system is in normal operation mode. Logging continues until the power is cut. The LED is programmed to indicate sensor status for each of the system modes.

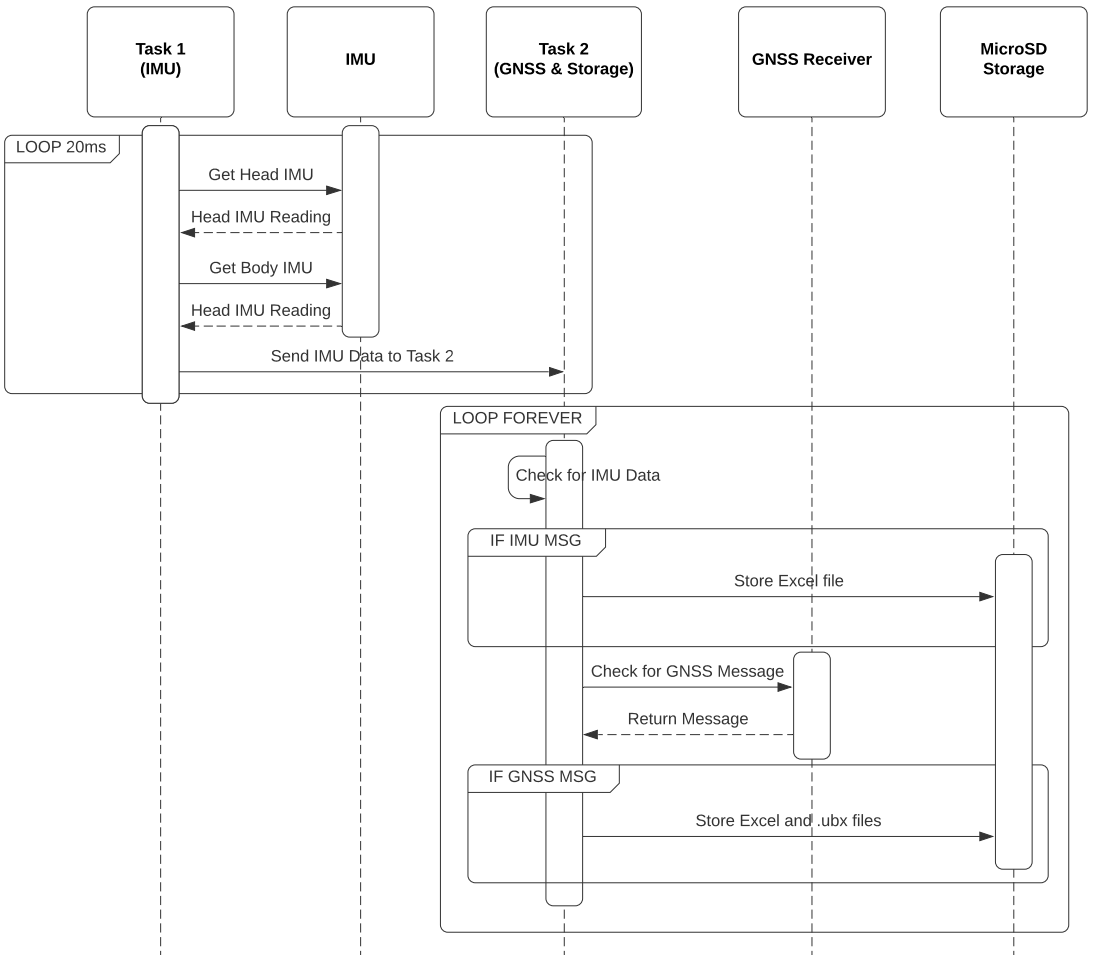


Figure A.1: RTOS Sequence Diagram

Filing Setup

The sensor is programmed to generate two files; one configured as a .csv file to store the IMU and GNSS PVT messages and the second, which stores raw satellite observation and navigation data for use in PPK processing in the .ubx u-Blox binary format [139]. This .ubx format can be imported directly into a range of post processing software packages.

A.2.7 Sensor Operation

For the best success when using PPK correction, it is important that the receiver has a lock on to as many satellites as possible. It takes time to acquire a good satellite fix; especially if the receiver is being started up in a new location for the first time. After the logger enters normal operation mode, the sensor is left stationary for approximately 30 minutes to continue to obtain more satellite fixes and a prolonged period of good quality data. This period of quality satellite lock before the experiment is required to ensure that the solution achieves a fix, which is where the most accurate PPK solution has been achieved. The time taken for this to occur is known as Time To First Fix (TTFF). After this stationary period, the sensor can be equipped to the study species for logging.

A.2.8 Post Processing Software Overview

There are a multitude of available offline, online, open-source and subscription-based software packages for PPK processing. RTKLIB was the software suite of choice, due to its capability and accessibility as it is open source. rtklibexplorer has written a version of this suited for low cost GNSS receivers and with specific support for the F9P, with which it has been tested extensively [101]. The version used in this work are the demo5 b34d binaries, which were forked from RTKLIB version 2.4.3 b34 released on 29/12/2020 [94].

Post Processing Using RTKLIB

RTKLIB includes a complete set of executables to compute PPK processing. RTKCONV is used to convert the recorded .ubx files into a RINEX observation file (obs) and a navigation file (nav) in RINEX 3 format. RTKPOST is used to post process the solution using the PPK Static setting for stationary data and the PPK Kinematic setting for dynamic data. This uses the converted RINEX obs and nav files from the F9P sensor, the RINEX obs file from the reference station service. OS does not provide the navigation file through OS Net and expect the user to use the one generated from their recordings via RTKCONV. RTKPLOT can be used to visualise results quickly before importing into MATLAB.

The settings for processing were taken from RTKLIBexplorer's recommended parameters for u-Blox receivers. The parameters that were changed include the solution type as static or kinematic as mentioned above and the base position.

Coordinate Conversion

To correctly process the PPK solution and enable a comparison between the PPK solution and the receiver's internal PVT solution, it is necessary to ensure that both results are in the same coordinate system. In this case, the PVT solution is in WGS84, whereas the OS Net base station file is in ETRS89. The coordinate system of the PPK solution is dependent on that of the base station file. In this case, it is simplest to convert the coordinates of the base RINEX file (found under APPROX POSITION XYZ in the file header) to WGS84 before processing to ensure that all coordinates are in the WGS84 reference coordinate system.

An ETRS89 to WGS84 coordinate transformation is equivalent to an ETRF97 e2009.756 to ITRF2008 e2021.5 conversion. This can be done using the EUREF Permanent Network (EPN) coordinate transformation tool [103]. To convert between epochs (e2009.756 to e2021.5) as well as reference frames (ETRF to ITRF), it is necessary to estimate the tectonic plate velocities, which can be done using the UNAVCO calculator [104]. For this, the NUVEL 1A tectonic plate motion model with no net rotation (NNR) was used.

A.2.9 Circuit Wiring Diagram

The circuit wiring diagram is presented in figure A.2.

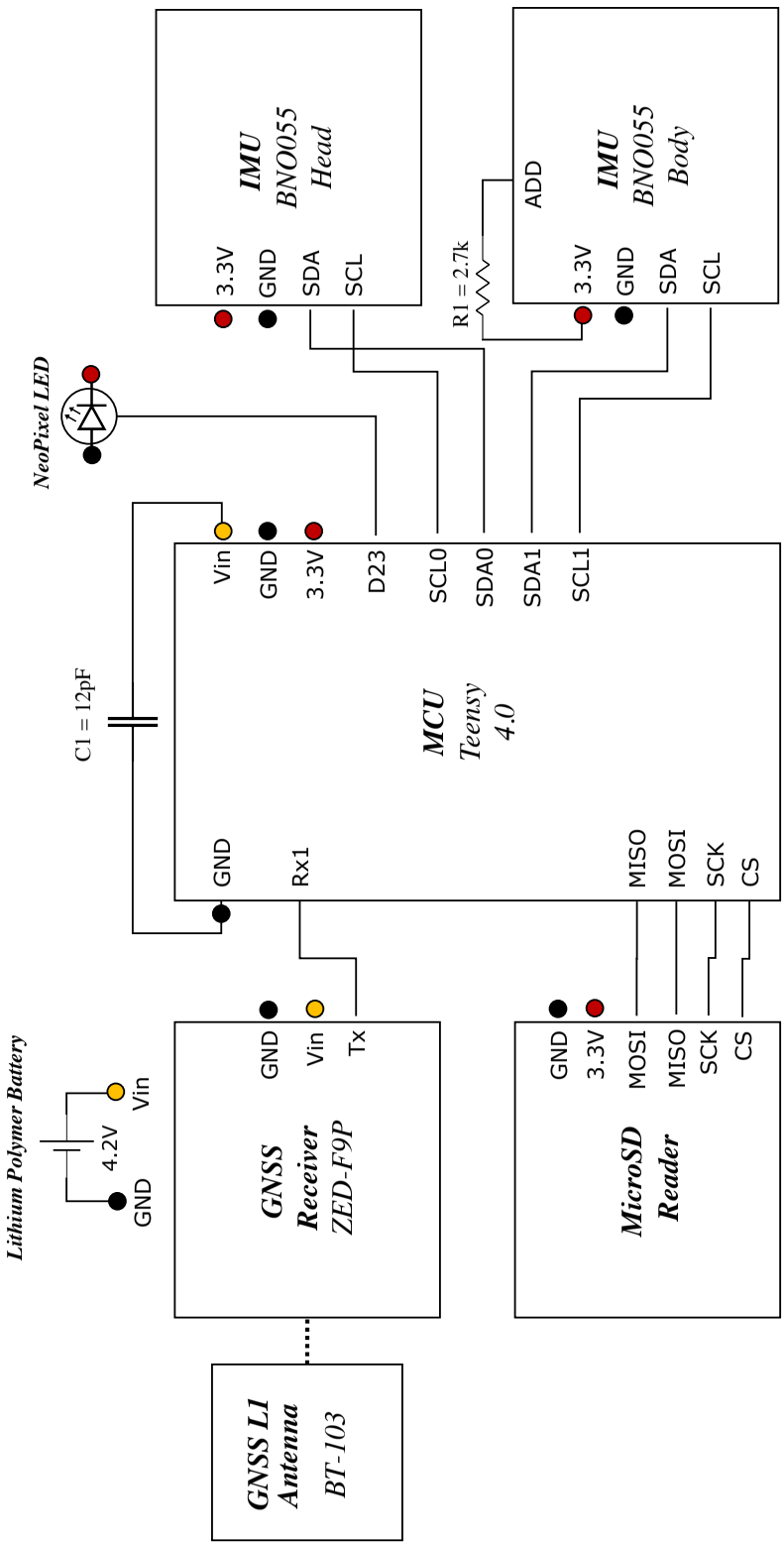


Figure A.2: Biologger circuit wiring diagram for a logger using two IMUs. Boxed components are separate PCB assemblies wired together as shown. Regulated 3.3V from Teensy supplies IMUs, SD card reader and LED. Resistor R1 changes the I2C address of the IMU to 0x29. Capacitor C1 is a decoupling capacitor for RFI reduction

B

Supplementary for Chapter 3 - Guidance Modelling

B.1 Augmented PN and PN+PP

To attempt to understand whether the birds are sensing and using target acceleration in their guidance loop, we fitted augmented PN and the mixed guidance law using the augmented definiton of PN to the measured flight trajectories. Augmented PN (APN) is an alternate form of PN used in missile literature which uses an additional term that allows response to target acceleration perpendicular to the line-of sight-vector [49]. The guidance equation for APN can be seen in equation B.1 below:

$$\boldsymbol{a}_P(t) = N(\boldsymbol{v}_P\omega + \frac{\hat{\boldsymbol{a}}_T}{2}.\frac{\boldsymbol{v}_P}{\boldsymbol{v}_C}) \tag{B.1}$$

where $\boldsymbol{v}_P$ is the velocity of the pursuer, $\boldsymbol{v}_C$ is the closing velocity $(\boldsymbol{v}_P - \boldsymbol{v}_T)$, $\hat{\boldsymbol{a}}_T$ is the target acceleration normal to the LoS vector, N is the navigation constant and ω is the vector form of the LoS vector.

For the mixed guidance law (APN+PP), this is written as before with the definition of PP:

$$\boldsymbol{a}_P(t) = N(\boldsymbol{v}_P\omega + \frac{\hat{\boldsymbol{a}}_T}{2}.\frac{\boldsymbol{v}_P}{\boldsymbol{v}_C}) - K\delta \times \boldsymbol{v}_P \tag{B.2}$$

Each guidance law was fitted globally to the 54 flights and the optimally fitted guidance parameters for each model are presented in table B.1. We then compared the performance of APN and APN+PP across all flights to the fit results for PN and PN+PP and present these as a box plot (see Fig. B.1). The median error for APN and APN+PP are higher than the results for the respective PN and PN+PP models. When observing the simulated trajectories in Figure B.2, despite similar error figures across Q1, median and Q3, the performance of the mixed guidance law using augmented proportional navigation is considerably worse than for AN

Table B.1: Globally fitted guidance parameters for augmented PN and the mixed guidance law using augmented proportional navigation and proportional pursuit.

Guidance Law	Median Error	N	K	τ
APN	2.88	1.3	-	0.02
APN+PP	1.78	4.4	5.2	0.06

alone, which suggests that the PP part significantly affects the is to be expected with such a high fitted gain ($K = 5.2$). This explains the abrupt changes in pursuer centripetal acceleration observed in the trajectory plots in Figure B.2 when fitted with APN+PP. Clearly, the performance of APN and APN+PP neither matches nor improves on the fit error achieved by using the standard formulations of PN or the mixed guidance law. We attribute this to variable noise present in the acceleration signal across all flights leading to an unreliable set of data to obtain a global optimum of fitted values. Therefore, we cannot use this to make a reliable conclusion on the sensory information used by the birds during pursuit flight.

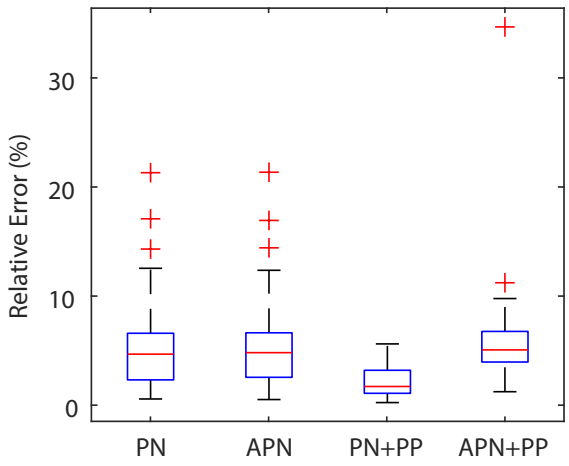


Figure B.1: Comparison of augmented and standard guidance law fit performance. Box plot showing relative error distribution over all 54 flights between measured and simulated flight trajectories for each guidance law using the guidance parameters found from global optimisation. The centre line of each box denotes the median for all flights. The upper and lower bounds of the box denote the 3rd and 1st quartiles. Crosses indicate outliers falling >1.5 times the interquartile range beyond the 1st or third quartile.

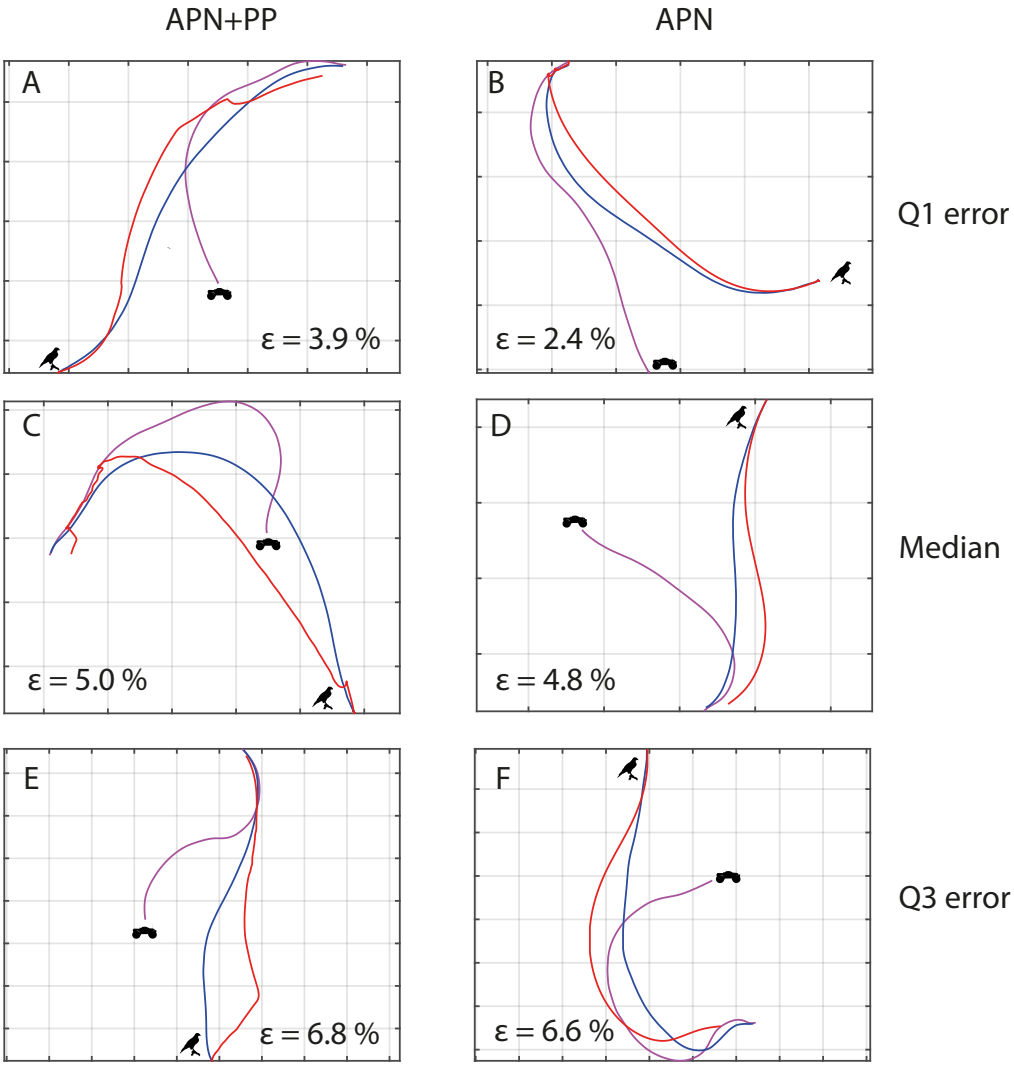


Figure B.2: Showing simulated trajectories for guidance laws using the global fitted optimum values (seen in table B.1 using augmented PN: A, C, E showing Q1, Q2 and Q3 error for APN+PP and B, D, F showing Q1, Q2 and Q3 error for APN. ε shows the relative error in percent calculated as the RMS error divided by the flight length.

C

Supplementary for Chapter 4 - Gaze Strategy in Harris's Hawks

C.1 Supplementary Methods

C.1.1 GNSS Data Processing

A pre-processing pipeline was developed to analyse the raw data obtained from all sensors and output synchronised trajectory data from the bird and lure GNSS receivers and the bird head IMU for each flight. GNSS data was first PPK post processed using RTKLIB; an open-source program for GNSS positioning (28, 29). Bird and target GNSS data were processed using the Kidlington (OXFR) Ordnance Survey OSNet antenna as the reference base station, which was located within 6km of the study site. The GNSS receiver outputs coordinates in the WGS84 reference coordinate system, whilst the OSNet reference antenna RINEX files output coordinates in ETRS89 reference frame. To process the PPK solution in the same coordinate system, the position of the reference antenna was converted to WGS84 for processing in RTKLIB. For this data collected in 2021, an ETRS89 to WGS84 coordinate transformation is equivalent to an ETRF97 e2009.756 to ITRF2008 e2021.5 conversion. This was done using the EUREF Permanent Network (EPN) coordinate transformation tool (30). To convert between epochs (e2009.756 to e2021.5) as well as reference frames (ETRF to ITRF), it is necessary to estimate the tectonic plate velocities, which was done using the UNAVCO calculator (31). For this, the NUVEL 1A tectonic plate motion model with no net rotation (NNR) was used. The SBAS and PPK position data were converted from the geodetic reference frame (longitude, latitude, height) with units in decimal degrees and height in metres to the local tangential ENU coordinate reference frame with units in metres using the base station positioned on the cricket pitch as the origin. A flight velocity quality control procedure was used to ensure that the average velocity extracted from differenced position was within a threshold of the measured Doppler ground speed. We developed a post processing method called interpolated PPK for the

GNSS data captured from the bird sensor as excessive perturbation of the antenna during flight limited the availability of a true PPK solution. This correction used the error between a single PPK and SBAS position point before and after each flight and applied a linear interpolation of this to the flight data. The PPK position was always available for the target trajectory. All data was output from bird flight start until the point of target interception. Flight intercept timing was based on a 0.6m threshold distance between the measured bird and lure positions. A value of 0.3m accounted for the distance from target antenna to the position of the lure on the radio-controlled car and an additional 0.3m was used to account for leg extension, and position offset of the GNSS antenna on the back of the bird. When the bird was in the catch phase within this threshold, it was concluded that guidance had ended and so it was taken as the end point for simulation. This process was also used as a quality control check to discard any flights where the bird and lure were not present within the threshold. An independent velocity quality control check between integration of IMU acceleration and differentiation of GNSS position was used to remove flights that did not meet a correlation threshold of >0.8. Further flights were removed where the head IMU data was unavailable. After all quality control, a total sample of n=42 flights were obtained for guidance simulation.

C.1.2 IMU Calibration

To perform IMU calibration, each hawk was positioned at a fixed location known by the output of the worn GNSS logger and made to look at the GNSS base station. The time when the bird's head aligned to the base station was recorded on a camera with timecode synchronised to GPS time. Then the orientation output of the IMU was compared to the true bearing known between the positions of the two GNSS receivers and the calculated systematic error removed from the IMU data for each flight.

C.2 Supplementary Figures

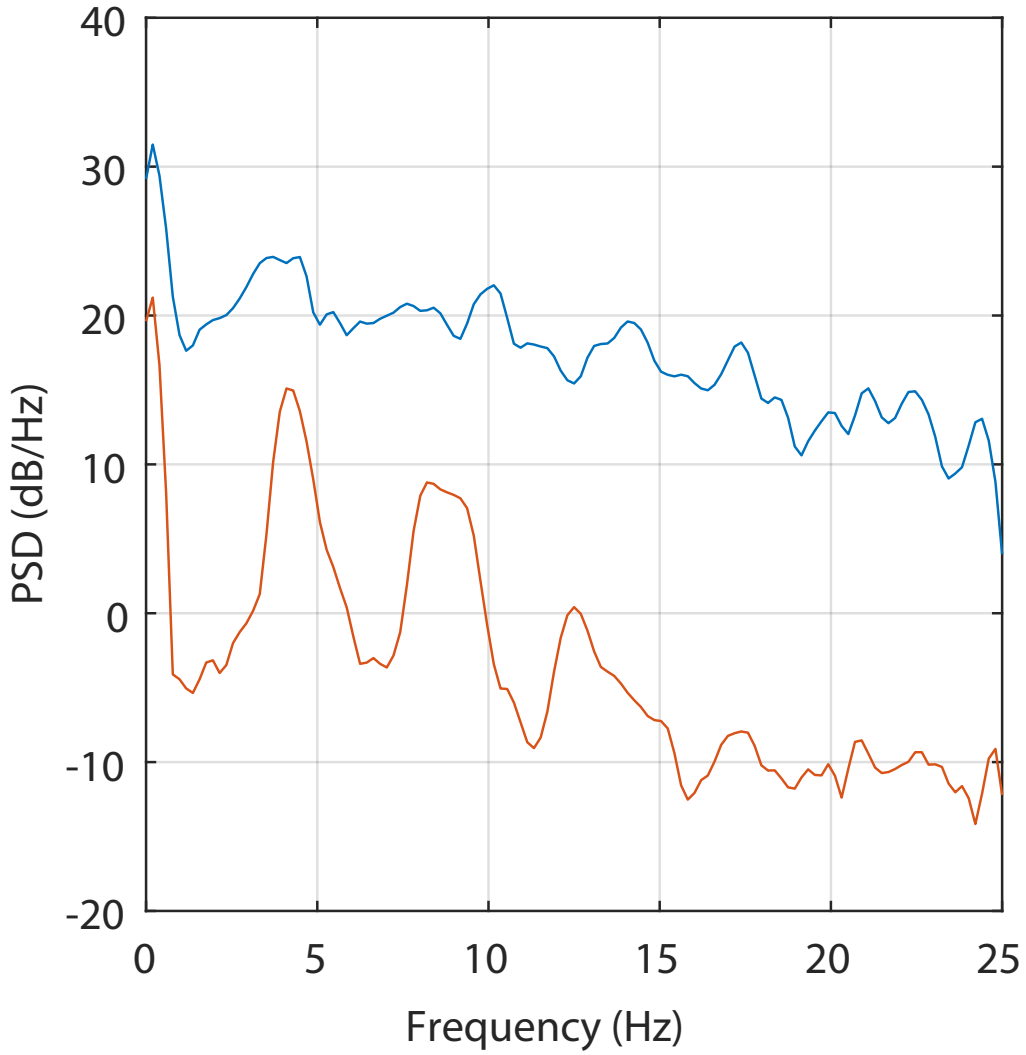


Figure C.1: Power spectral density of head yaw rate (blue) and vertical linear acceleration (red) for a single flight.

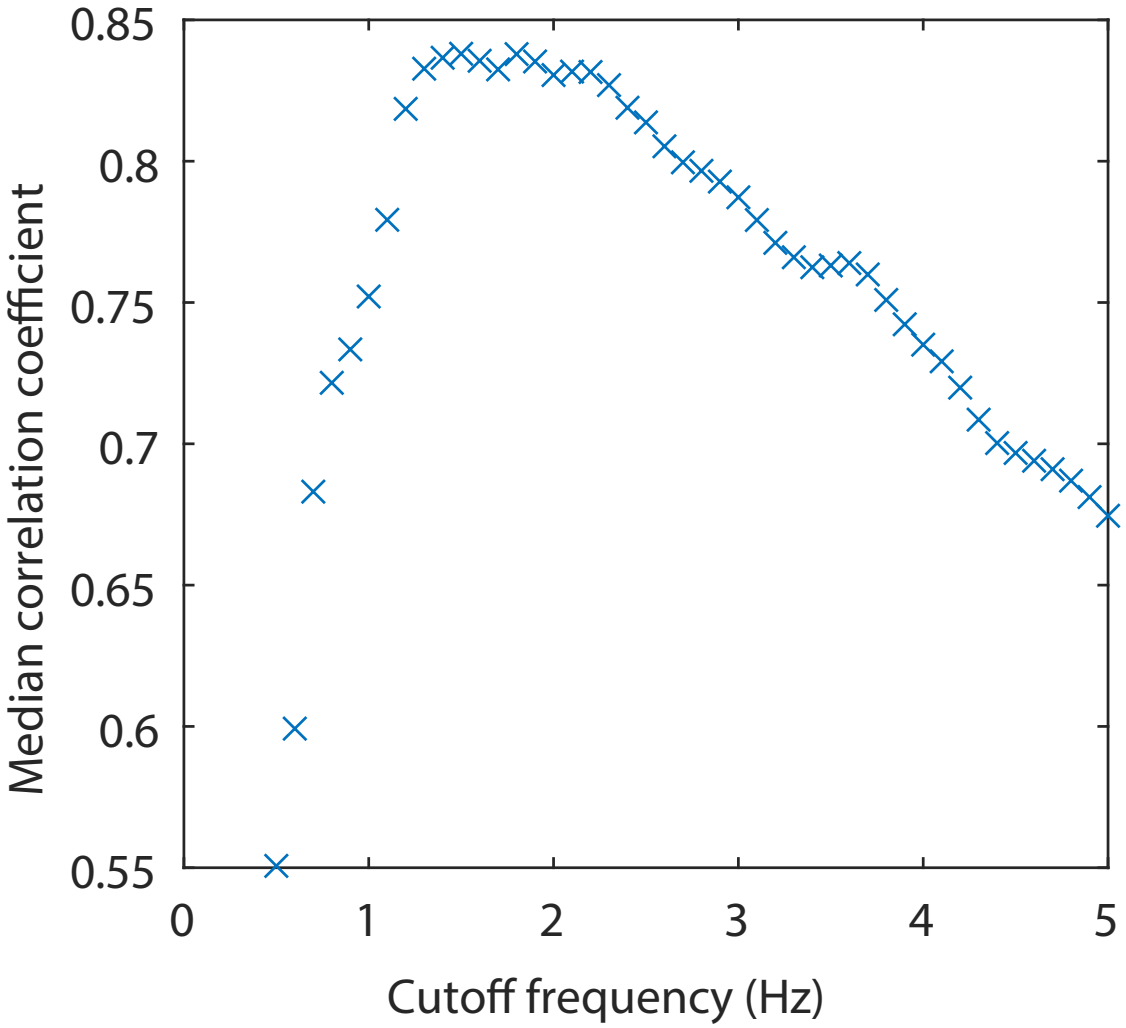


Figure C.2: Scatter plot of median correlation coefficient over all flights between inertially derived line-of-sight rate and head yaw rate filtered using a low pass filter with different cutoff frequencies in the interval [0.5:0.1:5] Hz.

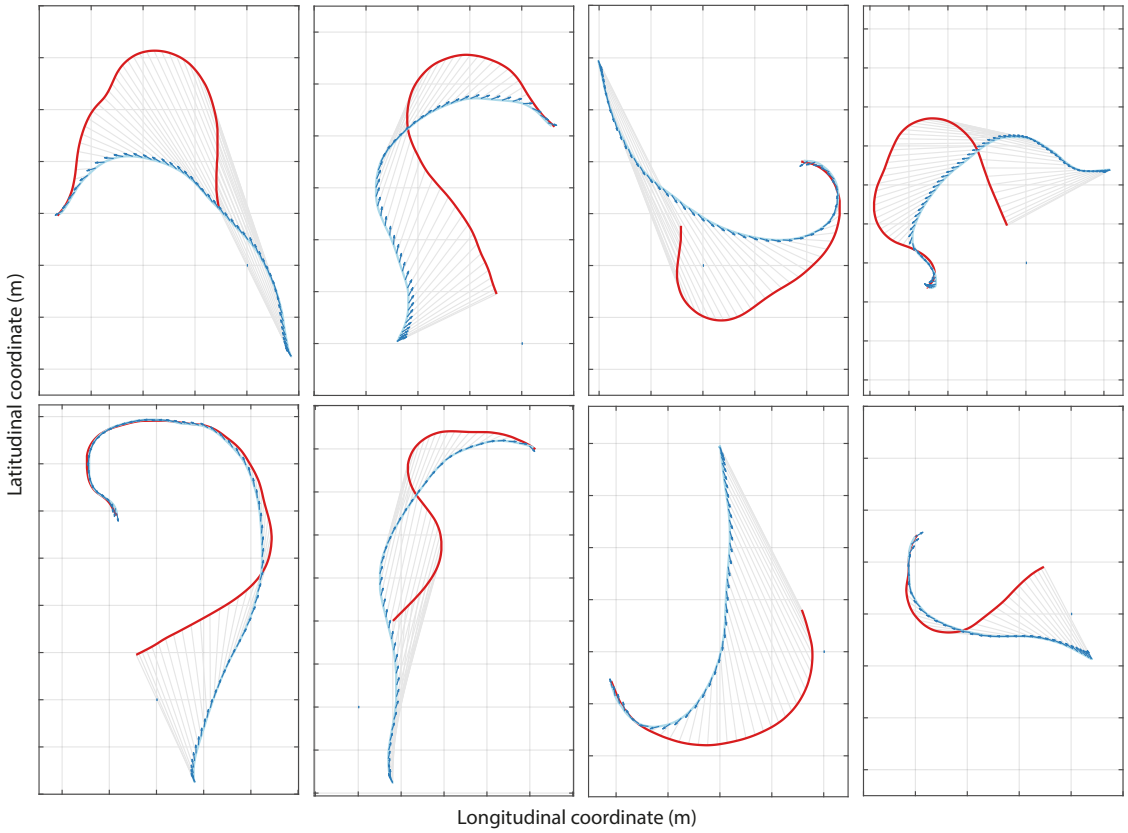


Figure C.3: 2D trajectory plots showing how the head gaze bearing (blue arrows) and instantaneous line-of-sight vectors (grey) between the hawk (blue) and the target (red) vary throughout 8 flights

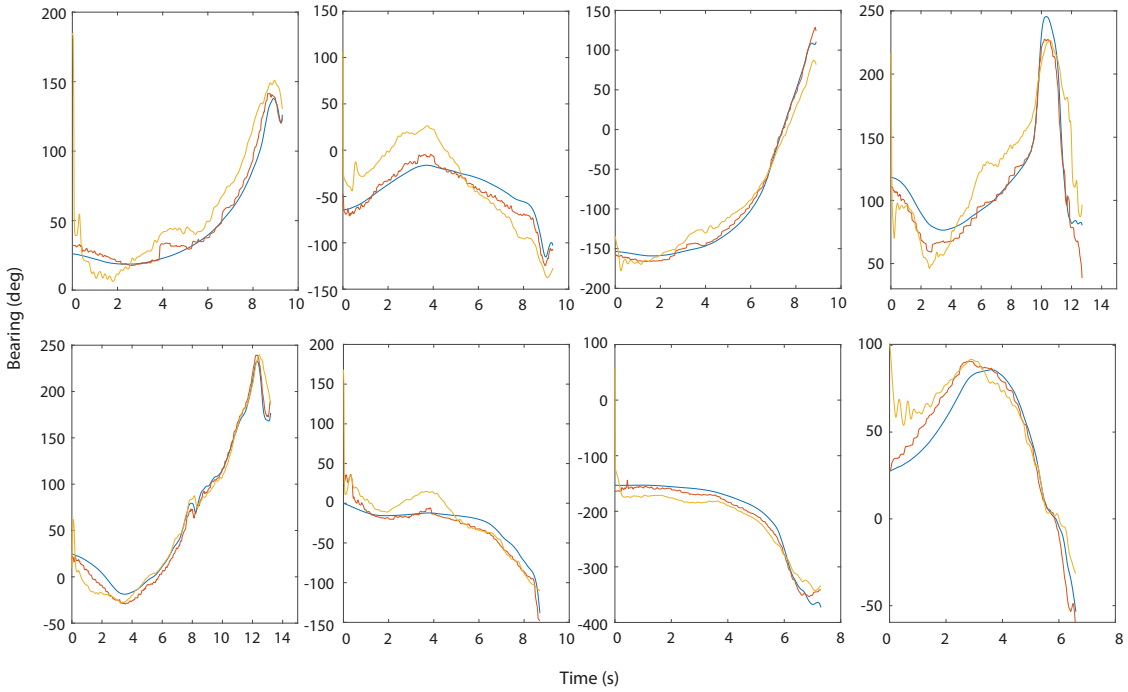


Figure C.4: Time histories of head yaw bearing (red), LoS bearing (blue) and track angle (yellow) bearing for 8 flights.

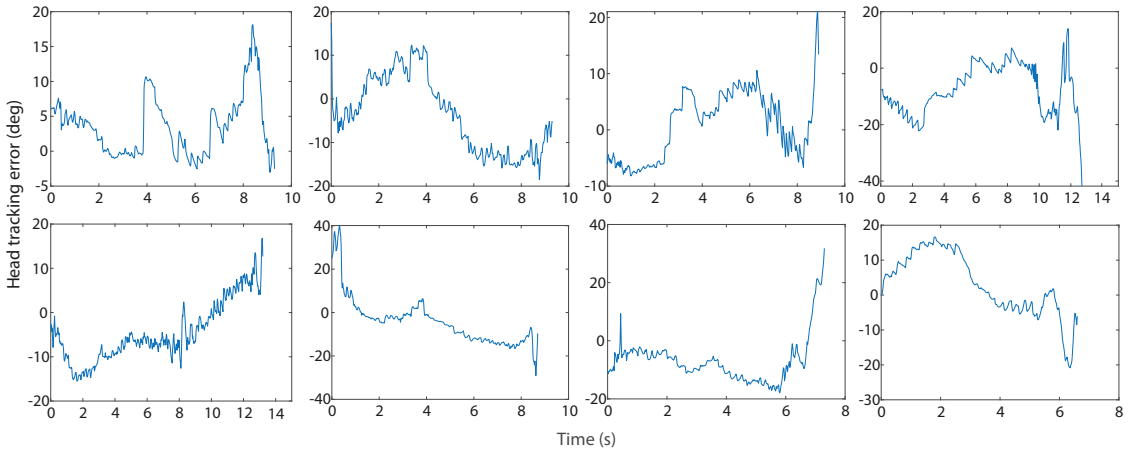


Figure C.5: Time history of head tracking error for 8 flights.

References

[1] Michael F Land and Dan-Eric Nilsson. *Animal eyes*. OUP Oxford, 2012.

[2] Suzanne Amador Kane, Andrew H Fulton, and Lee J Rosenthal. "When hawks attack: animal-borne video studies of goshawk pursuit and prey-evasion strategies". In: *Journal of Experimental Biology* 218.2 (2015), pp. 212–222.

[3] Robert M Olberg. "Visual control of prey-capture flight in dragonflies". In: *Current opinion in neurobiology* 22.2 (2012), pp. 267–271.

[4] Kaushik Ghose et al. "Echolocating bats use a nearly time-optimal strategy to intercept prey". In: *PLoS biology* 4.5 (2006), e108.

[5] Norbert Boeddeker, Roland Kern, and Martin Egelhaaf. "Chasing a dummy target: smooth pursuit and velocity control in male blowflies". In: *Proceedings of the Royal Society of London. Series B: Biological Sciences* 270.1513 (2003), pp. 393–399.

[6] SW Zhang et al. "Visual tracking of moving targets by freely flying honeybees". In: *Visual neuroscience* 4.4 (1990), pp. 379–386.

[7] Andreas F Haselsteiner, Cole Gilbert, and Z Jane Wang. "Tiger beetles pursue prey using a proportional control law with a delay of one half-stride". In: *Journal of the Royal Society Interface* 11.95 (2014), p. 20140216.

[8] Michael F Land and Thomas S Collett. "Chasing behaviour of houseflies (Fannia canicularis)". In: *Journal of comparative physiology* 89.4 (1974), pp. 331–357.

[9] Andrew M Hein et al. "An algorithmic approach to natural behavior". In: *Current Biology* 30.11 (2020), R663–R675.

[10] Caroline H Brighton, Adrian L R Thomas, and Graham K Taylor. "Terminal attack trajectories of peregrine falcons are described by the proportional navigation guidance law of missiles". In: *Proceedings of the National Academy of Sciences of the United States of America* 114 (51 2017), pp. 13495–13500. URL: %3CGo%20to%20ISI%3E://WOS:000418321600063.

[11] Caroline H Brighton and Graham K Taylor. "Hawks steer attacks using a guidance system tuned for close pursuit of erratically manoeuvring targets". In: *Nature Communications* 10 (1 2019). URL: https://doi.org/10.1038/s41467-019-10454-z.

[12] Caroline H Brighton et al. "Attack behaviour in naive gyrfalcons is modelled by the same guidance law as in peregrine falcons, but at a lower guidance gain". In: *Journal of Experimental Biology* 224 (5 2021), jeb238493.

[13] Samuel T Fabian et al. "Interception by two predatory fly species is explained by a proportional navigation feedback controller". In: *Journal of The Royal Society Interface* 15.147 (2018), p. 20180466.

[14] Robert M Olberg et al. "Eye movements and target fixation during dragonfly prey-interception flights". In: *Journal of comparative physiology A* 193 (2007), pp. 685–693.

[15] Matteo Mischiati et al. "Internal models direct dragonfly interception steering". In: *Nature* 517.7534 (2015), pp. 333–338.

[16] Paloma T Gonzalez-Bellido et al. "Eight pairs of descending visual neurons in the dragonfly give wing motor centers accurate population vector of prey direction". In: *Proceedings of the National Academy of Sciences* 110.2 (2013), pp. 696–701.

[17] Neryahu A Shneydor. *Missile guidance and pursuit: kinematics, dynamics and control*. Elsevier, 1998.

[18] Graham R Martin. "Visual fields and their functions in birds". In: *Journal of Ornithology* 148.2 (2007), pp. 547–562.

[19] Colleen T O'Rourke et al. "Hawk eyes I: diurnal raptors differ in visual fields and degree of eye movement". In: *PloS one* 5.9 (2010), e12802.

[20] Colleen T O'Rourke et al. "Hawk eyes II: diurnal raptors differ in head movement strategies when scanning from perches". In: *PLoS One* 5.9 (2010), e12169.

[21] Josh Wallman and John D Pettigrew. "Conjugate and disjunctive saccades in two avian species with contrasting oculomotor strategies". In: *Journal of Neuroscience* 5.6 (1985), pp. 1418–1428.

[22] Simon Potier et al. "Visual abilities in two raptors with different ecology". In: *Journal of Experimental Biology* 219.17 (2016), pp. 2639–2649.

[23] Graham R Martin. "What is binocular vision for? A birds' eye view". In: *Journal of Vision* 9.11 (2009), pp. 14–14.

[24] Katherine V Fite and Sheila Rosenfield-Wessels. "A comparative study of deep avian foveas". In: *Brain, Behavior and Evolution* 12.1-2 (1975), pp. 97–115.

[25] David B Meyer. "The avian eye and its adaptations". In: *The visual system in vertebrates*. Springer, 1977, pp. 549–611.

[26] George M Siouris. *Missile guidance and control systems*. Springer Science & Business Media, 2004.

[27] James Walker. "Visual guidance of target-oriented flight behaviours in birds". PhD thesis. University of Oxford, 2018.

[28] G L Walls. "The evolutionary history of eye movements". In: *Vision Research* 2 (1-4 1962), pp. 69–80.

[29] Raymond Dodge. "Five types of eye movement in the horizontal meridian plane of the field of regard". In: *American journal of physiology-legacy content* 8.4 (1903), pp. 307–329.

[30] Do A Robinson. "The mechanics of human smooth pursuit eye movement." In: *The Journal of Physiology* 180.3 (1965), p. 569.

[31] Stephen G Lisberger, Edward Joseph Morris, and Lawrence Tychsen. "Visual motion processing and sensory-motor integration for smooth pursuit eye movements". In: *Annual review of neuroscience* 10.1 (1987), pp. 97–129.

[32] Jolande Fooken, Philipp Kreyenmeier, and Miriam Spering. "The role of eye movements in manual interception: A mini-review". In: *Vision Research* 183 (2021), pp. 81–90.

[33] Leigh A Mrotek and John F Soechting. "Target interception: hand–eye coordination and strategies". In: *Journal of Neuroscience* 27.27 (2007), pp. 7297–7309.

[34] Cristina de la Malla, Jeroen BJ Smeets, and Eli Brenner. "Potential systematic interception errors are avoided when tracking the target with one's eyes". In: *Scientific reports* 7.1 (2017), p. 10793.

[35] Jolande Fooken et al. "Eye movement accuracy determines natural interception strategies". In: *Journal of vision* 16.14 (2016), pp. 1–1.

[36] Frederic R Danion et al. "More precise tracking of horizontal than vertical target motion with both the eyes and hand". In: *Cortex* 134 (2021), pp. 30–42.

[37] AF Fuchs. "Saccadic and smooth pursuit eye movements in the monkey". In: *The Journal of physiology* 191.3 (1967), p. 609.

[38] Martha G MacAvoy, Jacqueline P Gottlieb, and Charles J Bruce. "Smooth-pursuit eye movement representation in the primate frontal eye field". In: *Cerebral Cortex* 1.1 (1991), pp. 95–102.

[39] Clara Bourrelly et al. "Learning the trajectory of a moving visual target and evolution of its tracking in the monkey". In: *Journal of Neurophysiology* 116.6 (2016), pp. 2739–2751.

[40] Norbert Boeddeker and Martin Egelhaaf. "A single control system for smooth and saccade-like pursuit in blowflies". In: *Journal of experimental biology* 208.8 (2005), pp. 1563–1572.

[41] Thomas S Collett and MF Land. "Visual control of flight behaviour in the hoverflySyritta pipiens L." In: *Journal of comparative physiology* 99.1 (1975), pp. 1–66.

[42] Huai-Ti Lin and Anthony Leonardo. "Heuristic rules underlying dragonfly prey selection and interception". In: *Current Biology* 27.8 (2017), pp. 1124–1137.

[43] Dennis Eckmeier et al. "Gaze strategy in the free flying zebra finch (Taeniopygia guttata)". In: *PLoS One* 3.12 (2008), e3956.

[44] Ivo G Ros and Andrew A Biewener. "Pigeons (C. livia) follow their head during turning flight: head stabilization underlies the visual control of flight". In: *Frontiers in neuroscience* 11 (2017), p. 655.

[45] J H V Hateren and C Schilstra. "Blowfly flight and optic flow. II. Head movements during flight". In: *Journal of Experimental Biology* 202 (11 1999), pp. 1491–1500.

[46] C Schilstra and J H Van Hateren. "Stabilizing gaze in flying blowflies". In: *Nature* 395 (6703 1998), p. 654.

[47] Vance A Tucker. "The deep fovea, sideways vision and spiral flight paths in raptors". In: *Journal of Experimental Biology* 203.24 (2000), pp. 3745–3754.

[48] Suzanne Amador Kane and Marjon Zamani. "Falcons pursue prey using visual motion cues: new perspectives from animal-borne cameras". In: *Journal of Experimental Biology* 217.2 (2014), pp. 225–234.

[49] Neil F Palumbo, Ross A Blauwkamp, and Justin M Lloyd. "Basic principles of homing guidance". In: *Johns Hopkins APL Technical Digest* 29.1 (2010), pp. 25–41.

[50] Rexford D Lord, Frank C Bellrose, and William W Cochran. "Radiotelemetry of the Respiration of a Flying Duck". In: *Science* 137 (3523 1962), pp. 39–40.

[51] Cobert D LeMunyan et al. "Design of a Miniature Radio Transmitter for Use in Animal Studies". In: *The Journal of Wildlife Management* 23 (1 1959), pp. 107–110.

[52] Sivan Toledo et al. "Lessons and experiences from the design, implementation, and deployment of a wildlife tracking system". In: *2016 IEEE International Conference on Software Science, Technology and Engineering (SWSTE)*. IEEE. 2016, pp. 51–60.

[53] Simon P Ripperger et al. "Thinking small: next-generation sensor networks close the size gap in vertebrate biologging". In: *PLoS biology* 18.4 (2020), e3000655.

[54] R Kays et al. "Tracking Animal Location and Activity with an Automated Radio Telemetry System in a Tropical Rainforest". In: *The Computer Journal* 54 (12 2011), pp. 1931–1948.

[55] "Migration and Stopover in a Small Pelagic Seabird, the Manx Shearwater Puffinus puffinus: Insights from Machine Learning". In: *Proceedings: Biological Sciences* 276 (1660 2009), pp. 1215–1223.

[56] W J Fuller et al. "Utility of geolocating light loggers for indicating at-sea movements in sea turtles." In: *Endang Species Res.* (4 2008), pp. 139–146.

[57] Roger D Hill. *Theory of geolocation by light levels*. Ed. by B J Le Boeuf and R M Laws. 1994, pp. 227–236.

[58] Adam M Fudickar, Martin Wikelski, and Jesko Partecke. "Tracking migratory songbirds: accuracy of light-level loggers (geolocators) in forest habitats". In: *Methods in Ecology and Evolution* 3 (1 2012), pp. 47–52.

[59] Tim Guilford et al. "A Dispersive Migration in the Atlantic Puffin and Its Implications for Migratory Navigation". In: *PLoS ONE* 6 (7 2011), e21336.

[60] John J Craighead et al. "Satellite Monitoring of Black Bear". In: *BioScience* 21 (24 1971), pp. 1206–1212.

[61] Collecte Localisation Satellites. *Argos User's Manual*. 2016. URL: `www.argos-system.org/wp-content/uploads/2016/08/r363_9_argos_users_manual-v1.6.6.pdf`.

[62] Mark R Fuller, William S Seegar, and Linda S Schueck. "Routes and Travel Rates of Migrating Peregrine Falcons Falco peregrinus and Swainson's Hawks Buteo swainsoni in the Western Hemisphere". In: *Journal of Avian Biology* 29 (4 1998), pp. 433–440.

[63] BJ Le Boeuf et al. "Foraging ecology of northern elephant seals". In: *Ecological monographs* 70.3 (2000), pp. 353–382.

[64] Max Planck Institute of Animal Behavior. *Icarus*. 2022. URL: `https://www.icarus.mpg.de/en`.

[65] "Biological Earth observation with animal sensors". In: *Trends in Ecology and Evolution* 37 (4 2022), pp. 293–298. URL: https://www.sciencedirect.com/science/article/pii/S0169534721003165.

[66] Navigation National Executive Committee for Space-Based Positioning and Timing. *GPS Accuracy*. 2021. URL: https://www.gps.gov/systems/gps/performance/accuracy/#sa.

[67] Novatel Inc. *An introduction to GNSS*. 2015.

[68] Arthur R Rodgers, Robert S Rempel, and Kenneth F Abraham. "A GPS-Based Telemetry System". In: *Wildlife Society Bulletin (1973-2006)* 24 (3 1996), pp. 559–566. URL: http://ezproxy-prd.bodleian.ox.ac.uk:2154/stable/3783345.

[69] Max Planck Institute of Animal Behavior. *Movebank*. 2022. URL: https://www.movebank.org/cms/movebank-main.

[70] Ariana Strandburg-Peshkin et al. "Shared decision-making drives collective movement in wild baboons". In: *Science* 348.6241 (2015), pp. 1358–1361.

[71] Oliver Padget et al. "Shearwaters know the direction and distance home but fail to encode intervening obstacles after free-ranging foraging trips". In: *Proceedings of the National Academy of Sciences* 116.43 (2019), pp. 21629–21633.

[72] Deane Bunce. "Wide area augmentation system (WAAS) status and history". In: ed. by F A A. 2014. URL: https://www.gps.gov/multimedia/presentations/2014/09/ION/bunce.pdf.

[73] European Global Navigation Satellite Systems Agency. *EGNOS Open Service (OS) Service Definition Document,* 2.3, 2017. URL: https://egnos-user-support.essp-sas.eu/new_egnos_ops/documents/egnos-sdd/egnos-open-service-sdd.

[74] US Department of Defense. "Global positioning system standard positioning service performance standard". In: (2020). URL: https://www.gps.gov/technical/ps/2020-SPS-performance-standard.pdf.

[75] European Global Navigation Satellite Systems Agency. *EGNOS Open Service (OS) Service Definition Document,* 2.3, 2017. URL: https://egnos-user-support.essp-sas.eu/new_egnos_ops/documents/egnos-sdd/egnos-open-service-sdd.

[76] Amedeo Rodi Vetrella et al. "Multi-UAV Carrier Phase Differential GPS and Vision-based Sensing for High Accuracy Attitude Estimation". In: *Journal of Intelligent and Robotic Systems* 93 (1-2 2019), pp. 245–260.

[77] Julián Tomaštík et al. "UAV RTK/PPK Method—An Optimal Solution for Mapping Inaccessible Forested Areas?" In: *Remote Sensing* 11 (6 2019), p. 721. URL: https://www.mdpi.com/2072-4292/11/6/721/pdf.

[78] B Richard. Langley. "RTK GPS". In: *GPS World* (1998).

[79] Johannes Traugott. "Precise flight trajectory reconstruction based on time-differential GNSS carrier phase processing". PhD thesis. Technische Universität München, 2011.

[80] G Sachs. "In-flight measurement of upwind dynamic soaring in albatrosses". In: *Progress in Oceanography* 142 (2016), pp. 47–57. URL: %3CGo%20to%20ISI%3E://WOS:000373863800004.

[81] G Sachs et al. "Experimental verification of dynamic soaring in albatrosses". In: *Journal of Experimental Biology* 216 (22 2013), pp. 4222–4232. URL: http://jeb.biologists.org/content/216/22/4222.full.pdf.

[82] Gottfried Sachs et al. "Flying at No Mechanical Energy Cost: Disclosing the Secret of Wandering Albatrosses". In: *PLoS ONE* 7 (9 2012), e41449. URL: https://journals.plos.org/plosone/article/file?id=10.1371/journal.pone.0041449&type=printable.

[83] Hamed Haddadi et al. "Determining association networks in social animals: choosing spatial–temporal criteria and sampling rates". In: *Behavioral Ecology and Sociobiology* 65 (8 2011), pp. 1659–1668. URL: http://ezproxy-prd.bodleian.ox.ac.uk:2154/stable/41414626.

[84] Andrew J King et al. "Selfish-herd behaviour of sheep under threat". In: *Current Biology* 22 (14 2012), R561–R562. URL: https://www.sciencedirect.com/science/article/pii/S0960982212005295.

[85] James R Usherwood et al. "Flying in a flock comes at a cost in pigeons". In: *Nature* 474 (7352 2011), pp. 494–497. URL: http://europepmc.org/articles/pmc3162477?pdf=render.

[86] Steven J Portugal et al. "Upwash exploitation and downwash avoidance by flap phasing in ibis formation flight". In: *Nature* 505 (7483 2014), pp. 399–402. URL: https://researchonline.rvc.ac.uk/8076/1/8076.pdf.

[87] A M Wilson et al. "Locomotion dynamics of hunting in wild cheetahs". In: *Nature* 498 (7453 2013), pp. 185–189.

[88] Alan M Wilson et al. "Biomechanics of predator–prey arms race in lion, zebra, cheetah and impala". In: *Nature* 554 (7691 2018), pp. 183–188. URL: https://researchonline.rvc.ac.uk/11143/1/11143.pdf.

[89] Hattie Bartlam-Brooks et al. "There and back again - a zebra's tale". In: *Journal of Experimental Biology* 223 (23 2020), jeb232140.

[90] Tatjana Y Hubel et al. "Movement patterns and athletic performance of leopards in the Okavango Delta". In: *Proceedings of the Royal Society B: Biological Sciences* 285 (1877 2018), p. 20172622.

[91] Oliver P Dewhirst et al. "Improving the accuracy of estimates of animal path and travel distance using GPS drift-corrected dead reckoning". In: *Ecology and Evolution* 6 (17 2016), pp. 6210–6222. URL: https://onlinelibrary.wiley.com/doi/pdf/10.1002/ece3.2359.

[92] Monica A Daley et al. "Preferred gait and walk–run transition speeds in ostriches measured using GPS-IMU sensors". In: *Journal of Experimental Biology* 219 (20 2016), pp. 3301–3308. URL: http://jeb.biologists.org/content/219/20/3301.full.pdf.

[93] Hamideh Keshavarzi et al. "Validation of Real-Time Kinematic (RTK) Devices on Sheep to Detect Grazing Movement Leaders and Social Networks in Merino Ewes". In: *Sensors* 21 (3 2021), p. 924.

[94] Tomoji Takasu. *RTKLIB: An Open Source Program Package for GNSS Positioning*. URL: https://www.rtklib.com. (accessed: 19.12.2022).

[95] u-Blox. *ZED-F9P Integration manual*. R08. 2020. URL: https://www.u-blox.com/en/product/zed-f9p-module#tab-documentation-resources.

[96] Vaughan Pratt. "Direct least-squares fitting of algebraic surfaces". In: *SIGGRAPH Comput. Graph.* 21 (4 1987), pp. 145–152. URL: https://ezproxy-prd.bodleian.ox.ac.uk:2102/10.1145/37402.37420.

[97] Nikolai Chernov. *Circle Fit (Pratt Method)*. 2022. URL: https://uk.mathworks.com/matlabcentral/fileexchange/22643-circle-fit-pratt-method.

[98] Bosch Sensortec. *BNO055 Datasheet*. 1.8. 2021. URL: https://www.bosch-sensortec.com/media/boschsensortec/downloads/datasheets/bst-bno055-ds000.pdf.

[99] *ZED-F9P Datasheet*. UBX-21044850. u-Blox. May 2022.

[100] Bednarz JC Dwyer JF. "Birds of the world". In: 1.0. Cornell Lab of Ornithology, Ithaca, NY, USA, 2020. Chap. Harris' Hawk (Parabuteo unicinctus).

[101] rtklibexplorer. *RTKLIB demo5*. 2022. URL: https://github.com/rtklibexplorer/RTKLIB/releases. (accessed: 19.12.2022).

[102] Ordnance Survey. *OS Net RINEX Data*. 2022. URL: https://www.ordnancesurvey.co.uk/gps/os-net-rinex-data/. (accessed: 19.12.2022).

[103] Network EPG. *ETRF/ITRF Coordinate Transformation Tool (ECTT)*. 2022. URL: https://www.epncb.oma.be/_productsservices/coord_trans/. (accessed: 19.12.2022).

[104] UNAVCO. *Plate motion calculator*. 2022. URL: https://www.unavco.org/software/geodetic-utilities/plate-motion-calculator/plate-motion-calculator.html. (accessed: 19.12.2022).

[105] Haleh Fotowat et al. "A novel neuronal pathway for visually guided escape in Drosophila melanogaster". In: *Journal of neurophysiology* 102.2 (2009), pp. 875–885.

[106] Andrei Sourakov. "Faster than a flash: the fastest visual startle reflex response is found in a long-legged fly, Condylostylus sp.(Dolichopodidae)". In: *The Florida Entomologist* 94.2 (2011), pp. 367–369.

[107] Christopher L Stitt et al. "Modification of the pigeon's visual startle reaction by the sensory environment." In: *Journal of comparative and physiological psychology* 90.7 (1976), p. 601.

[108] Harold Pomeroy and Frank Heppner. "Laboratory determination of startle reaction time of the starling (Sturnus vulgaris)". In: *Animal Behaviour* 25 (1977), pp. 720–725.

[109] Daniel Kress, Evelien Van Bokhorst, and David Lentink. "How lovebirds maneuver rapidly using super-fast head saccades and image feature stabilization". In: *PLoS ONE* 10 (6 2015), e0129287.

[110] Fumihiro Kano et al. “Head-mounted sensors reveal visual attention of free-flying homing pigeons”. In: *Journal of Experimental Biology* 221 (17 2018).

[111] Michael F Land. “Motion and vision: why animals move their eyes”. In: *Journal of Comparative Physiology A* 185 (4 1999), pp. 341–352.

[112] Michael Land. “Eye movements in man and other animals”. In: *Vision Research* 162 (2019), pp. 1–7.

[113] Vance A Tucker et al. “Curved flight paths and sideways vision in peregrine falcons (Falco peregrinus)”. In: *Journal of Experimental Biology* 203 (24 2000), pp. 3755–3763.

[114] Mees Muller. “Mechanical aspects of the semicircular ducts in the vestibular system”. In: *Biological Cybernetics* 114 (4 2020), pp. 421–442.

[115] Hans Straka et al. “Vestibulo-ocular signal transformation in frequency-tuned channels”. In: *Annals of the New York Academy of Sciences* 1164.1 (2009), pp. 37–44.

[116] William M Connelly et al. “The thalamus as a low pass filter: filtering at the cellular level does not equate with filtering at the network level”. In: *Frontiers in neural circuits* 9 (2016), p. 89.

[117] Ben J Hardcastle and Holger G Krapp. “Evolution of biological image stabilization”. In: *Current Biology* 26 (20 2016), R1010–R1021.

[118] Kikuro Fukushima et al. “Cognitive processes involved in smooth pursuit eye movements: behavioral evidence, neural substrate and clinical correlation”. In: *Frontiers in systems neuroscience* 7 (2013), p. 4.

[119] Shane P Windsor and Graham K Taylor. “Head movements quadruple the range of speeds encoded by the insect motion vision system in hawkmoths”. In: *Proceedings of the Royal Society B: Biological Sciences* 284 (1864 2017), p. 20171622.

[120] James Kempton. “The dynamic flight behaviour of birds in different frames of reference”. PhD thesis. University of Oxford, 2022.

[121] Robin Mills et al. “Physics-based simulations of aerial attacks by peregrine falcons reveal that stooping at high speed maximizes catch success against agile prey”. In: *PLoS Computational Biology* 14 (4 2018), e1006044.

[122] Marco KleinHeerenbrink et al. “Optimization of avian perching manoeuvres”. In: *Nature* 607.7917 (2022), pp. 91–96.

[123] Sofia Miñano. “Visually guided flight in Harris’ hawks: a computer vision approach”. PhD thesis. University of Oxford, 2022.

[124] Stuart Golodetz et al. “Real-Time Hybrid Mapping of Populated Indoor Scenes using a Low-Cost Monocular UAV”. In: *IEEE/RSJ International Conference on Intelligent Robots and Systems (IROS)*. Oct. 2022.

[125] US Coast Guard. *Navstar GPS user equipment introduction*. 1996. URL: `https://www.hsdl.org/?abstract&did=22298`.

[126] Elliott D Kaplan et al. *Understanding GPS: principles and applications*. 2nd. Artech House, 2006.

[127] B Bidikar et al. "Satellite Clock Error and Orbital Solution Error Estimation for Precise Navigation Applications". In: *Positioning* 5 (1 2014), pp. 22–26.

[128] European Space Agency. *Galileo and GPS 'synchronise watches': new time offset helps working together*. 2013. URL: https://www.esa.int/Applications/Navigation/Galileo_and_GPS_synchronise_watches_new_time_offset_helps_working_together.

[129] G M V. *Delay Lock Loop (DLL)*. Ed. by GMV. 2011. URL: https://gssc.esa.int/navipedia/index.php/Delay_Lock_Loop_(DLL).

[130] J Sanz Subirana, J M Juan Zornoza, and M Hernandez-Pajares. *GPS Navigation Message*. 2011. URL: https://gssc.esa.int/navipedia/index.php/GPS_Navigation_Message.

[131] van Diggelen Frank. "GPS accuracy: Lies, damn lies and statistics". In: (1998). URL: https://www.gpsworld.com/gps-accuracy-lies-damn-lies-and-statistics/%20https://www.gpsworld.com/gpsgnss-accuracy-lies-damn-lies-and-statistics-1134/.

[132] Jean-Marie. Zogg. *GPS: Essentials of Satellite Navigation,* 2009.

[133] European Union Agency for the Space Programme. *What is SBAS?* 2021. URL: https://www.euspa.europa.eu/european-space/eu-space-programme/what-sbas.

[134] Peter. Joosten and Tiberiusm Christian. "Fixing the Ambiguities: Are you sure they're right?" In: *GPS World* (May 2000 2000). URL: http://www2.unb.ca/gge/Resources/gpsworld.may00.pdf.

[135] Oxford Technical Solutions Ltd. *What is RTK?* 2020. URL: https://www.oxts.com/rtk/.

[136] Battery University. *Is lithium-ion the ideal battery?,* 2016. URL: https://batteryuniversity.com/article/is-lithium-ion-the-ideal-battery.

[137] National Geodetic Survey. *The NOAA CORS Network (NCN)*. 2022. URL: https://geodesy.noaa.gov/CORS/.

[138] European Plate Observing System. *EPOS GNSS Data Gateway,* 2022. URL: https://gnssdata-epos.oca.eu/#/site.

[139] u-Blox. *ZED-F9P Interface Description*. R08. 2020. URL: https://www.u-blox.com/en/product/zed-f9p-module#tab-documentation-resources.

[140] Angelo Joseph. "GNSS Solutions: Measuring GNSS Signal Strength". In: *Inside GNSS* (2010), pp. 20–25. URL: https://insidegnss.com/wp-content/uploads/2018/01/novdec10-Solutions.pdf.

[141] u-Blox. *GNSS antennas: RF design considerations for u-blox GNSS receivers*. R03. 2019. URL: https://www.u-blox.com/sites/default/files/products/documents/GNSS-Antennas_AppNote_%28UBX-15030289%29.pdf.

[142] Renesas Electronics. *General RTOS Concepts,* 2010. URL: https://www.renesas.com/eu/en/document/apn/general-rtos-concepts?language=en.